DISSERTATIONES
CHIMICAE
UNIVERSITATIS
TARTUENSIS
233

AKMAL KOSIMOV

Template-assisted mechanosynthesis (TAMS) for the production of bifunctional transition metal-based catalysts

DISSERTATIONES CHIMICAE UNIVERSITATIS TARTUENSIS
233

DISSERTATIONES CHIMICAE UNIVERSITATIS TARTUENSIS
233

AKMAL KOSIMOV

Template-assisted mechanosynthesis (TAMS) for the production of bifunctional transition metal-based catalysts

UNIVERSITY OF TARTU
Press
1632

Institute of Chemistry, Faculty of Science and Technology, University of Tartu, Estonia.

The dissertation is accepted for the commencement of the degree of *Doctor Philosophiae* in Chemistry on May 28, 2024 by the Council of Institute of Chemistry, Faculty of Science and Technology, University of Tartu.

Supervisor: Assoc. Prof. Nadezda Kongi
Institute of Chemistry, University of Tartu

Opponent: Prof. Elena Baranova,
Department of Chemical and Biological Engineering,
University of Ottawa, Canada

Commencement: August 29, 2024 at 15:15 Ravila 14A-1020, Tartu (Chemicum) and Microsoft Teams (*online*)

This work has been partially supported by ASTRA project PER ASPERA Graduate School ofFunctional Materials and Technologies receiving funding from the European Regional Development Fund under project in University of Tartu, Estonia

ISSN 1406-0299 (print)
ISBN 978-9916-27-568-9 (print)
ISSN 2806-2159 (pdf)
ISBN 978-9916-27-569-6 (pdf)

University of Tartu Press
www.tyk.ee

TABLE OF CONTENTS

1. LIST OF ORIGINAL PUBLICATIONS

This thesis consists of three original articles listed below. The articles are referred to in the text by Roman numerals I–III.

I. **Kosimov, A.**; Yusibova, G.; Aruväli, J.; Paiste, P.; Käärik, M.; Leis, J.; Kikas, A.; Kisand, V.; Šmits, K.; Kongi, N. Liquid-Assisted Grinding/ Compression: A Facile Mechanosynthetic Route for the Production of High-Performing Co–N–C Electrocatalyst Materials. *Green Chem.* **2022**, *24* (1), 305–314. https://doi.org/10.1039/D1GC03433B.

II. **Kosimov, A.**; Alimbekova, A.; Assafrei, J.-M.; Yusibova, G.; Aruväli, J.; Käärik, M.; Leis, J.; Paiste, P.; Ahmadi, M.; Roohi, K.; Taheri, P.; Pinto, S. M.; Cepitis, R.; Baptista, A. J.; Teppor, P.; Lust, E.; Kongi, N. Template-Assisted Mechanosynthesis Leading to Benchmark Energy Efficiency and Sustainability in the Production of Bifunctional Fe–N–C Electrocatalysts. *ACS Sustainable Chem. Eng.* **2023**, *11* (29), 10825–10834. https://doi.org/10.1021/acssuschemeng.3c02077.

III. **Kosimov, A.**; Yusibova, G.; Wojsiat, I. T.; Aruväli, J.; Käärik, M.; Leis, J.; Paaver, P.; Vlassov, S.; Kikas, A.; Kisand, V.; Piirsoo, H.-M.; Kukli, K.; Heinmaa, I.; Kaljuvee, T.; Kongi, N. Mechanosynthesis of a Bifunctional FeNi–N–C Oxygen Electrocatalyst via Facile Mixed-Phase Templating and Preheating-Pyrolysis. *J. Mater. Chem. A* **2023**, *12* (1), 335–342. https://doi.org/10.1039/D3TA04580C.

Author's contribution

Article I The author was responsible for the development of the synthesis procedure and synthesis of catalysts. The author was responsible for the interpretation of all testing results and data analysis and was primarily responsible for writing the manuscript.

Article II The author was responsible for the development of the synthesis procedure and synthesis of catalysts. The author was responsible for the interpretation of all testing results and data analysis and was primarily responsible for writing the manuscript.

Article III The author was responsible for the development of the synthesis procedure and synthesis of catalysts. The author was responsible for the interpretation of all testing results and data analysis and was primarily responsible for writing the manuscript.

2. ABBREVIATIONS AND SYMBOLS

APS	average pore size
C_{sp}	specific capacity
CV	cyclic voltammetry
E^0	standard potential
$E_{1/2}$	half-wave potential
EDX	energy-dispersive X-ray spectroscopy
EES	electrochemical energy storage
$E_{j=10}$	potential at 10 mA cm^{-2}
E_{on}	onset potential
ESC	energy storage and conversion
GC	glassy carbon
HAADF	high-angle annular dark field
j	current density
KPI	key performance indicator
LAC	liquid-assisted compression
LAG	liquid-assisted grinding
LSV	linear sweep voltammetry
MAB	metal-air battery
M-N-C	metal-nitrogen-carbon
M-N_x	metal-coordinated to nitrogen
MSM	Multi-Layer Stream Mapping
n	number of electrons transferred per O_2 molecule
NVA	non-value-added cost
OER	oxygen evolution reaction
ORR	oxygen reduction reaction
PGM	platinum-group metals
P_{max}	peak power density
PSD	pore size distribution
PXRD	powder X-ray diffraction
RDE	rotating disk electrode
RHE	reversible hydrogen electrode
S_{BET}	specific surface area
S_{dft}	
SEM	scanning electron microscopy
SHE	standard hydrogen electrode
s-NMR	solid-state nuclear magnetic resonance
STEM	scanning transmission electron microscopy
TAMS	template-assisted mechanosynthesis
TGA	thermogravimetric analysis
TGA-DTA	thermogravimetric – differential thermal analysis
VA	value-added cost

V_{μ}	micropore volume
V_{meso}	mesopore volume
V_{tot}	total pore volume
XPS	X-ray photoelectron spectroscopy
ZAB	zinc-air battery

3. INTRODUCTION

Pursuing renewable energy solutions is critical due to environmental challenges and the finite nature of fossil fuels [1,2]. Electrochemical energy storage (EES) devices are pivotal in transitioning to renewable energy, addressing the intermittency of sources like solar and wind power [3]. Among EES devices, metal-air batteries (MABs) stand out for their high theoretical energy density (1086 Wh kg^{-1}), safety, and cost-efficiency, employing uncomplicated device design and abundant materials [4]. While some MABs, like zinc-air batteries (ZABs), are brought to the commercial-level application, their performance is still limited by low power density, limited stability, and substantial overpotential of the sluggish oxygen reduction (ORR) and oxygen evolution reactions (OER) at the air electrode [5]. To optimise ORR and OER performance and stability, it is necessary to employ an effective bifunctional catalyst, which lies at the heart of the process, governing the overall ZAB efficiency. The effective promotion of ORR and OER is often associated with the platinum group metal-based catalysts [6,7], which are extremely expensive and scarce, limiting their practical application. Among the alternatives, transition metal-nitrogen-doped carbon catalysts (M-N-Cs) are considered promising candidates for oxygen electrocatalysis in ZAB [8]. These catalysts feature ORR/OER-active sites, like single-atom sites and metal nanoparticles, respectively, exhibiting superior activity and stability in the ORR and OER [9]. Furthermore, M-N-Cs allow for synthetic versatility, featuring various C/N and transition metal sources. Conventionally, in M-N-C synthesis, the bifunctional performance of the resulting catalyst is prioritised over sustainability and cost-efficiency. Nevertheless, the catalyst is a significant part of the device, which makes sustainable and cost-efficient catalyst production a determinant factor in the industrial setting, significantly impacting the total price of the MAB stack [10]. Thus, the ambition of this research lies in enhancing the bifunctional performance of catalysts without compromising their sustainability. To achieve this, a novel synthesis method – Template-Assisted Mechanosynthesis (TAMS) was developed by integrating sustainable mechanosynthesis and sacrificial templating to improve the porosity and active site density and accessibility, enhancing electrochemical performance [11,12]. Additionally, this study introduces a sustainability and cost-efficiency assessment for M-N-C production, which was previously not performed in the field of M-N-C catalysts. Thus, in this work, an industrially validated Multi-Layer Stream Mapping (MSM) is adopted as an innovative assessment tool to evaluate sustainability metrics of TAMS-derived catalysts and showcase TAMS advantages over traditional synthesis techniques [13].

This study presents a journey through the TAMS development process, which starts with establishing the initial TAMS protocol for cobalt (Co)-based catalysts, which is then gradually upgraded for iron (Fe) and nickel (Ni)-based catalysts. Each TAMS parameter, ranging from the optimisation of mechanosynthesis and pyrolysis to the integration of different metals, is progressively

refined to enhance catalyst bifunctional performance. Furthermore, each modification was evaluated and correlated with its effects on the observed morphology, composition, and catalytic performance of TAMS-derived catalysts to establish a relationship between the synthetic parameters and the resulting electrocatalytic behaviour. In this study, the critical insights into the TAMS-induced changes in structure, composition and performance aim to lay a groundwork for further advances in sustainable M-N-C production. Additionally, by introducing MSM, the study aims to turn the abstract sustainability and cost-efficiency of the catalyst into a defined quantitative value, making it an additional benchmarking characteristic, apart from catalytic performance, for future catalyst development.

4. LITERATURE OVERVIEW

4.1 Electrochemical energy storage devices

Transition to renewable energy remains one of the most prominent solutions to pressing environmental issues [14]. Nevertheless, renewable energy remains less reliable compared to fossil fuels as its efficiency is heavily dependent on external factors. Therefore, integrating renewable energy with electrochemical energy storage (EES) systems is essential for ensuring a smooth and efficient energy supply. EES devices can be categorised into rechargeable batteries, pseudocapacitors, supercapacitors, and fuel cells, which all feature numerous advantages such as high energy and power density, affordability, and sustainability [15]. Nowadays, extensive research in EES devices is focused on improving energy storage density, specific capacities (C_{sp}), power output, and charge-discharge cycle life [15]. Among the EES devices, metal-air batteries show great potential due to their high energy density, inherent safety, reliability, and the use of abundant metals for energy storage (eg. Zn, Al). The open cell structure of MAB allows the use of air as electrode material, and the negligible mass of the O_2 cathode, sourced from ambient air rather than stored within the cell, enables a higher theoretical specific energy [4].

4.2 Chemistry behind MABs

From the beginning of metal-air battery research in the 19th century [16], multiple advances have been made. Specifically, the Zn-air battery (ZAB), not long after the introduction of carbon-based gas diffusion electrodes [17], ZAB was commercialised and used as a battery for hearing aids, gaining interest in various energy storage applications [18,19]. Despite the extensive research on ZAB, they still suffer from low power density, limited stability, and poor discharge voltage plateaus, stemming from high overpotential on the air electrode caused by sluggish oxygen reduction reaction and oxygen evolution reaction kinetics [20]. Therefore, finding a cost-effective ORR/OER bifunctional catalyst is the key to improving ZAB performance [5,8]. The bifunctionality aspect necessitates the presence of both ORR- and OER-active sites to suit their distinct reaction mechanisms. In particular, OER is constrained by the formation steps of HOO* and O*, while ORR is limited by the reduction steps of OH* and O_2 [21].

Regarding device structure, ZABs comprise several key components (Fig. 1): anode, electrolyte, and cathode. At the cathode, O_2 permeates the air electrode during discharging to initiate the ORR (Equation 1a), generating OH^-. Upon charging, OER occurs at the cathode (Equation 1b), generating electrons for Zn^{2+} reduction. During discharge, the zinc (Zn) metal anode reacts with OH^- groups from ORR and gets oxidised to zincate ions ($Zn(OH)_4^{2-}$), generating electrons (Equation 2a). $Zn(OH)_4^{2-}$ decomposes into zinc oxide (ZnO) (Equa-

tion 2b), and then, during charging, ZnO is reduced back to zinc and plated onto the anode (backward reaction of Equation 3). While charging-discharging, ion movement is supported by the electrolyte. ORR and OER reactions, happening on the cathode surface, govern the kinetics of discharge and charge processes, determining the overall efficiency and stability of ZAB. Due to the slow kinetics of ORR and OER, there is a critical need for bifunctional air electrocatalysts that are both highly active and durable, improving the performance, stability, and recyclability of ZABs [8,22].

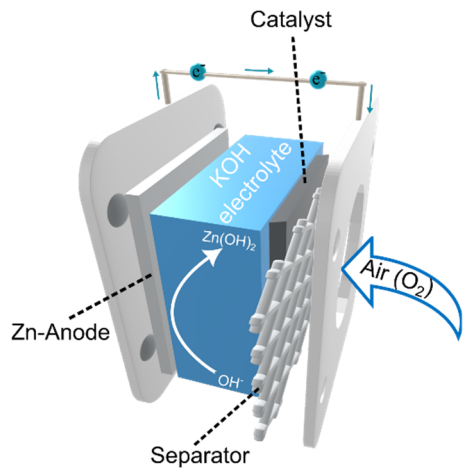

Figure 1. Schematic illustration of ZAB.

Cathode: $O_2 + 2H_2O + 4e^- \leftrightarrow 4OH^-$ (1a)

Cathode: $4OH^- \leftrightarrow O_2 + 2H_2O + 4e^-$ (1b)

Anode: $Zn + 4OH^- \leftrightarrow Zn(OH)_4^{2-} + 2e^-$ (2a)

$Zn(OH)_4^{2-} \leftrightarrow ZnO + H_2O + 2OH^-$ (2b)

Overall: $2Zn + O_2 \leftrightarrow 2ZnO$ (3)

In ZAB assembly, Zn dendrites formation at the anode, cathode flooding, and electrolyte evaporation are important problems to consider. Nevertheless, slow ORR and OER activity are the most critical, as they determine the charge-discharge efficiency and stability of ZAB [23]. Therefore, it is critical to understand the pathway of both reactions to effectively facilitate them. In ZAB, the ORR occurs in alkaline conditions with two distinct reaction pathways.

The direct 4-electron pathway:

$$O_2 + 2H_2O + 4e^- \rightarrow 4OH^- \qquad E^0 = 0.401 \text{ V} \qquad (4)$$

or 2-electron pathway:

$$O_2 + H_2O + 2e^- \rightarrow HO_2^- + OH^- \qquad E^0 = -0.065 \text{ V} \qquad (5)$$

followed by further reduction of hydroperoxide ion:

$$HO_2^- + H_2O + 2e^- \rightarrow 3OH^- \qquad E^0 = 0.867 \text{ V} \qquad (6)$$

With the standard potential (E^0) values versus the standard hydrogen electrode (SHE) at 25° C.

The desired ORR efficiency is often associated with the direct 4-electron pathway, which is fundamentally achieved by optimising the adsorption energies of the reaction intermediates [24]. Practically, such optimisation can be achieved by adjusting the active site composition (e.g., metal centre and coordinating groups composition) and increasing active site density and accessibility [25]. The OER pathway is proposed to proceed by forming an adsorbed *OH on the metal site, which reacts with OH^-, yielding *O and water. Next, *O reacts with another OH^-, forming an *OOH intermediate, which reacts with OH^- and O_2 getting desorbed, restoring the active metal site [26]. Like in ORR, optimised adsorption energies of the intermediate determine the OER efficiency and practically require adjusting active site composition, density and accessibility. Thus, the key to a superior bifunctional performance lies in a thorough design of catalysts, which accommodate abundant and accessible ORR/OER active sites.

4.3 Bifunctional M-N-C catalysts for ZAB

Today, *state-of-the-art* catalysts primarily depend on platinum group metals (PGMs) to achieve significant ORR and OER activity [27]. Despite being the benchmark, the high costs, scarcity, and limited durability of PGMs pose substantial challenges to their widespread industrial application in energy storage and conversion (ESC) devices. In search of alternatives, non-precious-metal catalysts have been investigated as promising PGM replacement [28]. Among the non-precious-metal catalysts, transition metal-nitrogen-doped carbon catalysts (M-N-C) stand out as viable options with comparable PGM ORR/OER performance and remarkable electrochemical stability [29–31]. Furthermore, compared to PGMs, M-N-Cs are more cost-effective, enabling the use of abundant raw materials as metal/nitrogen /carbon sources [32]. Such variability makes M-N-C a versatile framework for sophisticated design, encompassing the selection of suitable precursors, optimisation of synthetic methodologies and post-synthetic treatments to enhance ORR and OER performance [32].

In ORR, the electrocatalytic activity of M-N-Cs is associated with the synergy of distinct active sites. ORR-active sites represent (i) nitrogen-coordinated transition metal ($M\text{-}N_x$) [30,33,34] and (ii) nitrogen functional groups (e.g., pyridinic-N and pyrrolic-N) [35,36]. The activity of $M\text{-}N_x$ sites is attributed to the electronic structure of the metal centres, which facilitates the breaking of the O-O bond, by bonding with π^*-electrons of O_2 via the empty d_{z2} orbitals [37]. In the $M\text{-}N_x$ configuration, the choice of the metal centre has a significant impact on the catalytic performance, following the activity trend $Fe^{2+} > Co^{2+} > Mn^{2+} > Cu^{2+}$ [38]. Additionally, bimetallic M-N-C catalysts can enhance the electrocatalytic activity, featuring a combination of transition metals (e.g., Fe, Co, Ni), which boost ORR efficiency in synergy with the nitrogen-doped carbon matrix [39,40].

OER-active species in M-N-C catalysts usually represent mono-/bimetallic nanoparticles of transition metal oxides or OER-active alloys [41]. Factors like the choice of metal, oxidation states and the type of support strongly influence the OER activity of oxides. Among high-performing oxides in OER, CoO_x [42] and FeO_x [43] gained substantial attention for OER due to the mixed valence states of Co cations and the abundance of iron. Recently, an outstanding OER performance was observed with nickel and Ni-M alloys/oxides [44]. Specifically, Ni-based oxides $Fe_6Ni_{10}O_x$ [45] and $Fe_3Ni_7O_x$ [46] demonstrated exceptional OER activity, outperforming pure NiO_x or FeO_x. Furthermore, nickel-iron (FeNi) nanoparticles performed outstandingly in OER, making these alloy nanoparticles an abundant and cost-efficient OER catalyst [47–49]. Thus, as shown by previous studies [50,51], the way to achieve a superior bifunctionality is by incorporating ORR and OER-active species within the carbon/nitrogen matrix of M-N-C and optimising their composition, density and accessibility.

4.4 Mechanosynthesis and templating for M-N-C catalysts

As previously mentioned, M-N-C materials present a flexible platform for various M-N-C synthesis approaches and precursors. The most common production way is to combine transition metal and nitrogen-containing precursors through high-temperature pyrolysis [52]. This approach utilises various transition metal salts and nitrogen-rich sources (e.g., dicyandiamide, urea, melamine) as precursor materials [53–56]. Despite the existing versatility, the synthetic protocols for M-N-C catalysts mostly rely on liquid-phase processes – such as precipitation, deposition-precipitation, hydrothermal treatments, and wet impregnation/doping, which raise significant sustainability concerns [57]. Specifically, these methods often lead to the production of toxic waste, require considerable time and energy, and involve extensive solvent use, which together create bottlenecks that hinder large-scale production. Solid-phase mechanosynthesis (MS) has recently emerged as a promising alternative to address these issues [11,57].

In MS, chemical reaction is facilitated by applying mechanical force via milling or grinding. This approach dates back to ancient times when it was performed using mortar and pestle. Today, mechanochemistry's capabilities have recently garnered renewed interest in sustainable chemical manufacturing [58], with IUPAC acknowledging its advantages among the top ten chemical inventions [59]. Unlike traditional wet chemistry techniques [60], mechanochemistry typically necessitates minimal or no solvents and employs resource-efficient procedures, reducing waste generation and enhancing scalability [61]. Furthermore, MS often yields improved/complete conversion of reactants, minimising the requirement for elaborate purification steps.[62] Currently, mechanochemical synthesis is upgraded by employing automated equipment like ball mills (planetary, vibrational) or extruders, enabling high-energy friction and collisions between the grinding media and reactants [63]. In MS, efficient synthesis design involves a thorough consideration of the following parameters: (1) type of equipment, (2) additives (e.g. reaction catalysts, grinding aid), (3) grinding media (e.g., steel, ceramic) and (4) dimensions of grinding jars and balls [62,64,65]. In general, MS can be classified into two main techniques – neat grinding (NG) and liquid-assisted grinding (LAG). NG refers to a solid-phase reaction without liquid media [68], whereas LAG refers to a mechanochemical reaction in the presence of a catalytic amount of solvent [66]. While both NG and LAG approaches significantly reduce the required solvent volume, LAG has the capacity to greatly improve the yield and efficiency of a reaction [67]. Due to its advantages, MS has gained a significant interest in M-N-C production. Recent studies have highlighted the effectiveness of MS in producing M-N-C materials that show outstanding performance and superior synthetic efficiency over solution-based methods [57,68].

Apart from sustainability advantages, MS also provides a versatile platform for synthetic upgrades. In particular, sacrificial templating can be effectively integrated into MS to enhance the catalytic activity of M-N-C materials [57]. Sacrificial templating uses a template or a scaffold that provides a rigid spatial framework, directing the generation of a template-defined structure upon removal [69,70]. By forming a confined environment, the templating approach can generate diverse porous structures with precisely defined and adjustable morphologies [71]. In the context of M-N-C synthesis, templating can yield hierarchical porous structures with high diffusivity and surface area, improving porosity, mass/electron transport and catalytic performance, superior to non-templated counterparts [72–74]. In templating, inorganic salts and oxides, such as NaCl, KCl, MgO, Al_2O_3, etc., can be used as abundant, stable, and environmentally friendly templates without requiring sophisticated removal [75–77]. Thus, combining MS and sacrificial templating is a promising way to tailor the structural and functional properties of M-N-C catalysts in a sustainable manner.

4.5 Sustainability assessment in M-N-C catalysts

In the context of large-scale production, manufacturing has a significant impact on the ecosystem and human life [78]. Therefore, apart from improving efficiency and reducing costs, it is necessary to minimise the sustainability impact [79]. To address these concerns, plenty of sustainability assessment tools such as life cycle assessment (LCA), life cycle costing (LCC), and multicriteria analysis (MCA) were introduced, becoming a well-known tool in industrial settings [80]. These tools enable holistic assessments of key environmental, economic, social, and technical criteria, allowing better decision-making with consideration of economic and environmental consequences [81].

Nevertheless, despite the fairly well-developed sustainability assessment framework and extensive M-N-C research, no attempts have been made to evaluate the sustainability of the M-N-C catalyst production. Moreover, when assessing ESC systems' viability, evaluating the catalyst production footprint remains an often overlooked aspect [82]. Considering the current environmental awareness and possible wide application of ESC devices, it is imperative to comprehensively assess the environmental and economic impact of catalyst production, which takes up a substantial part of the ESC device [10].

To fill this gap and pioneer sustainability assessment, waste mapping, and cost-based efficiency analysis of M-N-C synthesis, the Multi-Layer Stream Mapping framework can be applied to assess M-N-C catalyst production [13]. This methodology, founded on innovative Lean Methodologies [83], was developed to assess the resource efficiency of manufacturing systems and has been validated across various industrial sectors [84,85]. Evolving into a contemporary digital Lean tool, the MSM framework evaluates the efficiency of time and resource utilisation in production systems, identifying waste and other variables within a given process. The application of the MSM assessment facilitates the easy identification of inefficiencies and waste hotspots, serving as a robust foundation for confirming the feasibility of M-N-C catalyst production.

5. AIM OF THE STUDY

The aim of this study is to develop and optimise the template-assisted mechanosynthesis (TAMS) for producing templated M-TPTZ coordination complexes, which are pyrolysed to yield bifunctional M-N-C catalysts. The design of TAMS-derived catalysts aims to optimise the content and exposure of ORR and OER active sites to fabricate bifunctional catalysts for zinc-air batteries. Additionally, the improvement and assessment of TAMS-derived catalysts' sustainability are key objectives of this research. The study is structured into four main components with specific objectives.

1. To establish the foundational principles of TAMS by producing and characterising a series of Co-N-C catalysts. To assess and correlate the effect of the TAMS protocol on the morphology, composition and ORR and OER activity [I].
2. To upgrade the TAMS process with rapid pyrolysis to enhance the performance of the Fe-N-C catalysts. To assess and correlate the effect of the upgraded TAMS protocol on the morphology, composition and ORR and OER activity. To apply TAMS-derived Fe-N-C as ZAB electrode [II].
3. To enhance TAMS with preheat-pyrolysis and mixed-phase templating to produce bimetallic FeNi-N-C catalysts. To assess and correlate the effect of the upgraded TAMS protocol on the morphology, composition and ORR and OER activity. To apply TAMS-derived FeNi-N-Cs as ZAB electrodes [III].
4. To assess the sustainability and cost-efficiency of TAMS by performing a comprehensive analysis of resource usage, energy consumption, and waste generation. Compare the results with conventional M-N-C synthesis techniques [I, II].

6. EXPERIMENTAL

6.1 Materials and Equipment

2,4,6-tri(2-pyridyl)-1,3,5-triazine (tripyridyl triazine – TPTZ, ≥98%, Sigma-Aldrich), 2,4,6-triamino-1,3,5-triazine (Melamine, 99% Alfa Aesar), Iron(III) chloride hexahydrate ($FeCl_3 \cdot 6H_2O$, ≥98% Sigma-Aldrich), cobalt nitrate hexahydrate ($Co(NO_3)_2 \cdot 6H_2O$, Sigma-Aldrich), hydrochloric acid (HCl, ≥37%, Honeywell-Fluka) and Nickel(II) chloride hexahydrate ($NiCl_2 \cdot 6H_2O$, ≥98% Sigma-Aldrich) were used as received. Sodium chloride (NaCl, ≥99%, Sigma-Aldrich) and potassium chloride (KCl, 99.0-100.5%, Sigma-Aldrich) – were pulverised in a ball mill to achieve an average crystallite size of 0.3–0.8 μm. Ultrapure water (18.2 MΩ cm; Milli-Q purification system by Millipore, Inc.) was used to prepare all solutions. Milling was conducted in a ball mill (Fritsch Planetary Mill Pulverisette 7) using 12 mL zirconium oxide grinding bowls and 5 mm diameter zirconium oxide milling balls. A tubular furnace (Carbolite Gero EST 12/300B) was used for the post-synthetic carbonisation.

6.2 Synthesis

6.2.1 Co-N-C series

CoNC-LAG: $Co(NO_3)_2 \cdot 6H_2O$ (31 mg, 0.106 mmol, 1 eq.) and 2,4,6-tri(2-pyridyl)-1,3,5-triazine (100 mg, 0.32 mmol, 3 eq.) were placed in a ball mill jar with 40 μl of EtOH and ground at 600 rpm for 20 min to synthesise the cobalt 2,4,6-tri(2-pyridyl)-1,3,5-triazine complex (Co–TPTZ). Consequently, the mixture was pyrolysed under N_2 at 700 °C for 2 h with a ramping of 20 °C min^{-1}. After pyrolysis, the oxide/metal particles were removed by acid leaching with 5 mL of 1 M HCl for 3 h at 70 °C to give CoNC-LAG (m = 24.6 mg).

3D-CoNC-LAG: $Co(NO_3)_2 \cdot 6H_2O$ (31 mg, 0.106 mmol, 1 eq.) and 2,4,6-tri(2-pyridyl)-1,3,5-triazine (100 mg, 0.32 mmol, 3 eq.), NaCl (1 g) were placed in a ball mill jar with 40 μl of EtOH and ground at 600 rpm for 20 min. Consequently, the mixture was pyrolysed under N_2 at 700 °C for 2 h with a ramping of 20 °C min^{-1}. After pyrolysis, NaCl was washed out by H_2O and treated with 5 mL of 1 M HCl for 3 h at 70 °C to give 3D-CoNC-LAG (m = 28.8 mg).

3D-CoNC-LAC: $Co(NO_3)_2 \cdot 6H_2O$ (31 mg, 0.106 mmol, 1 eq.) and 2,4,6-tri(2-pyridyl)-1,3,5-triazine (100 mg, 0.32 mmol, 3 eq.) and NaCl (1 g) were mixed thoroughly together, placed in a pellet mold, and 40 μl of EtOH was added and compressed at 300 kg cm^{-2} for 10 minutes. Consequently, the mixture was pyrolysed under N_2 at 700 °C for 2 h with a ramping of 20 °C min^{-1}. After pyrolysis, NaCl was washed out by H_2O and treated with 5 mL of 1 M HCl for 3 h at 70 °C to give 3D-CoNC-LAC (m = 32 mg).

3D-CoNC-LAG-LAC: $Co(NO_3)_2 \cdot 6H_2O$ (31 mg, 0.106 mmol, 1 eq.) and 2,4,6-tri(2-pyridyl)-1,3,5-triazine (100 mg, 0.32 mmol, 3 eq.), NaCl (1 g) and 40 µl of EtOH were placed in a ball mill jar and ground at 600 rpm for 20 min. The powder was then placed in a pellet mold, EtOH was added, and the mixture was compressed at 300 kg cm^{-2}. Consequently, the mixture was pyrolysed under N_2 at 700 °C for 2 h with a ramping of 20 °C min^{-1}. After pyrolysis, NaCl was washed out by H_2O and treated with 5 mL of 1 M HCl for 3 h at 70 °C to give 3D-CoNC-LAG-LAC (m = 34.1 mg).

6.2.2 Fe-N-C series

FeNC-LAG: 100 mg (0.32 mmol, 3 eq.) of 2,4,6-tri(2-pyridyl)-1,3,5-triazine (TPTZ), 29.7 mg (0.11 mmol, 1 eq) of $FeCl_3 \cdot 6H_2O$ were placed in a grinding jar with 40 µL of EtOH and ground in a ball mill at 600 rpm for 20 min to synthesise template-free Fe-TPTZ. Then, the mixture was pyrolysed under N_2 at 800 °C for 1 h with a heating rate of 50 °C min^{-1}. Acid etching was performed using 1 M HCl at 70 °C for 3 h to remove excess metal or oxides. The final mass of the FeNC-LAG was 23.6 mg.

3D-FeNC-LAG: 100 mg (0.32 mmol, 3 eq.) of 2,4,6-tri(2-pyridyl)-1,3,5-triazine, 29.7 mg (0.11 mmol, 1 eq) of $FeCl_3 \cdot 6H_2O$, 1000 mg of NaCl were placed in a grinding jar with 40 µL of EtOH and ground in a ball mill at 600 rpm for 20 min. Then, the mixture was pyrolysed under N_2 at 800 °C for 1 h with a heating rate of 50 °C min^{-1}. NaCl was washed out with MilliQ water. Acid etching was performed using 1 M HCl at 70 °C for 3 h to remove excess metal or oxides. The final mass of the 3D-FeNC-LAG was 39.8 mg.

3D-FeNC-LAC: 100 mg (0.32 mmol, 3 eq.) of 2,4,6-tri(2-pyridyl)-1,3,5-triazine, 29.7 mg (0.11 mmol, 1 eq.) of $FeCl_3 \cdot 6H_2O$, 1000 mg of NaCl were mixed and poured into a pellet mold with 40 µL of EtOH. The mixture was compressed using a pressure of 300 kg cm^{-2} (≈294.2 bar). Then, the mixture was pyrolysed under N_2 at 800 °C for 1 h with a heating rate of 50 °C min^{-1}. NaCl was washed out with MilliQ water. Acid etching was performed using 1 M HCl at 70 °C for 3 h to remove excess metal or oxides. The final mass of the 3D-FeNC-LAC is 40.0 mg.

6.2.3 Fe/Ni-N-C series

IroNi-1: 150 mg (0.48 mmol) of 2,4,6-tri(2-pyridyl)-1,3,5-triazine, 137.7 mg (0.57 mmol) of $NiCl_2 \cdot 6H_2O$ and 310.5 mg (1.15 mmol) of $FeCl_3 \cdot 6H_2O$ were placed in a milling jar with 360 µL of 1 M HCl solution and milled at 25 Hz for 10 minutes. Consecutive 2-step pyrolysis was performed by preheating at 300 °C for 1 hour with a heating rate of 10 °C min^{-1}, then carbonised at 800 °C for 1 hour at the same heating rate. Then, the mixture was washed with H_2O at 80 °C for 1 hour. After filtration and drying, the final mass of IroNi-1 was 104 mg.

IroNi-2: 150 mg (0.48 mmol) of 2,4,6-tri(2-pyridyl)-1,3,5-triazine, 196 mg (1.55 mmol) of 2,4,6-Triamino-1,3,5-triazine (melamine), 137.7 mg (0.57 mmol) of $NiCl_2 \cdot 6H_2O$ and 310.5 mg (310.5 mmol) of $FeCl_3 \cdot 6H_2O$ were placed in a milling jar with 360 µL of 1 M HCl solution and milled at 25 Hz for 10 minutes. Consecutive 2-step pyrolysis was performed by preheating at 300 °C for 1 hour with a heating rate of 10 °C min^{-1}, then carbonised at 800 °C for 1 hour at the same heating rate. Then, the mixture was washed with H_2O at 80 °C for 1 hour. After filtration and drying, the final mass of IroNi-2 was 113 mg.

IroNi-3D: 150 mg (0.48 mmol) of 2,4,6-tri(2-pyridyl)-1,3,5-triazine, 196 mg (1.55 mmol) of 2,4,6-Triamino-1,3,5-triazine (melamine), 137.7 mg (0.57 mmol) of $NiCl_2 \cdot 6H_2O$, 310.5 mg (310.5 mmol) of $FeCl_3 \cdot 6H_2O$ and 468.5 mg (6.3 mmol) of KCl were placed in a milling jar with 360 µL of 1 M HCl solution and milled at 25 Hz for 10 minutes. Consecutive 2-step pyrolysis was performed by preheating at 300 °C for 1 hour with a heating rate of 10 °C min^{-1}, then carbonised at 800 °C for 1 hour at the same heating rate. Then, the mixture was washed with H_2O at 80 °C for 1 hour. After filtration and drying, the final mass of IroNi-3D was 128 mg.

6.3 Physical characterisation

Nitrogen physisorption
Low-temperature N_2 adsorption with a NOVAtouch LX2 (Quantachrome Instruments) was performed to determine the textural parameters of the prepared materials (BET surface area (S_{BET}), the total pore volume (V_{tot}), specific surface area (S_{dft}), the volume of micropores (V_{μ}), and pore size distributions (*PSD*)). Before measurement, each sample was degassed at 300 °C under vacuum for 12 hours [86,87].

Powder X-Ray Diffraction (PXRD)
The PXRD analysis was performed using Bruker D8 Advance diffractometer with Ni-filtered Cu Kα as a radiation source and LynxEye line detector. The catalysts were measured in a range of 3° to 93° 2θ using a scanning step of 0.013° 2θ and a counting time of 356 s per step.

X-Ray Photoelectron Spectroscopy (XPS)
XPS analysis was carried out by the PHI-TFA XPS spectrometer (Physical Electronics, Inc.), equipped with an X-ray Al-monochromatic source under the vacuum (10^{-9} mbar). Narrow multiplex scans of the peaks were recorded using a pass energy of 23.5 eV with a step size of 0.25 eV at a take-off angle of 45° with respect to the sample surface. A low-energy electron gun was used for surface charge neutralisation. Obtained spectra were processed using Multipak v8.0 (Physical Electronics, Inc., Chanhassen, MN, USA).

Microwave Plasma Atomic Emission Spectroscopy (MP-AES)

MP-AES analysis was performed with Agilent 4210 MP-AES. Analytical wavelengths were set to Fe 371.993 nm and Co 340.512 nm. Catalysts (10 mg) were digested in a microwave (Anton Paar Multiwave PRO system) in a mixture of 2 mL of H_2O_2 and 4 mL of HNO_3 in NXF100 vessels (PTFE/TFM liner) at 230 °C and pressures in the range of 45 and 50 bar. Afterwards, samples were diluted with 2% HNO_3 to 5 mg L^{-1} of metal concentration.

Scanning Transmission Electron Microscopy (STEM)

A double-corrected and monochromated Themis Z scanning transmission electron microscope (ThermoFisher Scientific-TFS) was used, operating at 300 kV and equipped with high-angle annular dark-field (HAADF) STEM mode. The beam convergence angle was measured at ~24.0 mrad, and the probe current of 50 pA was used for STEM imaging. Energy dispersive X-ray spectroscopy (STEM EDS maps) results were achieved with a Dual X EDS system (Bruker) using two large area detectors, capturing 1.76 steradians with a probe current of 100 pA for over 1 hour. Data acquisition and analysis were made using Velox software.

Thermogravimetric analysis (TGA)

The Thermogravimetric – Differential Thermal Analysis (TG-DTA) experiments were conducted in an Ar atmosphere with a Setaram Labsys Evo 1600 thermo-analyser. Samples (6.0-6.9 mg) were placed in a standard 100 μL and thermalised under the gas flow of 20 mL min^{-1}. First, the samples were heated up to 300 °C at the heating rate of 10 °C min^{-1} under non-isothermal conditions and stored at 300 °C for 1 hour. Then, the temperature was increased to 800 °C at the heating rate of 10 °C min^{-1} under non-isothermal conditions and stored at 800 °C for 1 hour.

Solid-State Nuclear Magnetic Resonance (s-NMR)

Solid state ^{13}C MAS NMR spectra were recorded on Bruker AVANCE-II spectrometer at 14.1 T magnetic field using a probe for 1.8 x 15 mm Si_3N_4 rotors, 39 kHz fast spinning speed, spin-echo pulse sequence ($\pi/2 - \tau - \pi - \tau -$ acquisition) and relaxation delay 200 ms. Each spectrum was averaged by 400000 accumulations. In addition, to see only the resonances of aromatic TPTZ carbons attached to the protons, we recorded the spectra with a probe for 4 mm rotors at 12.5 kHz spinning speed with ordinary $^{1}H/^{13}C$ cross-polarization technique followed by high field proton decoupling (CP-MAS NMR) as well. All chemical shifts are given in the TMS scale.

6.4 Electrochemical assessment

Catalyst ink preparation

Electrocatalyst inks were prepared by dispersing 5 mg of catalyst powders in 495 μL of isopropanol and 5 μL of Nafion ionomer solution (5 wt.%, Sigma-Aldrich). For even dispersion, the suspensions were ultra-sonicated for 20 min.

Electrode modification

The catalyst suspensions were dropped onto the alumina-polished glassy carbon (GC) electrodes with five 2 μL steps (total of 10 μL) for material loading of 0.5 mg cm^{-2}.

Electrochemical measurements

The electrocatalysts were assessed in a standard three-electrode cell system connected to the Autolab PGSTAT128N potentiostat/galvanostat (Metrohm Autolab B.V., The Netherlands) and controlled by Nova 2.1.4 software. The GC rotating disk electrode (diameter – 5 mm) served as the working electrode. Reference electrode and counter electrodes were silver-silver chloride (Ag/AgCl), and GC rod, respectively. The alkaline electrolyte solution was prepared from 2.8 g of KOH (purity ≥99.998%, Sigma-Aldrich) in 500 mL of Milli-Q water. The electrolyte was then saturated with pure O_2 (99.999%, Linde Gas) or deaerated with Ar gas (99.999%, Linde Gas).

The cyclic voltammetry (CV) curves were obtained in an Ar-saturated electrolyte at scan rates of 50 mV s^{-1} and 10 mV s^{-1}. The samples were also subjected to cycling in an Ar-saturated solution to determine the electrochemical double-layer capacitance. The modified electrodes were cycled at the 10, 20, 30, 40, and 50 mV s^{-1} scan rates. Points of cathodic and anodic current densities were extracted from the measured data at non-Faradaic potentials.

The ORR polarisation curves were recorded in O_2-saturated 0.1 M KOH electrolyte with the scan rate of 10 mV s^{-1} at various electrode rotation speeds (360, 610, 960, 1600, 1900, and 3100 rpm). Then, the OER activity in the Ar-saturated electrolyte (0.1 M KOH) was investigated at a scan rate set to 10 mV s^{-1}. 85% *iR* compensation was applied to all electrochemical data where required. Potentials were then converted to RHE with the formula: $E_{Ag/AgCl} = E_{RHE} - 0.966$ ($E_{vs\ RHE} = E_{vs.Ag/AgCl} + 0.0591*pH + E_{Ag/AgCl}^{\theta}$ (0.209)).

The main ORR kinetic parameters (onset and half-wave potentials (E_{on} and $E_{1/2}$), kinetic current density (j_k), diffusion-limited current density (j_d), number of electrons transferred per oxygen molecule (n), and Tafel slope values) were extracted from the rotating disc electrode (RDE) data. The RDE data was analysed by the Koutecky–Levich (K–L) equation [88]:

$$\frac{1}{j} = \frac{1}{j_k} + \frac{1}{j_d} = \frac{1}{nFkC_{O_2}^b} + \frac{1}{0.62nFC_{O_2}^b D_{O_2}^{2/3} \upsilon^{-1/6} \omega^{1/2}} \quad (7)$$

The current densities (in mA cm^{-2}) in the above equation are j – measured current density, j_k – kinetic current density, and j_d – diffusion-limited current density. The remaining values are defined as follows: ω is the electrode rotation rate (rad s^{-1}), n is the electron transfer number per oxygen molecule, F is the Faraday constant (96 485 C mol^{-1}) [89], C^b_{O2} is the oxygen concentration in 0.1 M KOH (1.2×10^{-6} mol cm^{-3}), D_{O2} is the diffusion coefficient of O_2 (1.9×10^{-5} cm^2 s^{-1} in 0.1 M KOH), and υ – kinematic viscosity of the solution (0.01 cm^2 s^{-1}) [90]. The overall oxygen electrode bifunctional activity was calculated as the potential difference (ΔE) of an ORR $E_{1/2}$ and an OER $E_{j=10}$: $\Delta E = E_{j=10} - E_{1/2}$.

Assembly of zinc-air battery

ZAB tests were conducted with an in-house single-cell battery in a two-electrode configuration constructed as a stacked plate set. The air cathode was fabricated from a nickel mesh, a current collector, and a carbon paper gas diffusion layer (Sigracet BB39). The cathode layer was coated by hand brush coating the catalyst ink (loading of 2 mg cm^{-2}). Zn foil (99%) was utilised as an anode, and 6 M KOH and 0.2 M $Zn(CH_3CO_2)_2$ solution as electrolytes.

The catalyst inks were prepared from 7 mg of catalyst, 20 µl of 5% Nafion ionomer solution (Sigma-Aldrich), 0.2 mL of MilliQ water, and 0.6 mL of ethanol for 1.5 h. The commercial PtRu (Pt – 50 wt.%, Ru – 25 wt.%) was used to prepare benchmark PtRu catalyst ink. Galvanostatic tests were controlled by a potentiostat (Autolab PGSTAT204).

6.5 Multi-Layer Stream Mapping (MSM)

MSM analysis followed the previously reported protocol [13,83] and was performed in three consecutive steps (Scheme 1):

1) MSM Inventory Collection
2) Calculation following the developed MSM Algorithm
3) MSM Results Assessment

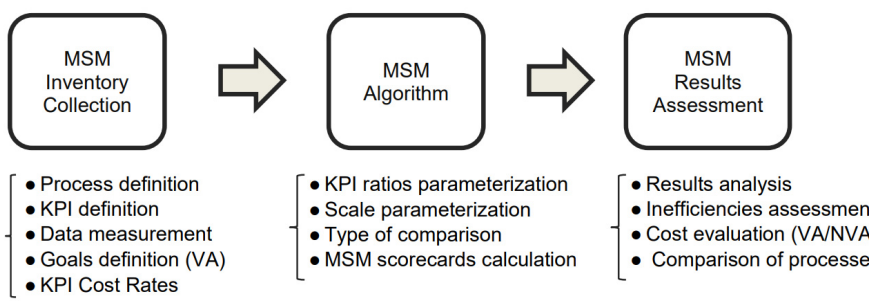

Scheme 1. Processes associated with each MSM step.

First, four classes of key performance indicators (KPIs) were identified for the TAMS: Time, Energy, Resources, and Catalytic performance. Then, KPI values were calculated to produce 1 g of the catalyst (Table 1).

Table 1. Summary of KPI values to produce 1 g of the corresponding catalyst.

Catalyst	KPIs					
	Time (h)	Energy (kWh)	Resources	Catalytic performance		
				E_{on} (V vs. RHE)	$E_{1/2}$ (V vs. RHE)	$E_{j=10}$ (V vs. RHE)
FeNC-LAG	4.6	3.94	TPTZ – 4.24 g $FeCl_3$ – 0.73 g EtOH – 1.7 mL NaCl – 0 g 1M HCl – 200 mL H_2O (MilliQ) – 0 mL	0.89	0.69	1.78
3D-FeNC-LAG	5.6	4.34	TPTZ – 2.5 g $FeCl_3$ – 0.43 g EtOH – 1.7 mL NaCl – 25 g 1M HCl – 125 mL H_2O (MilliQ) – 250 mL	1.00	0.85	1.73
3D-FeNC-LAC	5.8	3.42	TPTZ – 2.5 g $FeCl_3$ – 0.43 g EtOH – 1.7 mL NaCl – 25 g 1M HCl – 125 mL H_2O (MilliQ) – 250 mL	0.94	0.80	1.70

Each KPI relative efficiency calculation followed the reported formula [13,83]:

$$Relative\ Efficiency\ (\%) = \frac{selected\ KPI\ value}{best\ KPI\ value\ from\ the\ identical\ class} \times 100\%$$

KPI relative efficiencies were employed to assemble the scorecards, where the production process was divided into three separate processes: (1) Synthesis of precursor, (2) Pyrolysis, and (3) Workup. An example of a scorecard is depicted in Scheme 2.

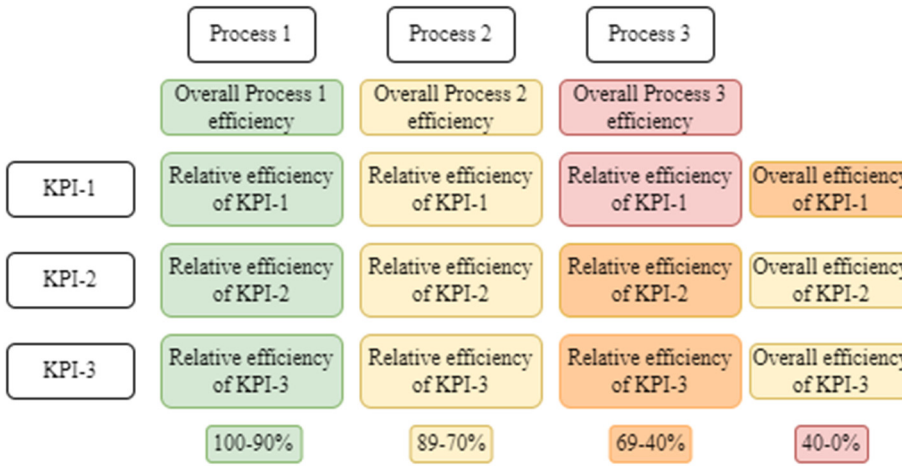

Scheme 2. KPI scorecard example.

The value-added (VA) and non-value-added (NVA) costs per process were determined according to the previously reported procedure [13]. The cost was estimated in EUR/unit of the material in mL or gram for the resource cost assessment (Table 2). Cost per unit of TPTZ, $FeCl_3$, NaCl, EtOH, and 1M HCl were estimated from the Sigma Aldrich. The Estonian electricity rate for the business sector (0.183 EUR per 1 kWh) was considered the energy cost. The "time" in the KPI cost assessment was the equipment operation time. The equipment operation time cost was estimated according to the formula:

$$Operation\ time\ cost = \ operation\ time \frac{equipment\ price\ (EUR)}{guarantied\ operation\ period\ (hours)}$$

Table 2. The equipment for catalyst production and cost estimation are summarised in the table below.

Equipment type	Equipment data	Guaranteed operation time (h)	Equipment price (EUR)	Operation cost (EUR/h)
Ball-mill	Fritsch Planetary Mill Pulverisette 7	43800 (5 years)	10000	0.228
Tubular Furnace	Carbolite Gero EST 12/300B	43800 (5 years)	6000	0.137
Magnetic stirrer	VWR Standard Hot Plate Stirrer 97042-594	26280 (3 years)	500	0.019

7. RESULTS AND DISCUSSION

7.1 TAMS for bifunctional Co-N-C catalysts

7.1.1 Synthesis of Co-N-C catalysts via TAMS

In the first part of this study, TAMS for M-N-C catalysts was developed from the reported application of NaCl as a nanoconfinement agent to support the Co/Fe-TPTZ coordination polymer [91,92]. This method uses TPTZ as a C/N source and an effective polydentate ligand, forming N-coordinated metal moieties (Fig. 2) [93]. The coordinated metal ions give an advantage of improved stability during pyrolysis, making them less prone to agglomerating and leading to improved atom utilisation. As a result, coordinated metal ions form the M-N_x site effectively and inhibit the clustering of less-active nanoparticles [94].

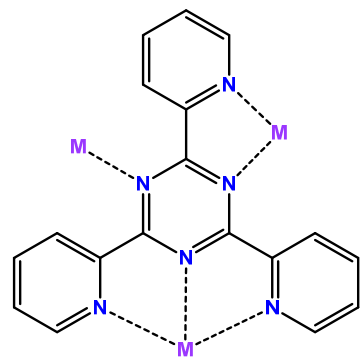

Figure 2. Polydentate coordination states of 2,4,6-tri(2-pyridyl)-1,3,5-triazine.

Furthermore, NaCl showcases versatile advantages: (1) stabilising Co-TPTZ-complex during heat treatment, (2) improving porosity, and (3) increasing the accessibility of catalytically active sites [91,92]. While NaCl-supported catalyst synthesis was efficient, it involved prolonged solvent-based synthesis with further intensive freeze drying. Therefore, it was hypothesised that adapting the templating approach to mechanosynthesis could significantly decrease reaction times and simplify or even eliminate post-synthetic workups to make this approach more sustainable and energy/time-efficient. Thus, to investigate the suitability of mechanosynthesis for templated synthesis, a series of Co-based catalysts was synthesised and evaluated.

At first, it was important to confirm that mechanosynthesis is suitable for forming TPTZ metal-organic polymer. Therefore, a mechanochemical reaction between $Co(NO_3)_2 \cdot 6H_2O$ and TPTZ was conducted in a ball mill with a catalytic amount of EtOH. In this test (Fig. 3a), an immediate colour change of the reaction mixture was observed: a heterogeneous mixture of ligand (yellow) and metal salt (pink) turned into a homogeneous red powder, indicating the success-

ful formation of Co-TPTZ [93], which was further recrystallised to give dark-red needle-like crystals (Fig. 3b, (inset)). The structural change was determined by the comparative PXRD (Fig. 3b) by the disappearance of characteristic peaks of cobalt nitrate at 15° and 30.5° and the appearance of new peaks of Co-TPTZ at 7.5°, 14.3°, and 26.3°.

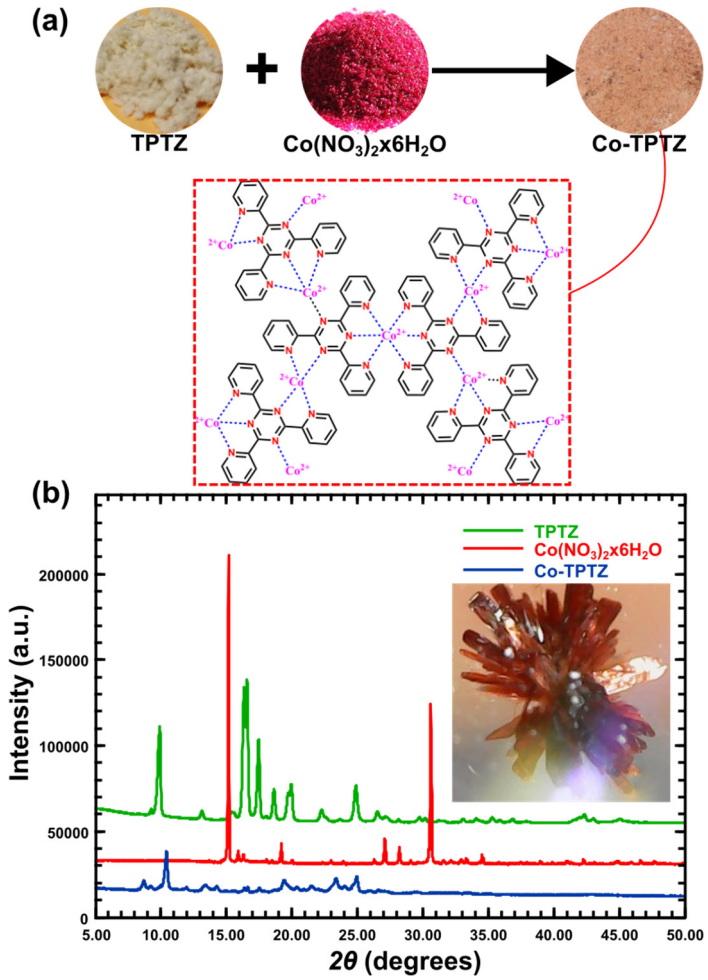

Figure 3. Mechanosynthesis of Co-TPTZ: (a) Visual colour change and the suggested structure of Co-TPTZ; (b) Comparative PXRD of starting materials and product, single crystal of Co-TPTZ (inset).

Upon confirming the efficiency of mechanosynthesis towards Co-TPTZ, the protocol was upgraded by introducing NaCl nano-templates via one-pot mechanosynthesis (Fig. 4). In this approach, the NaCl-template was also used as a grinding aid to facilitate the milling and improve materials dispersion, and

provide finer particles for narrower particle size distribution [95]. To assess the effect of the new procedure, three different NaCl-templated catalysts were synthesised using liquid-assisted grinding (LAG) and compression (LAC) and their combination. The templated catalysts were designated as **3D-CoNC-LAG**, **3D-CoNC-LAC**, and **3D-CoNC-LAG-LAC**. Non-templated catalyst **CoNC-LAG** was prepared for comparison.

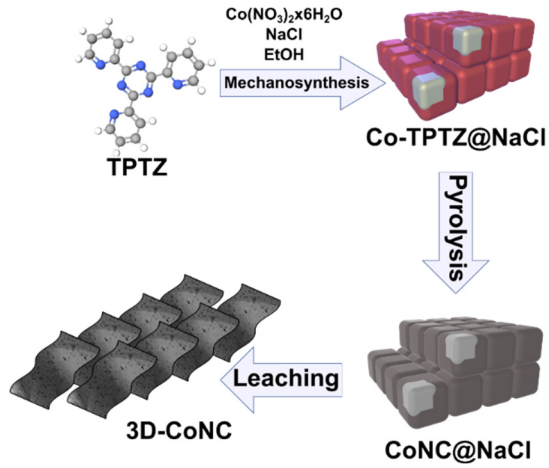

Figure 4. Template-assisted mechanosynthesis of 3D-CoNC.

First, optical microscopy (Fig. 5a-c) was used to assess the results of TAMS. After TAMS (Fig. 5a), templated Co-TPTZ samples showed an even integration of NaCl crystallites into the polymer framework, which remained included in the carbon framework after the pyrolysis (Fig. 5b). Upon pyrolysis and acid leaching (Fig. 5c), non-templated **Co-TPTZ-LAG** appears as dense bulky carbon blocks with a metallic shine, suggesting the formation of metallic Co. In contrast, supported catalysts yielded homogeneous porous carbon. This morphological difference was attributed to a stabilising effect of NaCl during the pyrolysis, which was previously reported in solution-based syntheses and was maintained in TAMS [91,92].

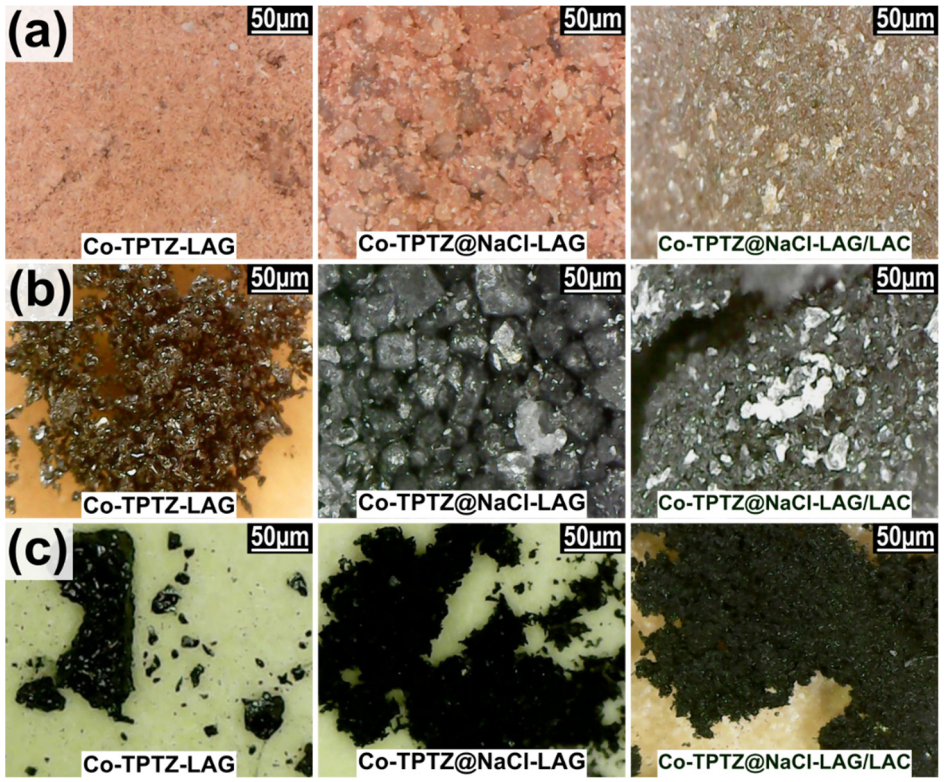

Figure 5. Optical microscopy images of (a) catalyst precursors, (b) pyrolysed precursors, and (c) acid-washed Co-N-C catalysts.

7.1.2 TAMS effect on morphology and composition of Co-N-C catalysts

In PXRD analysis (Fig. 6a), templated catalysts show an intense peak at 26.5° (graphitic-C), which indicates the retention of carbon framework by NaCl during pyrolysis, leading to a higher degree of graphitization [96]. Furthermore, templated Co-N-C shows the lower intensity of metallic Co peaks (44.1°, 51.7°, and 75.9° (Co-cubic)), suggesting that TAMS partially inhibits the agglomeration of metal ions into nanoparticles, which was assigned to the template-induced stabilisation of the chelated Co ions.

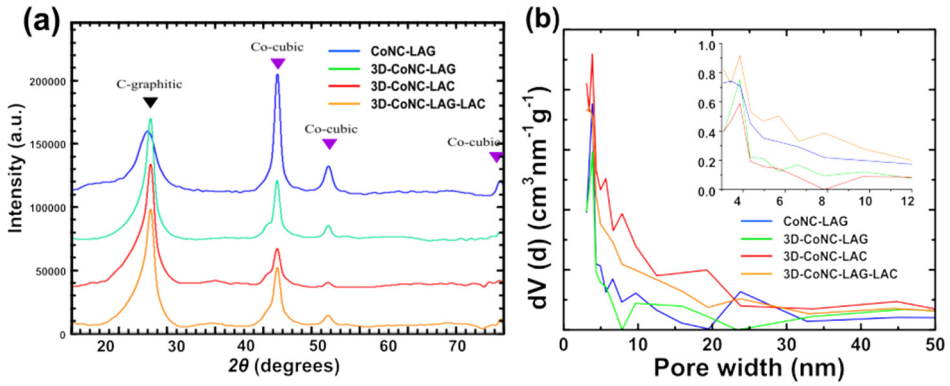

Figure 6. (a) PXRD patterns of synthesised catalysts; (b) Pore size distribution among the Co-N-C catalysts.

N_2 physisorption analysis (Fig. 6b) results indicate that the TAMS approach significantly improved the porosity of the resulting catalysts. All catalysts possess a mixed meso- and microporosity range of 1-30 nm with average pore sizes (APS) at ~2 nm. However, templated catalysts **3D-CoNC-LAC** and **3D-CoNC-LAG-LAC** showed (Table 3) the highest surface area (S_a) and total pore volume (V_{tot}), enabling more efficient charge transfer and mass transport in catalysis [97].

Table 3. Porosity characteristics of the obtained Co-N-C catalysts.

Catalyst	S_a (m^2 g^{-1})	V_{tot} (cm^3 g^{-1})	*APS* (nm)
	(0.02 – 0.2)	***0.97***	
CoNC-LAG	286	0.29	2.0
3D-CoNC-LAG	263	0.25	1.9
3D-CoNC-LAC	490	0.55	2.2
3D-CoNC-LAG-LAC	406	0.45	2.2

Morphological assessment of catalysts via TEM (Fig. 7a) confirmed a higher concentration of Co agglomerates in a densely packed **CoNC-LAG** carbon matrix, resulting in decreased exposure of active sites. Furthermore, the templated catalysts, **3D-CoNC-LAG**, **3D-CoNC-LAC**, and **3D-CoNC-LAC**, demonstrated a cross-linked sheet-like structure with an improved active surface exposure. The particle size distribution analysis (Fig. 7a (inset)) suggested that templating results in a smaller average size of Co particles – for **CoNC-LAG** and **3D-CoNC-LAG** (14-16 nm) compared to **3D-CoNC-LAC** and **3D-CoNC-LAG-LAC** (12 and 9 nm, respectively). Smaller sizes of Co particles effectively empower OER activity without blocking the pores and hindering the mass

transfer [98]. Furthermore, HR-TEM images of Co nanoparticles (Fig. 7b) indicate that agglomerates are coated with multilayer hollow carbon shells, protecting Co nanoparticles from corrosion and oxidation during harsh catalysis conditions [99]. Thus, TEM imaging further confirmed improved morphological parameters of catalysts via TAMS.

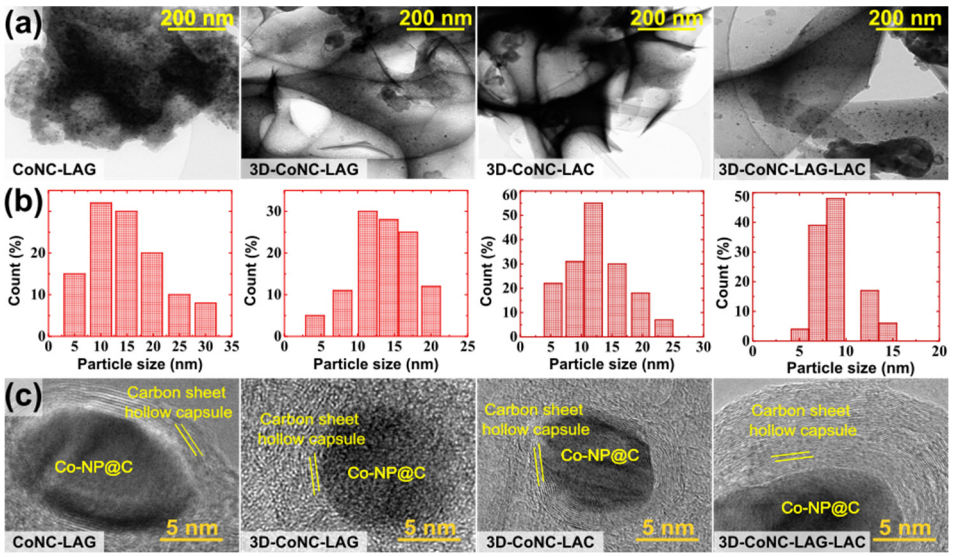

Figure 7. (a) TEM images and particle size distribution of Co-N-C catalysts; (b) HR-TEM images of Co nanoparticles coated by carbon sheets forming hollow nanocapsules.

The total surface content (Table 4) of four elements (Co, N, C, and O) indicated that the templated catalysts showed increased surface content of N with the highest N/C ratio (10.7%) in **3D-CoNC-LAG-LAC**, suggesting an efficient formation of C/N matrix for active CoN_x sites [100]. Furthermore, non-templated **CoNC-LAG** demonstrated a higher concentration of Co-species both on the catalyst surface (0.79 at.%) and in bulk (12.25 wt.%), which was supported by PXRD and TEM results, indicating the presence of a higher quantity of Co agglomerates. Thus, Co agglomerates greatly contribute to the total cobalt content in **CoNC-LAG** without finding significant use in oxygen electrocatalysis.

Table 4. Elemental composition of catalyst materials determined by XPS and MP-AES.

Catalyst	Surface elemental composition (at.%)				Bulk metal composition (wt.%)
	C	N	O	Co	Co
CoNC-LAG	85.87	4.1	7.63	0.79	12.35 ± 0.11
3D-CoNC-LAG	86.97	7.2	5	0.52	5.55 ± 0.05
3D-CoNC-LAC	88.75	5.99	4.14	0.47	4.69 ± 0.02
3D-CoNC-LAG-LAC	84.32	9.05	5.07	0.75	5.70 ± 0.04

Deconvoluted N 1s XPS spectra (Fig. 8b) of the obtained catalysts demonstrated the presence of active N-species: pyridinic (~398.4 eV), graphitic (~400.5 eV), and Co-N_x (~399.4 eV) [101]. Further, active metal single-atom sites – Co-C and Co-N_x were indicated at 779.8 and 781.8 eV upon deconvolution of Co 2p spectra [102].

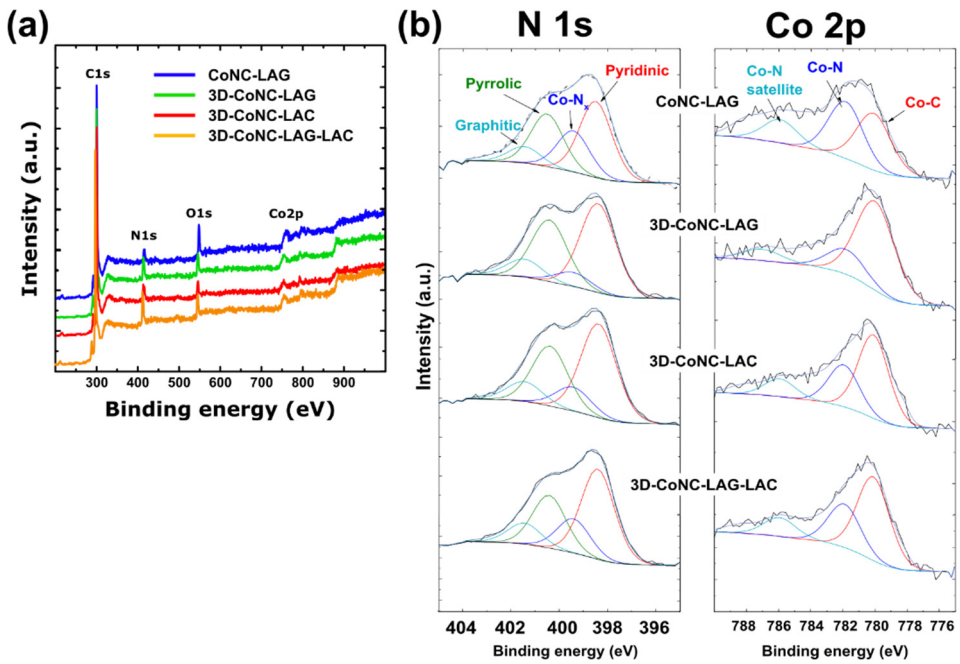

Figure 8. (a) Survey spectra of Co-N-C series; (b) Deconvoluted high-resolution N 1s and Co 2p photoelectron spectra of CoNC catalysts.

Among the catalysts, **3D-CoNC-LAG-LAC** showed the highest concentration of ORR-active N- and Co-species (Fig. 9a,b) with the highest Co/C ratio (~0.9%). Moreover, **3D-CoNC-LAG-LAC** showed the highest concentration of active Co-N_x species (1.49 at.%). Notably, the one-step LAG/LAC TAMS demonstrated the lowest concentration of Co-N_x, indicating that the grinding/compression techniques alone cannot provide sufficient energy to form Co-TPTZ effectively. Therefore, the two-step processing of 3D-CoNC-LAG-LAC yielded a higher concentration of active sites. The observed effect was attributed to improved pyrolysis stability due to better packing after the compression.

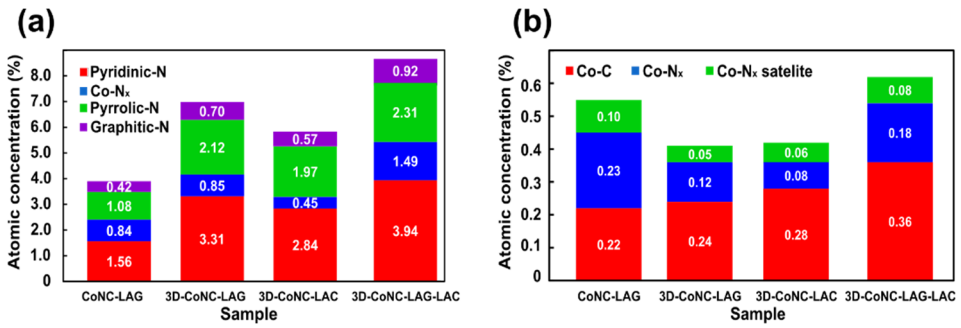

Figure 9. (a) The distribution of nitrogen species; (b) The distribution of single-atom Co-species.

Overall, the surface composition analysis demonstrated that the TAMS approach effectively enhances the N-content along with the concentration of ORR-active N/Co-N_x species.

7.1.3 TAMS effect on catalytic activity of Co-N-C catalysts

Ultimately, catalytic activity is one of the key determinants of TAMS effectiveness. Thus, the prepared catalysts were evaluated for oxygen electroactivity using the rotating disk electrode technique. RDE data for ORR (Fig. 10a) demonstrated that **3D-CoNC-LAG-LAC** had the highest ORR activity with an ORR onset potential value of 0.98 V and a half-wave potential value of 0.83 V, which is comparable to the recently reported results for Co-N-C materials [103]. Enhanced ORR electroactivity was attributed to TAMS-induced highly porous structure in combination with an abundance of ORR-active sites, as evidenced by BET, SEM, and XPS. Furthermore, the catalysts' OER activity was investigated in the potential range of 1–1.8 V vs. RHE (Fig. 10b) to achieve the benchmark OER current density of 10 mA cm^{-2} ($E_{j=10}$). The lowest OER was achieved by **3D-CoNC-LAG-LAC** at 1.70 V vs. RHE. The observed OER activity of **3D-CoNC-LAG-LAC** was associated with small Co nanoparticles, which are highly accessible due to improved porosity.

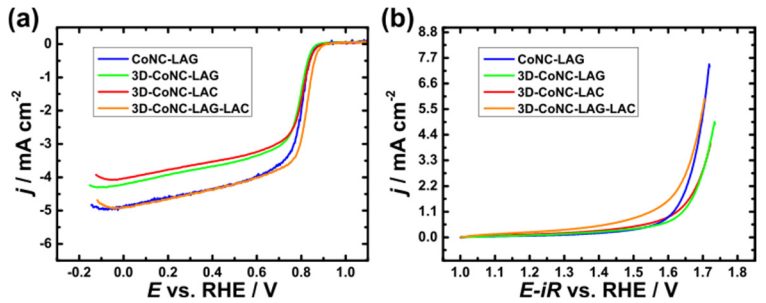

Figure 10. (a) ORR polarisation curves obtained for all CoNC catalyst materials in O_2-saturated 0.1 M KOH at 1600 rpm; (b) OER polarisation curves recorded in Ar-saturated 0.1 M KOH; v = 10 mV s^{-1}.

The kinetic parameters of the electrocatalysis were extracted from RDE data (Table 5). After Tafel analysis for the ORR mechanism insight, the Tafel slope values identify the first electron transfer as the rate-determining step of ORR. Furthermore, the electron transfer number, calculated from the K-L equation, was n = 4 for **3D-CoNC-LAG-LAC**, indicating that the ORR proceeds to water formation. Best-performing **3D-CoNC-LAG-LAC** showed the lowest overall bifunctional ORR/OER activity with ΔE = 0.908 V, calculated using the equation: $\Delta E = E_{j=10} - E_{1/2}$.

Table 5. Summary of electrokinetic parameters of Co-N-C catalysts.

Catalyst	$E_{1/2}$ (V vs. RHE)	E_{on} (V vs. RHE)	n	ORR Tafel (mV dec^{-1})	$E_{j=10}$ (V vs. RHE)	ΔE (V)
CoNC-LAG	0.788	0.960	3.1	-59	1.73	0.942
3D-CoNC-LAG	0.778	0.923	3.4	-37	1.80	1.022
3D-CoNC-LAC	0.791	0.935	3.5	-61	1.80	1.009
3D-CoNC-LAG-LAC	0.812	0.978	4.0	-47	1.72	0.908

Finally, the stability of the best-performing **3D-CONC-LAG-LAC** was assessed by chronoamperometry (Fig. 11). During the stability test, the catalysts showed a highly stable ORR current for over 8 hours of continuous operation. During the OER, a catalyst exhibited a current decay due to the blockage of the active sites by gas bubbles, which stopped after ~3000 s. Then, current density remained stable, with the **3D-CONC-LAG-LAC** catalyst exhibiting stable electrocatalytic performance towards OER for the next 7.5 hours.

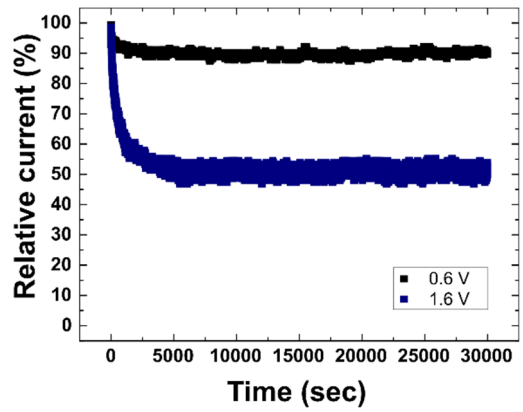

Figure 11. Chronoamperometric analysis for **3D-CoNC-LAG-LAC** at the potential of 0.6 V for ORR and 1.6 V for OER.

To sum up, the observed promising bifunctionality of **3D-CoNC-LAG-LAC** proves TAMS efficiency for **(1)** improving the porosity and active site accessibility, **(2)** enhancing the density of active nitrogen species, and **(3)** effectively stabilising N-coordinated metal ions for an improved formation of active single-atom sites. The investigation of sacrificial NaCl templating via mechanosynthesis in this work laid the groundwork for further studies to advance TAMS towards catalysts with better bifunctionality. Most importantly, with TAMS, the above-mentioned improvements were achieved in an inexpensive and sustainable way. The sustainability and cost-efficiency of TAMS will be discussed in detail in Section 7.4.

7.2 TAMS for bifunctional Fe-N-C catalysts

7.2.1 Synthesis of Fe-N-C catalysts via TAMS

The study on TAMS for Co-N-C, although successful, showcased several shortcomings to address: **(1)** Cobalt is a critical raw material [104] that should be replaced for better sustainability, and **(2)** A more preferred one-step processing via LAG/LAC did not provide enough energy to efficiently form Co-TPTZ polymer. Thus, the identified drawback of the Co-N-C study served to map further improvements of the TAMS approach. In this study, TAMS was upgraded by replacing cobalt with more abundant ORR/OER active iron (Fe) [105]. Using Fe also lowers the energy required for Fe-TPTZ formation, enabling one-step synthesis, as the TPTZ ligand is a known Fe detection agent due to its high affinity to $Fe^{2+/3+}$ cation [106].

At first, the Fe-TPTZ polymer was synthesised via mechanosynthesis using TPTZ, $FeCl_3 \cdot 6H_2O$ and 40 µL of EtOH. After mechanochemical processing, a distinct colour change from pale yellow to ink blue was observed, suggesting

Fe-TPTZ formed with an estimated poly-coordinate structure depicted in Fig. 12a. Comparative PXRD further confirms the structural change by the absence of characteristic peaks of TPTZ and $FeCl_3x6H_2O$ in the product's XRD pattern (Fig. 12b).

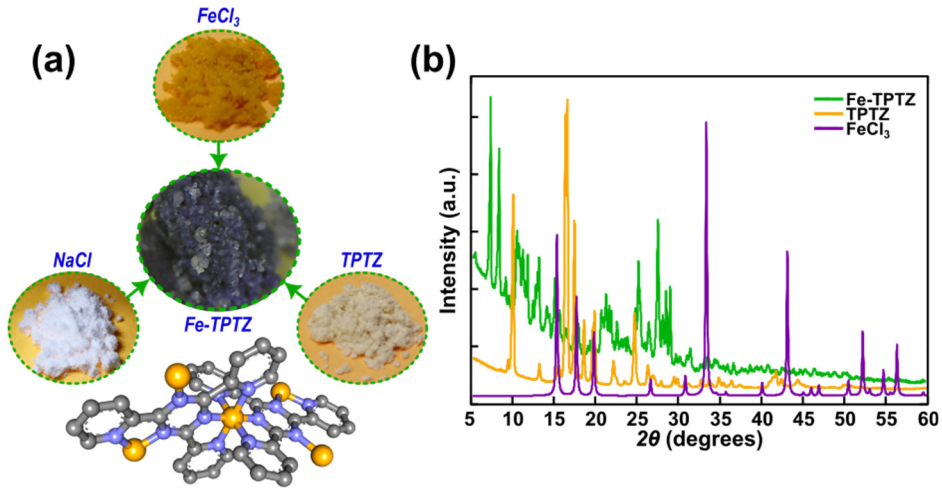

Figure 12. (a) Fe-TPTZ complex mechanosynthesis and suggested structure; (b) Comparative PXRD reaction precursors and Fe-TPTZ.

After Fe-TPTZ formation was confirmed, TAMS protocols were applied to synthesise three different Fe-N-C catalysts (Fig. 12) by varying synthetic conditions: **FeNC-LAG**, **3D-FeNC-LAG**, and **3D-FeNC-LAC**.

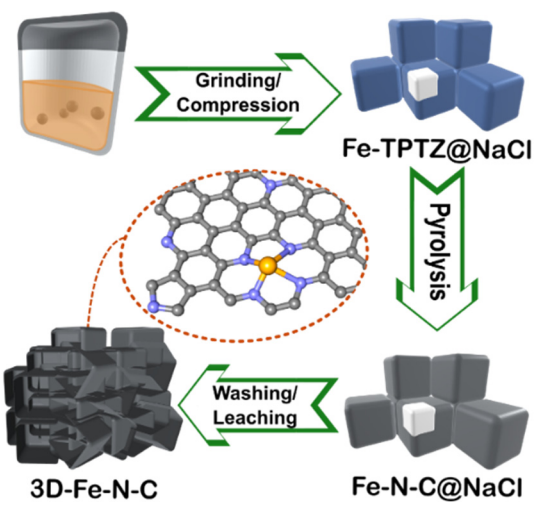

Figure 12. Schematic depiction of the TAMS for Fe-N-C.

Additionally, in this work, the pyrolysis protocol was modified by increasing the temperature to 800 °C with a faster ramping of 50 °C per minute to perform rapid pyrolysis, which decreases the heat treatment time, hence energy and time expenses. Furthermore, at 800 °C, the NaCl template gains the additional role of a molten-salt solvent – liquefied NaCl becomes a highly polar medium, allowing the movement of Fe-cations towards N-species for improved coordination and FeN_x single-site formation [107].

After TAMS and rapid pyrolysis, microscopy images of templated catalysts demonstrated the homogeneous inclusion of NaCl into the Fe-TPTZ framework (Fig. 14a,b), ensuring the stabilisation of Fe-TPTZ complexes as it was observed in the previous study on Co-N-C. Upon washing and leaching (Fig. 14c), templated catalysts demonstrated hierarchically porous open-frame 3D structures, which is conventionally achieved using carbon supports [108]. Similar morphological features were observed after SEM imaging (Fig. 14d), where templated catalysts showed a highly porous open matrix of cross-linked graphene sheets.

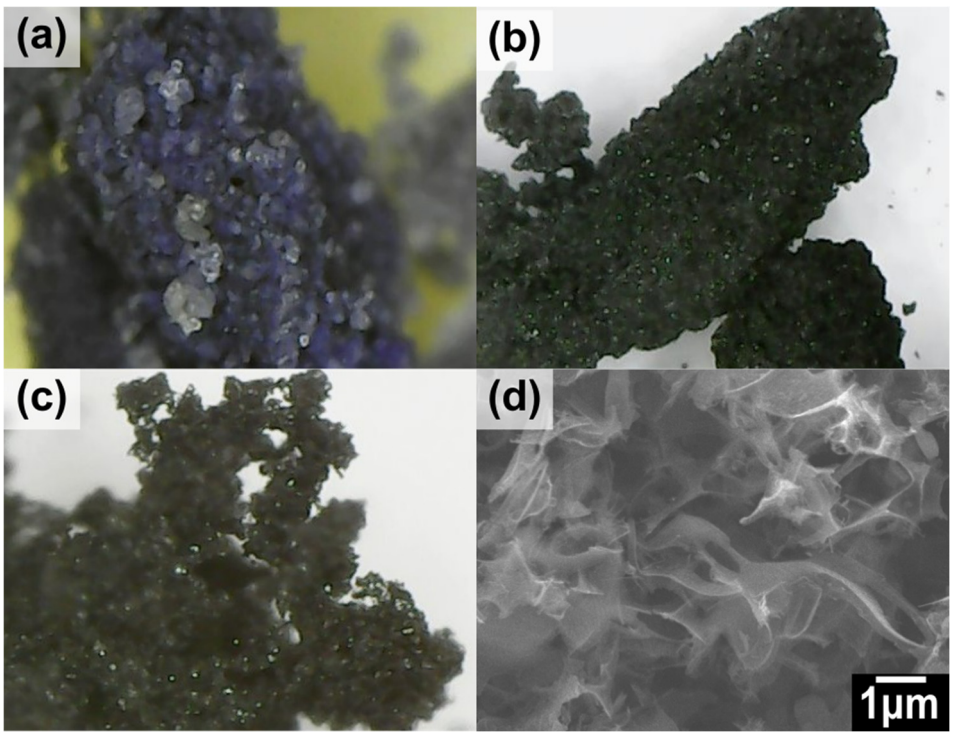

Figure 14. Optical microscopy images of templated catalysts on the example of 3D-FeNC-LAG: (a) After TAMS; (b) Pyrolysed; (c) Washed/Leached; (d) SEM image of 3D-FeNC-LAG

7.2.2 TAMS effect on morphology and composition of Fe-N-C catalysts

Similarly, the template-induced enhanced porosity was confirmed by the N_2 physisorption analysis. First, from a Type IV hysteresis loop shape adsorption-desorption isotherms (Fig. 15 (inset)), it was evident that the templated Fe-N-C catalysts contained both micro- and mesopores, which facilitate the charge and mass transfer. Pore size distribution (Fig. 15) showed that micropores and mesopores were primarily distributed over 1.2–2 nm and 2–34 nm, with an average pore size of 3.45 nm and 2.93 nm for **3D-FeNC-LAG** and **3D-FeNC-LAC**, respectively.

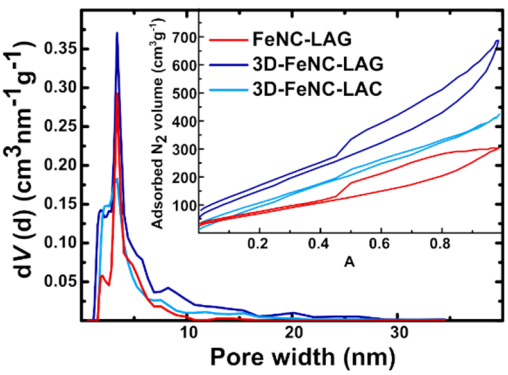

Figure 15. Pore size distribution curves and nitrogen adsorption-desorption isotherms (inset) of Fe-N-C catalysts.

Furthermore, templating significantly improved the surface area of catalysts (Table 6). **3D-FeNC-LAG** showed the largest surface area (563 m^2 g^{-1}), followed by **3D-FeNC-LAC** (430 m^2 g^{-1}) while non-templated **FeNC-LAG** showed values of only 269 m^2 g^{-1}. Additionally, templated catalysts demonstrated the highest density of catalysis-enhancing micropores and mesopores and the highest total pore volume [97].

Table 6. Porosity parameters determined from N_2 physisorption analysis.

Sample	Surface area (S_{BET} / m^2 g^{-1})	Total pore volume (cm^3 g^{-1})	Meso S_a (m^2 g^{-1})	Micro S_a (m^2 g^{-1})
3D-FeNC-LAG	563	0.97	381	111
3D-FeNC-LAC	430	0.63	269	45
FeNC-LAG	269	0.46	217	24

In PXRD analysis (Fig. 16), each catalyst demonstrated a distinct peak at 26° (002), suggesting their graphitic morphology [109]. However, graphite peaks of the compressed **3D-FeNC-LAC** were broader and of lower intensity, hinting at a low degree of graphitisation. Furthermore, **3D-FeNC-LAC** exhibited a set of peaks of iron species at 44.3° (α-Fe), 35.5° (Fe_3O_4), and several peaks from 39° to 45° (Fe_3C) (Fig. 16 (inset)), which appeared in **3D-FeNC-LAG** with significantly lower intensity. Lower graphitisation and abundance of Fe-clusters in **3D-FeNC-LAC** were linked to low reaction homogeneity during compression and poor access to metal clusters by acid due to dense packing.

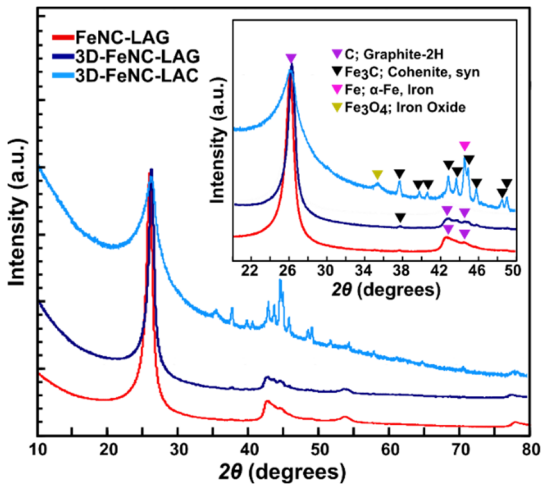

Figure 15. PXRD patterns of FeNC-LAG, 3D-FeNC-LAG, and 3D-FeNC-LAC and magnified region (inset).

In XPS, deconvoluted N 1s spectra (Fig. 17a) suggested the presence of active N-species (Fe-N_x, Pyrrolic, Pyridinic, Graphitic), while deconvoluted Fe 2p (Fig. 17b) indicated the presence of active single-atom Fe species (Fe-C_x at 714 eV, Fe-N_x 712 eV). Additionally, Fe^{3+} and Fe^{2+} oxides were identified on the surface of all samples at 710 and 709 eV, respectively [110,111]. Although oxides bear no use in ORR, their efficiency in OER can contribute significantly to the overall bifunctionality of the catalysts.

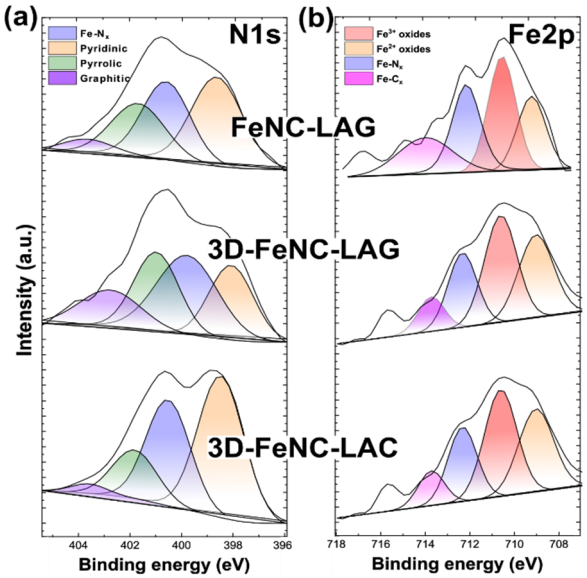

Figure 17. Deconvoluted high-resolution (a) N 1s and (b) Fe 2p photoelectron spectra of Fe-N-C.

Furthermore, the surface elemental composition (Table 7) suggested an improved N-doping with templated catalysts with the highest N-content in 3D-FeNC-LAG (7.4 at.%). Notably, **3D-FeNC-LAG** showed a high bulk metal composition of 1.471 wt.%. At the same time, PXRD did not detect significant peaks of Fe particles in PXRD, suggesting the atomic dispersion of most iron in the active form of Fe-N_x and Fe-C_x [112]. In contrast, compression-prepared 3D-FeNC-LAC showed the largest share of iron (9.3 wt.%) in alignment with PXRD results.

Table 7. Bulk composition of Fe (wt.%), and surface elemental (at.%) of C/N/O/Fe.

Catalyst	Fe bulk (wt.%)	Surface elemental composition (at.%)			
		C	N	O	Fe
FeNC-LAG	0.960	93.2	1.4	4.6	<1%
3D-FeNC-LAG	1.471	92.0	3.0	4.4	<1%
3D-FeNC-LAC	9.276	87.0	7.4	4.9	<1%

Morphology investigation using STEM (Fig. 18a) indicated that the **3D-FeNC-LAG** accommodated a lower quantity of Fe nanoparticles with an average size

of 27.35 nm, which were sparsely distributed in the carbon matrix (Fig. 18b). In contrast, STEM images of compression-derived **3D-FeNC-LAC** (Fig. 18 e) showed a high density of Fe nanoparticles with a larger average size of 32.67 nm (Fig. 18f). Notably, upon closer look, **3D-FeNC-LAG** revealed a high density of atomically dispersed iron clusters integrated into the porous carbon matrix (Fig. 18c), suggesting the high accessibility of these single-atom sites for improved ORR performance [113]. On the contrary, **3D-FeNC-LAC** showed very few single-atom sites (Fig. 18g), which could hinder its ORR activity. Furthermore, magnified STEM imaging (Fig. 18d) showed that particles in 3D-FeNC-LAG were confined in a carbon core-shell (d=2.13 Å, Graphite (001)), improving their performance in OER and stability to oxidation. In 3D-FeNC-LAC, STEM images of nanoparticles (Fig. 18h) revealed the oxide-covered Fe_3C structure of particles surrounded by carbon layers. Fe oxides and Fe_3C are expected to facilitate OER and ORR, respectively. However, their overabundance and relative bulkiness might hinder catalysis by lowering the accessibility of active sites and mass/charge transfer [114].

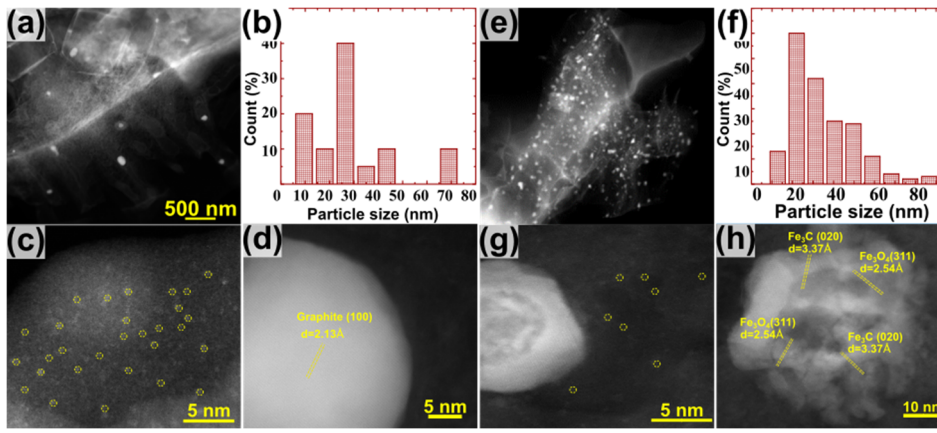

Figure 18. STEM images of (a) D-FeNC-LAG and (e) 3D-FeNC-LAC. Particle size distribution of (b) 3D-FeNC-LAG and (f) 3D-FeNC-LAC. Magnified regions of STEM images of (c,d) 3D-FeNC-LAG and (g,h) 3D-FeNC-LAC.

7.2.3 TAMS effect on catalytic activity of Fe-N-C catalysts

To assess the effect of TAMS on catalytic performance, RDE studies were conducted on prepared Fe-N-C catalysts to evaluate their ORR activity in an alkaline medium. In RDE (Fig. 19a), milling-derived **3D-FeNC-LAG** demonstrated an outstanding ORR activity with E_{on} = 1.00 V, $E_{1/2}$ = 0.85 V, and larger limited current density (5.0 mA cm^{-2}), which hints at a better electron and mass transfer induced by higher porosity.

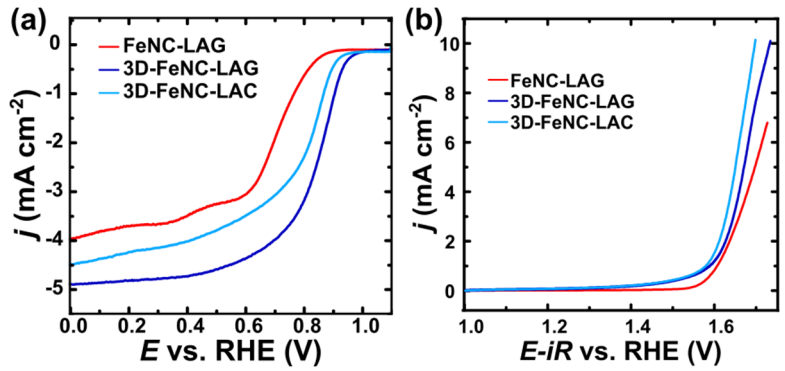

Figure 19. (a) ORR polarisation curves of FeNC-LAG, 3D-FeNC-LAG, and 3D-FeNC-LAC in O2-saturated 0.1 M KOH solution at a rotation rate of 1600 rpm. (b) OER polarisation curves were recorded for FeNC-LAG, 3D-FeNC-LAG, and 3D-FeNC-LAC in an Ar-saturated 0.1 M KOH solution at a rotation rate of 1600 rpm.

Furthermore, in ORR Tafel analysis (Table 8), the **3D-FeNC-LAG** showed the lowest Tafel slope value (74 mV dec^{-1}), implying favourable ORR kinetics, while the K-L analysis indicated primarily the $4e^-$ ORR pathway for **3D-FeNC-LAG**. Thus, in the RDE experiment, **3D-FeNC-LAG** stands out as a promising ORR catalyst.

Table 8. Summary of ORR performance characteristics of synthesised catalysts.

Sample	$E_{1/2}$ (V vs. RHE)	E_{on} (V vs. RHE)	n	ORR Tafel (mV dec^{-1})
FeNC-LAG	0.69	0.89	3.24	123
3D-FeNC-LAG	0.85	1.00	3.85	74
3D-FeNC-LAC	0.80	0.94	3.81	80

Further, the synthesised catalysts were assessed for OER using linear sweep voltammetry (LSV) in alkaline conditions. The catalysts were assessed in a potential range of 1-1.8 V vs. RHE to determine the potential required to reach a current density of 10 mA cm^{-2}. In OER (Fig. 19b), the compression-derived **3D-FeNC-LAC** showed the best performance with the lowest $E_{j=10}$ value of 1.70 V. Calculated kinetic parameters of OER (Table 9) further confirmed the superiority of the **3D-FeNC-LAC** in OER, which was attributed to the abundance of OER-active nanoparticles in the catalyst [115].

Table 9. Summary of OER performance characteristics of synthesised catalysts.

Sample	$E_{j=10}$ (V vs. RHE)	η_{OER} (V)	OER Tafel (mV dec^{-1})
FeNC-LAG	1.78	0.55	70
3D-FeNC-LAG	1.73	0.50	243
3D-FeNC-LAC	1.70	0.47	267

ORR and OER curves, combined in Fig. 20, indicate that **3D-FeNC-LAG** has the best bifunctionality (ΔE = 0.88 V), followed closely by **3D-FeNC-LAC** (ΔE = 0.90 V).

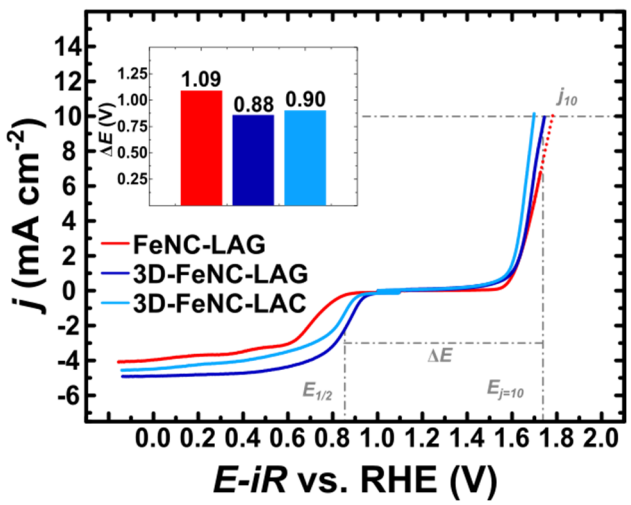

Figure 20. The overall polarisation curves of FeNC-LAG, 3D-FeNC-LAG, and 3D-FeNC-LAC within the ORR and OER potential window and the values of ΔE (inset).

Next, the best bifunctional **3D-FeNC-LAG** was tested in a Zn-air battery as the carbon paper-supported air cathode. As expected, **3D-FeNC-LAG** showcased an outstanding activity with the highest power density among all three catalysts (Fig. 21). Specifically, **3D-FeNC-LAG** showed a power density of 139 mW cm^{-2}, comparable to recent reports [116], outperforming the commercial PtRu/C catalyst with a power density of 120 mW cm^{-2}.

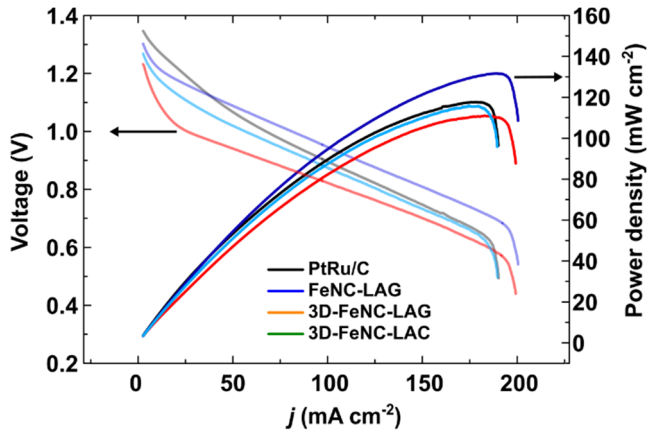

Figure 21. Power density curves for Fe-N-C and PtRu/C as catalysts on the air cathode (solid lines – power curves, hollow lines – polarisation curves).

The long-term performance of the **3D-FeNC-LAG**-driven ZAB was evaluated through galvanostatic charge-discharge cycling measurements at 5 mA cm^{-2} (Fig. 22). The battery showed a steady voltage-time profile in the potential range of 1.52 V without significant fluctuations for 60 hours. However, minor fluctuations were observed and assigned to zinc dendrites, causing internal short circuits and destabilising the battery. In contrast, the PGM-based catalyst started to malfunction after a few hours of work with significant voltage gaps between cycles (~2.4 V) compared to **3D-FeNC-LAG** voltage gaps of only 0.45 V, suggesting an outstanding stability of **3D-FeNC-LAG**-based battery.

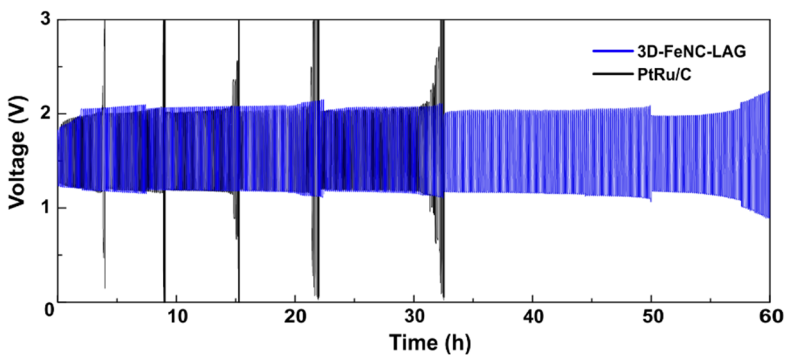

Figure 22. Galvanostatic charging/discharging cycling curves for 3D-FeNC-LAG and PtRu/C materials (blue and black lines, respectively) performed at 5 mA cm^{-2}.

The results of the electrochemical assessment demonstrated that the ORR/OER efficiency of TAMS-derived Fe-N-C catalysts was comparable to previously reported Fe-N-C catalysts [116]. The same can be said about the **3D-FeNC-**

LAG-driven battery performance. Thus, TAMS-derived catalysts showed comparable performance to the materials made by liquid-phase protocols, which fall far behind in cost and energy efficiency compared to TAMS (for details, Section 7.4).

In summary, the current study confirms that upgraded TAMS M-N-C synthesis further enhances essential catalyst characteristics for electrocatalysis. More specifically: **(1)** Upgrading TAMS with tailored rapid pyrolysis yielded an optimal ratio between ORR-active single-atom/nitrogen sites and OER-active nanoparticles for an improved bifunctionality (**3D-FeNC-LAG** ΔE = 0.88 V *vs.* **3D-CoNC-LAG-LAC** ΔE = 0.91 V). **(2)** Upgraded TAMS optimises the morphology of catalysts by yielding even better porosity parameters (**3D-FeNC-LAG** S_{BET} = 563 m^2 g^{-1} *vs.* **3D-CoNC-LAG-LAC** S_{BET} = 406 m^2 g^{-1}), increasing the wetting of the total surface, rendering the Fe-N_x sites accessible. **(3)** Employing Fe in TAMS for M-N-C improved the coordination efficiency, yielding a higher concentration of ORR-active Fe-N_x single-atom sites, which could be visually identified by STEM. **(4)** Rapid pyrolysis at 800 °C enabled NaCl salt-melt solvent, shortened the processing time, lowering energy expenses.

7.3 TAMS for bifunctional Fe/Ni-N-C catalysts

7.3.1 Synthesis of Fe/Ni-N-C catalysts via TAMS

Previous TAMS studies focused solely on the design of single-metal Co/Fe-N-C catalysts. Therefore, in this work, TAMS was tested for the production of bimetallic M-N-C catalysts, which are expected to have better bifunctionality due to a synergy between two metal centres [51]. Specifically, **3D-FeNC-LAG** showed good ORR activity compared to the catalyst's lower OER activity. Therefore, in addition to iron, nickel was added to form OER-active FeNi-nanoparticles, enhancing the OER activity [48]. Thus, by incorporating OER-active FeNi-nanoparticles and ORR-active Fe-N_x sites, this study aims to significantly improve the bifunctionality of the catalysts. Therefore, in this work, three different FeNi–N–C catalysts were prepared: **IroNi-1**, **IroNi-2**, and **IroNi-3D**, where 3D implies the templating. In all samples, the ratio of metals was significantly increased to achieve the abundance of FeNi particles.

First, the formation of FeNi-TPTZ was confirmed by reacting TPTZ with $FeCl_3 \cdot 6H_2O$ and $NiCl_2 \cdot 6H_2O$ in a ball mill. In previous studies on TAMS, LAC did not yield significant improvement to Fe/Co-N-C catalysts compared to LAG. Thus, in this work, LAG via ball milling is employed as the primary technique. After ball milling, the colour of the reaction mixture shifted from pale yellow to dark green powder, which was recrystallised needle-like green crystals, suggesting the formation of FeNi-TPTZ. (Fig. 23a) The comparative PXRD (Fig. 23b) further confirmed the structural change, showing the absence of the peaks associated with the reactants in the formed FeNi-TPTZ pattern.

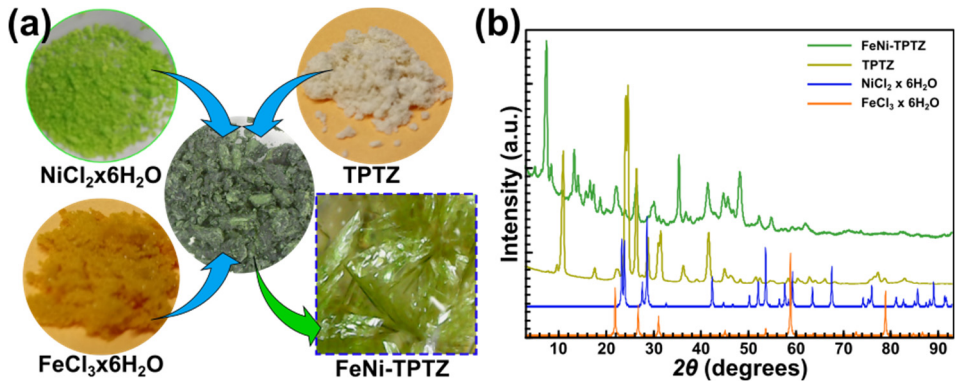

Figure 23. (a) Formation of the green FeNi-TPTZ complex after LAG with recrystallised FeNi-TPTZ; (b) Comparative PXRD of precursors and product.

In this study, it was imperative to ascertain the coordination of both Fe and Ni with TPTZ. Therefore, the coordination of TPTZ to Fe/Ni ions was additionally confirmed by comparative solid-state NMR (Fig. 24), where the FeNi-TPTZ spectrum showed characteristic peaks of Fe-TPTZ at 328, 231, 220, 199, 92, and 32 ppm, suggesting the presence of TPTZ-coordinated species. Furthermore, the characteristic peaks of the Ni-TPTZ spectrum were observed at 516, 327, 194, and 93 ppm, affirming the formation of the Fe and Ni-coordinated TPTZ complex.

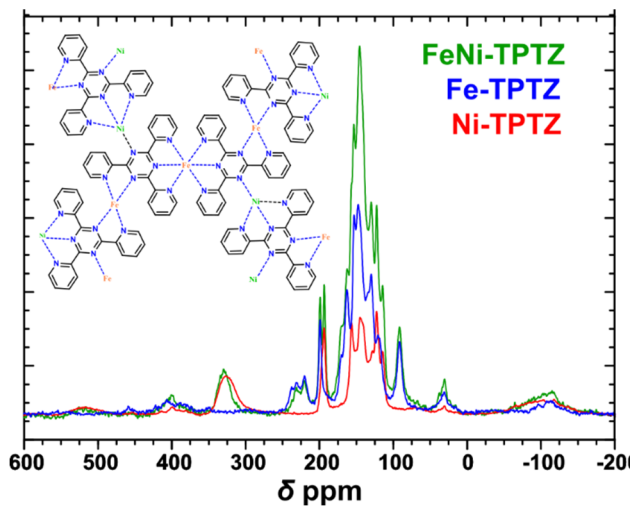

Figure 24. Solid-state NMR of Fe-TPTZ, Ni-TPTZ, and FeNi-TPTZ complex and its suggested structure (inset).

Inspired by the results of tailored pyrolysis for Fe-N-C, in this study, the TAMS approach was further enhanced by introducing a "two-stage pyrolysis" strategy. In this strategy, stage one focused on the Metal-TPTZ complex, which is pre-heated near the melting point to facilitate the coordination of ligands to metal ions in the liquid phase [117]. Stage two focused on activating the template by using it as a mixed-phase template. For that purpose, NaCl was replaced with KCl due to its lower melting point of 760 °C. At first, below 760 °C, KCl acts as a solid-phase template, supporting the porous framework of the resulting FeNi-N-C. Later, in the range of 760-800 °C, KCl becomes the liquid-phase polar medium – molten-salt solvent, facilitating Fe and Ni ions mobility for better coordination [118–120].

TGA was performed to develop the first stage of the two-stage pyrolysis (Fig. 25a), mimicking pyrolysis conditions to understand the behaviour of the FeNi-TPTZ complex at various temperatures. TGA was conducted on TPTZ and FeNi-TPTZ, showing improved stability of the coordination polymer in comparison to the pure ligand. Furthermore, TGA indicated that 300 °C is the optimal temperature for FeNi-TPTZ's non-destructive melting, establishing stage one's preheating temperature. Thus, by considering the melting points of the KCl template and FeNi-TPTZ, the two-stage pyrolysis strategy was designed as gradual heating to 300 °C and keeping at this temperature for 1 hour, then gradually increasing to 800 °C with one more hour dwelling. (Fig. 25b)

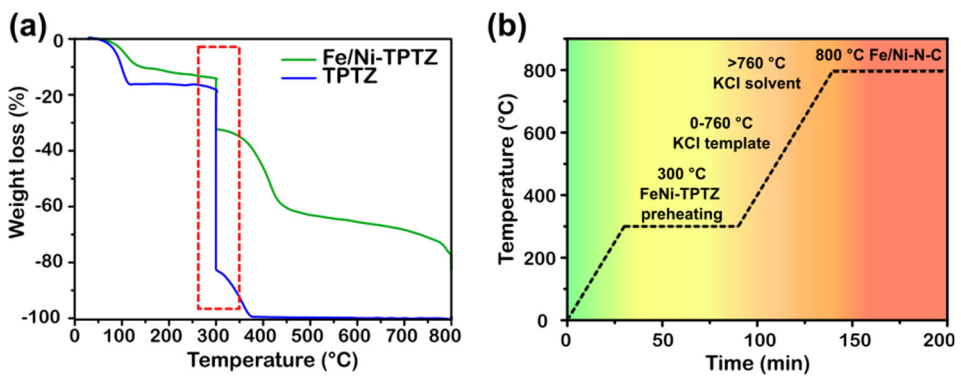

Figure 25. (a) TGA curves obtained for TPTZ and FeNi-TPTZ; (b) Pyrolysis protocol for FeNi-N-C synthesis.

In this strategy, exposure of FeNi-TPTZ to heat treatment is increased, risking the decomposition of the C/N component of the catalysts. Therefore, in addition to TPTZ, melamine was added to ensure efficient C/N doping. Furthermore, after pyrolysis, it was necessary to remove the sacrificial KCl template without harming the FeNi nanoparticles content, which is not possible with conventional acid leaching. Therefore, in this work, hydrothermal treatment of catalysts was used to remove KCl without destroying FeNi nanoparticles.

After incorporating the upgrades, the new TAMS protocol (Fig. 26) crystallised into a one-step template-assisted mechanosynthesis of FeNi-TPTZ-Melamine supported on KCl (FeNi-TPTZ-Mel@KCl). Next, the composite was subjected to two-stage pyrolysis to yield FeNi-N-C@KCl, which underwent hydrothermal treatment to remove the template and give **IroNi-3D**. For comparison, the non-templated catalyst **IroNi-2** was prepared to assess the effect of the template. Moreover, **IroNi-1** was prepared without adding a template and melamine to evaluate the influence of templating and melamine doping.

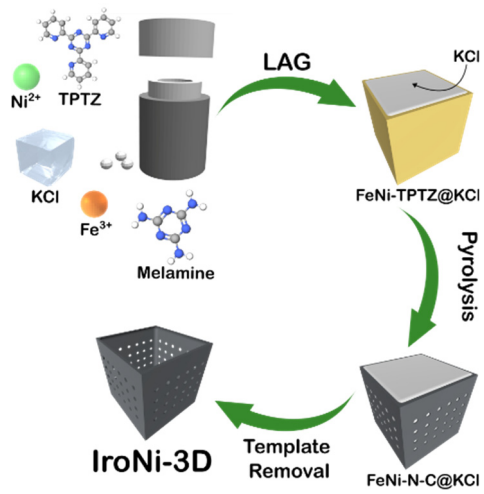

Figure 26. Schematic illustration of the upgraded TAMS protocol.

7.3.2 TAMS effect on morphology and composition of Fe/Ni-N-C catalysts

Microscopy imaging of mechanochemically treated and pyrolysed FeNi-TPTZ (Fig. 27a,b) revealed a homogeneous inclusion of KCl. As highlighted in previous studies, even dispersion of the template remains a crucial part of the TAMS approach, stabilising the FeNi-TPTZ complex in pyrolysis, resulting in enhanced porosity and increased exposure of active sites. Furthermore, the microscopy image of hydrothermally treated **IroNi-3D** (Fig. 27c) demonstrated a porous open-frame 3D structure induced by the template.

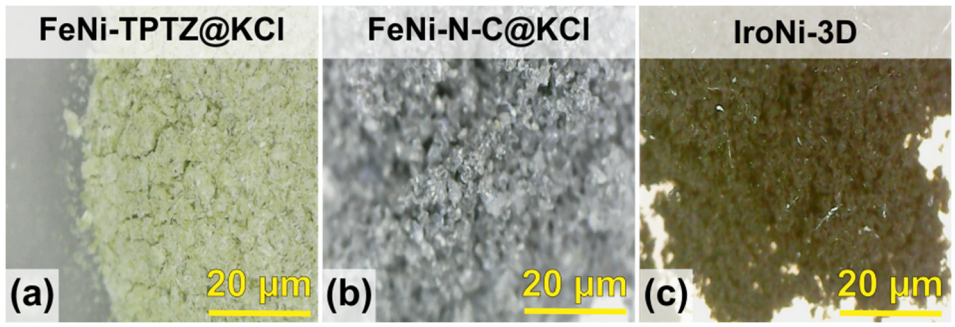

Figure 27. Microscopy images of IroNi-3D after different processing stages: (a) Synthesis; (b) Pyrolysis; (c) Washing.

The porosity of **IroNi-3D** was additionally confirmed by SEM images, showing a diversely porous open carbon matrix (Fig. 28a). Furthermore, the abundance of OER-active FeNi nanoparticles was detected in the **IroNi-3D** exposed on the carbon surface and distributed in the range of 10-30 nm (Fig. 26a). In contrast, template-free **IroNi-2** turned into closely packed carbon accommodating nanoparticles with a size of 20–60 nm (Fig. 28b). Lastly, template and melamine-free **IroNi-1** represented a dense carbon matrix with the inclusion of nanoparticle sizes spanning in the range of 20–140 nm (Fig. 28c). This suggests that template-induced mobility of Fe and Ni ions inhibits their confined agglomeration, resulting in smaller and well-dispersed nanoparticles, which, combined with porosity, improves their overall catalytic effect.

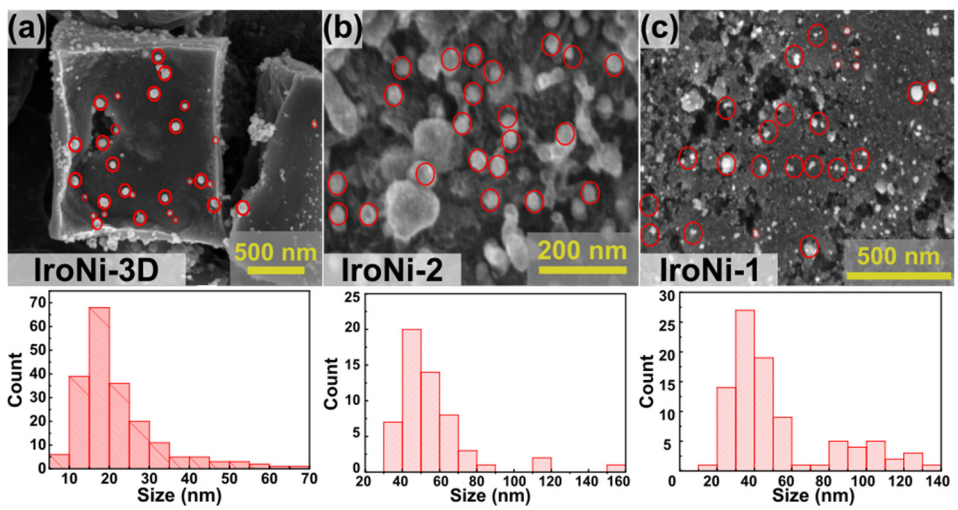

Figure 28. SEM images and corresponding particle size distribution of (a) IroNi-3D, (b) IroNi-2, and (c) IroNi-1.

The template-promoted porosity of FeNi-N-C catalysts was further evidenced by the N_2 physisorption. The materials exhibited a Type IV hysteresis loop shape of isotherms, indicating the presence of both micro- and mesopores in the range of 1.2–2 nm and 2.5–5 nm, respectively (Fig. 29).

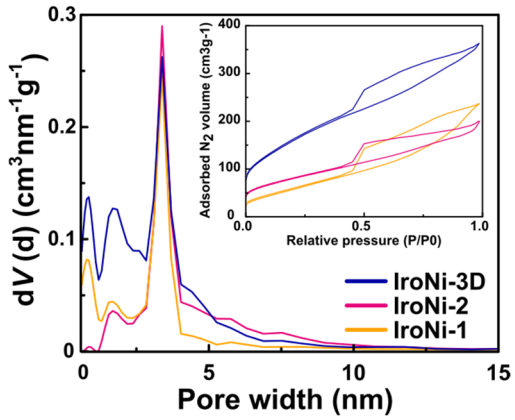

Figure 29. Pore size distribution of IroNi-series catalysts and adsorption-desorption isotherm (inset).

Furthermore, **IroNi-3D** demonstrated a great surface area of 570 m^2 g^{-1}, the highest among TAMS-derived catalysts (Table 10). In contrast, the surface area of **IroNi-2** and **IroNi-1** was in a significantly lower range of 200-300 m^2 g^{-1}. Moreover, the improved surface area of mesopores (194 m^2 g^{-1}) and micropores (288 m^2 g^{-1}) in **IroNi-3D** promises improved kinetics and mass/charge transfer, further supporting the efficiency of KCl mixed-phase templating.

Table 10. Specific porosity parameters of the IroNi catalysts determined from N_2 physisorption.

Sample	Surface area (S_{BET} / m^2 g^{-1})	Total pore volume (cm^3 g^{-1})	Mesopores S_a (m^2 g^{-1})	Micropores S_a (m^2 g^{-1})
IroNi-3D	570	0.54	194	288
IroNi-2	208	0.35	156	29
IroNi-1	284	0.29	113	148

Furthermore, the nature of the observed nanoparticles was determined by PXRD, which confirmed the presence of OER-active $FeNi_3$ alloy (Taenite; 43.5°, 50.5°, 74.5°, and 91°) in abundance in each catalyst (Fig. 30a), identifying hydrothermal treatment as an efficient approach to retain OER-active alloys. The abundance of metal particles reduced the prominence of the carbon component (Graphite-2H; 26°) in the PXRD of the catalysts. However, this is not expected to affect catalytic activity, provided the active species remain well-exposed on the porous carbon matrix. Apart from FeNi-nanoparticles, HAADF-STEM elemental mapping suggested the successful incorporation of single-atom species in the templated **IroNi-3D**. (Fig. 30b-e) In the images, EDX analysis demonstrated the regions with an elevated concentration of Fe and Ni (Fig. 30c,e) incorporated within an evenly distributed C/N matrix (Fig. 30d), where characterised spots do not show distinguishable discernible boundaries/ edges, evidencing a dense concentration of single-atom sites.

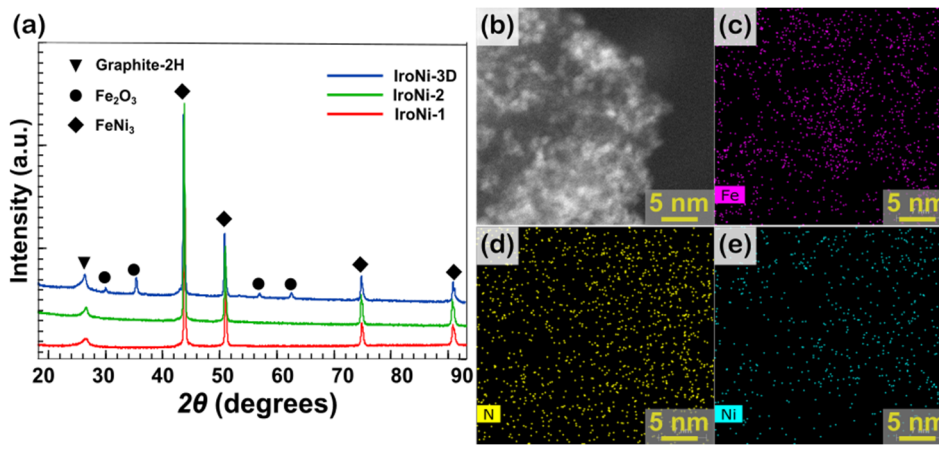

Figure 30. (a) XRD patterns of IroNi-3D, IroNi-2, and IroNi-1. (b) HAADF-STEM image of IroNi-3D accompanied by EDX elemental mapping images of (c) Fe (d) N (e) Ni.

On the surface, as determined by X-ray photoelectron spectroscopy, Ni and Fe represented a mixture of species. The Fe 2p XPS spectrum (Fig. 31) demonstrated the peaks of Fe^{2+} at 710.5 eV and 723.7 eV and Fe^{3+} at 712.2 and 725.5 eV and a peak at 705.0 eV assigned to Fe^0. The Ni 2p exhibited two spin-orbit peaks at 855.8 eV (Ni 2p3/2) and 873.4 eV (Ni 2p1/2), along with two satellite peaks, which can be attributed to Ni II. In line with previous studies, the results of XPS surface composition analysis confirmed the presence of FeNi alloy nanoparticles [121].

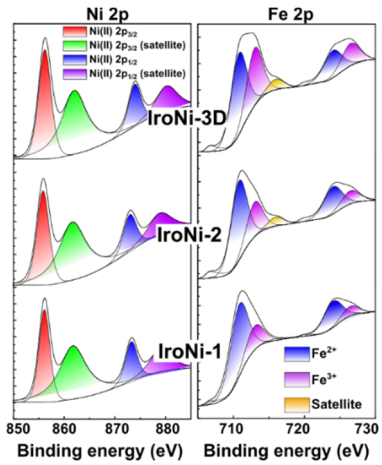

Figure 31. Deconvoluted high-resolution Ni 2p and Fe 2p photoelectron spectra.

IroNically, the surface content of C and N was found to be the lowest in the templated **IroNi-3D** – 52.6 and 2.4 at.%, respectively (Table 11). This can be explained by the abundance of metal exposed to the catalyst's surface, which had the highest Fe and Ni content – 2.3 and 14.3 at.%, respectively. In **IroNi-3D**, the bulk metal composition of Fe and Ni exceeded 20 wt.%, differing significantly from the surface composition, which was assigned not a lower homogeneity of the sample. Furthermore, **IroNi-2** demonstrated 8 wt.% more Fe and **IroNi-1** 8 wt.% more Ni. The observed discrepancy was assigned to the effect of the added melamine, providing more N-coordination sites to retain Ni.

Table 11. The bulk metal composition of Fe/Ni (wt.%) determined by MP-AES analysis, and the surface elemental composition (at.%) determined by XPS.

Catalyst	Surface elemental composition (at.%)					Bulk metal composition (wt.%)	
	C	N	O	Fe	Ni	Fe	Ni
IroNi-3D	52.6	2.4	28.4	2.3	14.3	21.345	20.686
IroNi-2	77.6	3.0	13.2	2.1	4.1	21.636	29.788
IroNi-1	78.0	3.0	14.3	1.3	3.4	29.230	21.065

Furthermore, as determined by the deconvoluted N 1s, only ~20% of all nitrogen in IroNi catalysts form the M– N_x sites (Table 12). These results imply that most of the metals agglomerated into OER-active nanoparticles. While the reduced surface concentration of M– N_x sites might lower the ORR efficiency, ORR-active nitrogen species (pyridinic, graphitic, pyrrolic), comprising ~65% of all surface nitrogen, are expected to facilitate the ORR activity.

Table 12. The ratio of nitrogen species detected on the surface of the catalysts identified by deconvoluted N 1s spectra.

Catalyst	Nitrogen species ratio (%)				
	Pyridinic	Pyridinic	Pyrrolic	M-N_x	Other
IroNi-3D	25.44	15.21	22.12	22.84	14.40
IroNi-2	23.04	15.76	23.58	23.62	14.01
IroNi-1	25.57	17.08	24.27	20.41	12.57

7.3.3 TAMS effect on catalytic activity of Fe/Ni-N-C catalysts

The ORR activity of IroNi catalysts in an alkaline medium (0.1 M KOH) was evaluated by RDE. In ORR, all catalysts demonstrated a primarily $4e^-$ pathway with decent kinetics (Table 13). Among all IroNi catalysts, **IroNi-3D** showed the highest onset potential of 0.92 V vs. RHE and a half-wave potential of 0.82 V vs. RHE. (Fig. 30a) Furthermore, **IroNi-3D** showed a comparable activity to the commercial Pt/C catalyst. In this study, the **IroNi-3D** ORR activity was attributed to an improved electron and mass transfer due to its high porosity. Nevertheless, when compared to **3D-FeNC-LAG** ORR activity, it becomes evident that the approach must be optimised to accommodate more M-N_x sites for better ORR. OER activity of the catalysts was assessed by LSV measurements in a 0.1 M KOH solution. The electrodes were scanned within a potential range of 1.1 to 1.8 V vs. RHE to determine $E_{j=10}$ values. The LSV curves (Fig. 32b) indicated that all IroNi catalysts performed well in OER with $E_{j=10}$ values of **IroNi-2** (1.48 V vs. RHE), closely followed by **IroNi-1** and **IroNi-3D** (1.51 and 1.52 V vs. RHE, respectively). As expected, the abundance of FeNi alloy nanoparticles resulted in an outstanding OER performance in all IroNi catalysts, significantly outperforming the benchmark RuO_2.

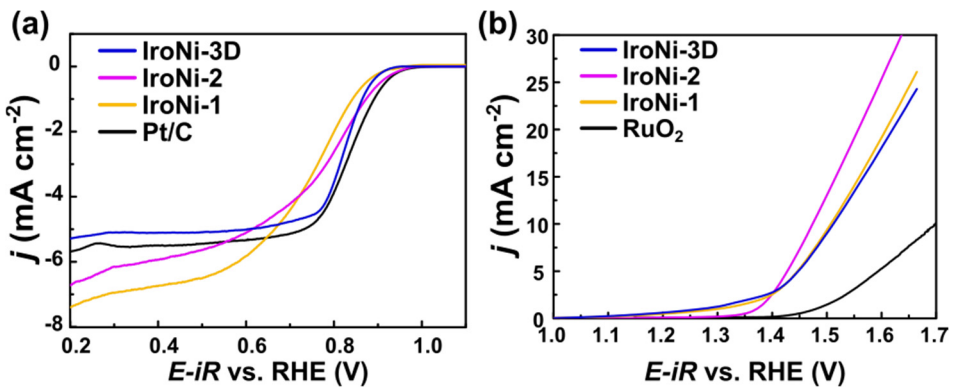

Figure 32. (a) ORR polarisation curves of the IroNi catalyst and benchmark Pt/C; (b) Linear sweep voltammetry curves of the IroNi catalyst and benchmark RuO_2.

Bifunctionality assessment (Fig. 33a) showed that the **IroNi-3D** showed the best ΔE among TAMS-derived catalysts – 0.70 V, closely followed by IroNi-2 (ΔE = 0.71 V). (Table 13) The results of the electrochemical assessment indicated that solid phase-derived **IroNi-3D** ORR/OER activity was comparable to previously reported liquid phase-derived FeNi-N-C catalysts [122]. Although the activity of **IroNi-2** was close to **IroNi-3D**, its lower ORR efficiency, along with lower porosity, might be unsuitable for application in ZAB. More specifically, lower porosity may hinder the wetting of the total surface, leading to the inaccessibility and inactivity of a significant portion of active sites. Next, **IroNi-3D** was applied in ZAB as a carbon paper-supported air cathode. In the ZAB test, **IroNi-3D** demonstrated an outstanding performance with a power density of 144 mW cm^{-2} at 201 mA cm^{-2} (Fig. 33b), comparable with previously reported ZAB catalysts [122]. Furthermore, **IroNi-3D** significantly outperformed the commercial benchmark PtRu/C, which reached only 101 mW cm^{-2} at 153 mA cm^{-2}. The charge-discharge polarisation curves showed that **IroNi-3D** exhibited an open-circuit voltage of 1.30 V, comparable to the PGM-based benchmark – PtRu/C (1.35 V).

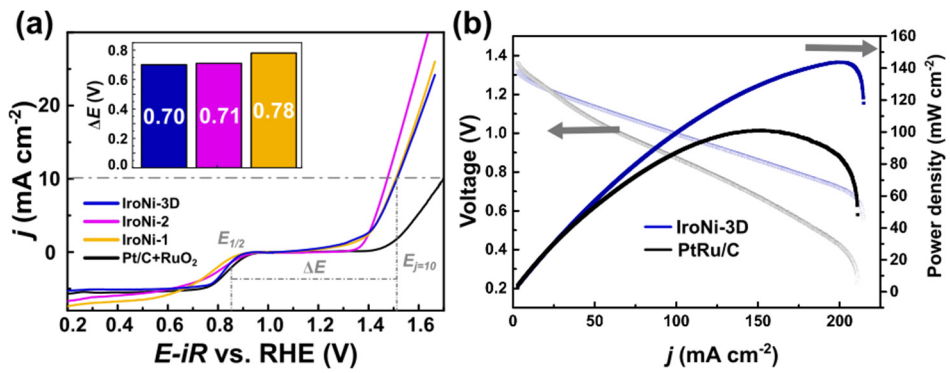

Figure 33. (a) The overall polarisation curves of IroNi-3D, IroNi-2, and IroNi-1 within the ORR and OER potential window and the values of ΔE (inset); (b) Power density curves for IroNi-3D and benchmark Pt-RuO_2 as the air cathode (solid lines – power curves and hollow lines – polarisation curves).

Table 13. Electrochemical performance parameters of IroNi catalsyst.

Sample	$E_{1/2}$ (V vs. RHE)	E_{on} (V vs. RHE)	n	ORR Tafel (mV dec^{-1})	$E_{j=10}$ (V vs. RHE)	η_{OER} (V)	ΔE (V)
IroNi-3D	0.82	0.92	3.42	53	1.52	0.29	0.70
IroNi-2	0.77	0.93	3.66	87	1.48	0.25	0.71
IroNi-1	0.73	0.89	3.72	68	1.51	0.28	0.78
Pt/C+RuO_2	0.85	0.94	-	-	1.70	0.47	0.85

The long-term performance of **IroNi-3D**-driven ZAB was checked by galvanostatic charge-discharge cycling at 5 mA cm^{-2} (Fig. 34), demonstrating a steady voltage–time profile without major fluctuations for over 22 hours operating in the range of 0.75–1.75 V, with the voltage gap increasing from 0.46 to 1.08 V. As previously determined, minor fluctuations arise from zinc dendrites, leading to internal short circuits and overall battery instability. It is important to note that this study on developing the TAMS approach did not involve optimising the ZAB conditions and setup and shall be addressed in a different study. Nevertheless, at the same testing condition, the benchmark PtRu/C catalyst destabilisation was observed after only 8 hours of operation, reaching a voltage gap of 3 V. The results of the ZAB test demonstrated a superior activity and stability of **IroNi-3D** compared to benchmark PGM catalysts.

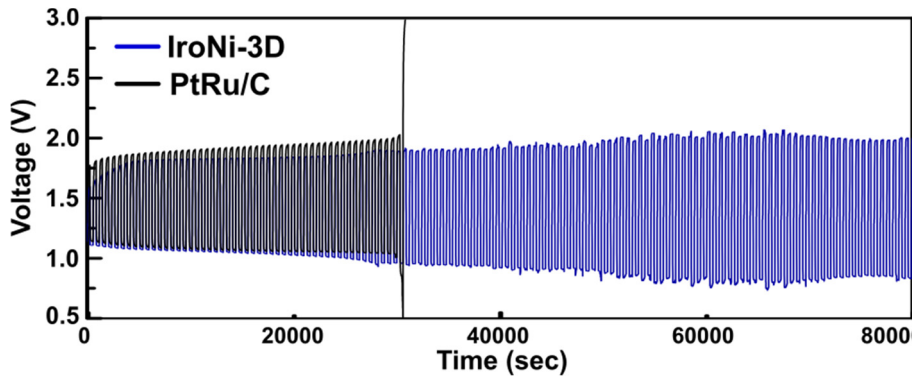

Figure 34. Galvanostatic charge-discharge cycling curves for IroNi-3D and benchmark Pt-RuO_2 performed at 5 mA cm^{-2}.

7.3.4 Bifunctionality comparison of TAMS-derived catalysts

During this PhD study, TAMS was developed and underwent gradual optimisations, addressing influencing factors of ORR and OER efficiency. Introduced upgrades and methodology enhancements continuously improved the bifunctionality of the derived M-N-C, leading to an outstanding ΔE value of 0.70 V (Fig. 35). Furthermore, TAMS-derived catalysts demonstrated potential applicability in ZAB, outperforming PGM-based catalysts. (Figs. 21 and 33) Overall, this study offers valuable insights into TAMS as a potential design strategy for efficient bifunctional M-N-C catalysts, laying the groundwork for further modifications and optimisation of the TAMS approach.

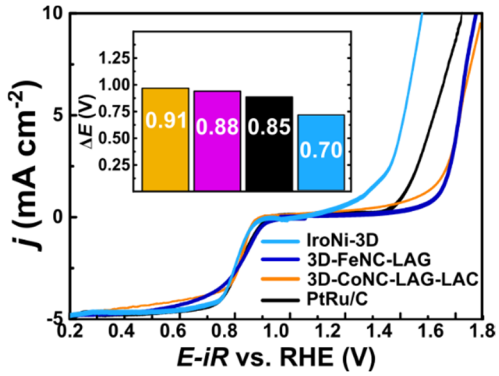

Figure 35. Bifunctionality comparison of best-performing TAMS-derived catalysts from each study.

7.4 Sustainability and cost-efficiency assessment

7.4.1 Preliminary sustainability assessment of TAMS method

In this work, the observed improvement in bifunctionality is the primary marker of TAMS efficiency. Beyond that, the sustainability and cost-efficiency of TAMS remain the main claims of the current study, which requires proof. Therefore, a comprehensive analysis was done to assess the method's sustainability, summarising the previously reported syntheses and the key aspects that determine their sustainability and cost-efficiency – Time and Energy (Table 14). The comparison was conducted on the protocol of the **3D-CoNC-LAG-LAC** and reported solvent-based syntheses of Co-N-C catalysts.

As a result, it was determined that TAMS, on average, requires 8 times less energy, and the reaction is 3 times quicker, yielding the same activity [103]. Moreover, in comparison to TAMS, the listed methods require solvent excess, sophisticated synthetic methods and materials. These findings, combined with minimal solvent usage and easy-to-conduct protocols, establish TAMS as a less time/energy-consuming method with no toxic waste and solvent overuse.

Table 14. Comparison of TAMS with recently reported procedures for Co-N-C synthesis.

Product	Energy consumed per synthesis (kJ)	Overall reaction time (h)
3D-CoNC-LAG-LAC	13158	6.5
Co-N-3DOM/mC [123]	164240	29
Co/MMCs [124]	59040	11
CoSAs@CNTs [125]	74160	16.5
$Co_2N_{0.67}$-BHPC [126]	163440	31
Co-N/PDC [127]	28000	6.5
UNT Co SAs/N-C [128]	168240	26

Nevertheless, the discovered superior sustainability of TAMS, shown by **3D-CoNC-LAG-LAC**, was anticipated, as the advantage of the solid-state approach over liquid-phase synthesis was well-proven by previous studies [130]. Therefore, to take the challenge one step further, the TAMS protocol for Fe-N-C catalysts was compared to the previously reported solid-phase syntheses of Fe-N-C catalysts. Thus, a preliminary assessment was performed for Fe-N-C TAMS, comparing the energy and time expenses of synthesis (Table 15). The comparison of results indicates that, on average, the best-performing **3D-FeNC-LAG** requires 5 times less energy input and features a 5 times quicker synthesis compared to other Fe-N-C mechanosynthesis protocols.

Table 15. Comparison of TAMS with recently reported procedures for Fe-N-C synthesis.

Product	Energy per synthesis (kWh)	Time per synthesis (h)	E_{on}
3D-FeNC-LAG	4.344	5.6	1.00
3D-FeNC-LAC	3.42	5.8	0.94
FFCN-MP4000 [131]	21.08	33.2	0.96
Fe-N-C from Fe-Pc [132]	34.82	56.3	0.98
Fe/N meso C-act [133]	16.8	11.0	0.99
FeDAAPyr [134]	21.1	22.5	0.95

Note that Tables 14 and 15 are a digest of a very detailed and thorough sustainability comparison. The information in the Tables summarises the key points of the study for readers' convenience. For detailed data, including reaction conditions, detailed synthesis process, equipment, material use, and values estimation, please see the referred works [103,116]. In the comparison, it was assumed that the same equipment was involved in every protocol for the simplicity of energy estimation. Furthermore, the duration of the synthesis was calculated using the reported procedures.

7.4.2 Multi-layer Stream Mapping for TAMS

While the preliminary assessment showed satisfactory results, highlighting the advantages of the TAMS protocol, the analysis was relatively primitive. Additionally, this method lacks sophisticated quantitative means of comparison often featured in more advanced sustainability assessment approaches [135]. Surprisingly, the search for advanced sustainability assessment methods for M-N-C catalyst synthesis yielded no results. Despite extensive research on M-N-C catalysts, there remains no established method to benchmark the sustainability merit of M-N-C synthesis for future studies. Thus, establishing such a method became one of the goals of this study. To make it viable, this method should feature adaptive, well-established assessment guidelines to serve as a universal tool for future research. To achieve this, the Multi-Layer Stream Mapping approach was

adapted to evaluate the efficiency of M-N-C catalyst synthesis, forming the basis for techno-economic and environmental upstream impact analysis [13]. The MSM methodology represents an industry-tested assessment method, serving as an enhancement of established Lean Methodologies [136]. At its core, MSM is a tool for assessing relative efficiency by determining deviations from the established benchmark – the best parameter in each corresponding category. The term category refers to Key Performance Indicators, which were determined prior to MSM analysis. In this work, KPIs were determined as follows: Process KPIs – Materials, consumed Time and Energy, and Performance KPI – E_{on}. Furthermore, the synthesis was divided into three related processes, namely Synthesis, Pyrolysis and Workup. Next, the KPI values were extracted from the reported procedures of Fe-N-C catalysts and compared with TAMS (Table 16).

Table 16. Summary of KPI values for Fe-N-C catalyst mechanosynthesis.

Catalyst	Synthesis		Pyrolysis		Workup		T_{tot} (h)	E_{tot} (kWh)	E_{onset}
	T (h)	E (kWh)	T (h)	E (kWh)	T (h)	E (kWh)			
FeNC-LAG	0.3	0.924	1.3	1.82	3	1.2	**4.6**	3.944	0.89
3D-FeNC-LAG	0.3	0.924	1.3	1.82	4	1.6	5.6	4.344	**1.00**
3D-FeNC-LAC	0.5	0	1.3	1.82	4	1.6	5.8	**3.42**	0.94
Fe_3C/FeNx-NOMC-2-900	-	0	10.5	14.7	-	-	10.5+	14.7+	0.85
HS-Phth-Fe-900	18.0+	7.2+	15.75	22.05	2	-	35.7+	29.25+	0.96
FFCN-MP4000	1.0	0	8.2	11.48	24	9.6	33.2	21.08	0.96
Fe-N-C Fe-Pc	44.0+	17.6	12.3	17.22	-	-	56.3	34.82	0.98
Fe_3C@3DCN – 1	1.5	4.2	11	15.4	-	-	12.5+	19.6	0.97
Fe/N meso C-act	-	0	12	16.8	-	-	11.0	16.8	0.99
FeDAAPyr	4.0	11.2	2.5	3.5	16	6.4	22.5	21.1	0.95

Upon summarising the KPIs, the Energy (E (kWh)) and Time (T (h)) were "normalised", meaning the lowest values in each category were benchmarked as 100%, and the remaining values were proportionally scaled relative to this benchmark. Next, the normalised values were plotted (Fig. 36a), indicating that TAMS exhibits over 80% relative time and energy efficiency. To provide a comprehensive outlook, Process KPIs (Energy and Time) were correlated with Performance KPI (E_{on}) (Fig. 36b). The results reveal that the TAMS protocol of **3D-FeNC-LAG** shows unmatched energy/time efficiency while retaining a high level of catalytic activity, significantly outperforming the next best alternative – Fe/N meso C-act [133].

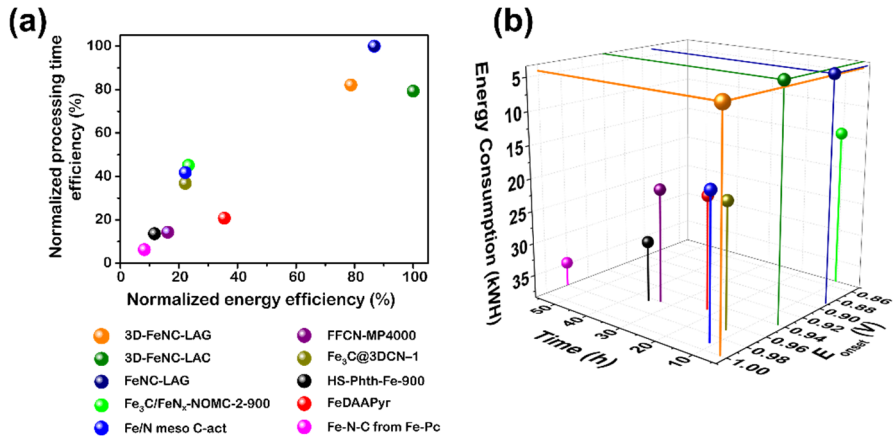

Figure 36. (a) Normalised Energy and Time consumption value comparison. (b) Correlation of Energy and Time efficiency with catalytic activity in absolute values.

Apart from KPI absolute values (in kWh, hour, etc.), MSM can also use the monetary units to perform a cost-efficiency assessment. For that, the cost of absolute values is used as an input, e.g. Energy in kWh = electricity price per kWh. Thus, KPI absolute values were converted to EUR (for cost estimation, see Section 7.5), and MSM was applied to map process deficiencies from the perspective of cost. For that, MSM analysis determines value-added costs (VA) – the "useful consumption" that adds value to the process, and non-value-added costs (NVA) – the "waste/misuses" of time, energy, or resources [13]. The KPIs of the Pyrolysis process were selected to assess the VA and NVA of solid-state protocols as the most representative process. After the analysis (Fig. 37), it was evident that the proposed rapid pyrolysis for TAMS showed 100% VA in comparison to the reported protocols, followed by pyrolysis of FeDAAPyr [134] (VA = 51%, NVA = 49%).

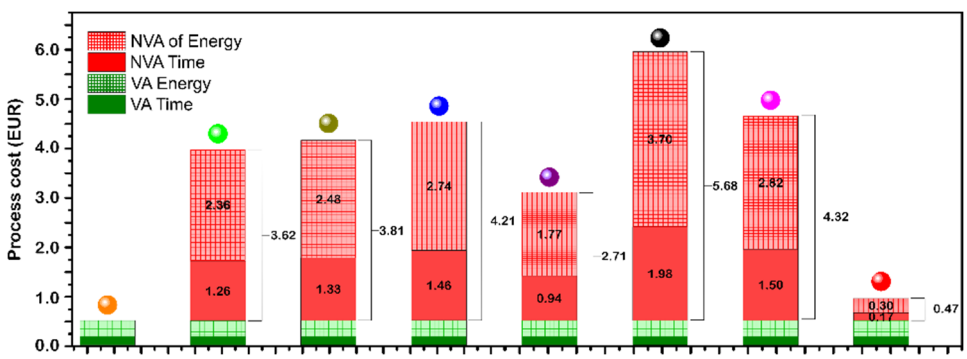

Figure 37. VA and NVA costs of pyrolysis comparison. (Materials are labelled in accordance with Figure 36).

From the cost perspective, the results of MSM suggest that TAMS-induced stability enabled rapid pyrolysis, yielding the lowest overall pyrolysis cost (0.50 EUR) compared to other reports. Next, MSM was applied to evaluate the cost efficiency of the TAMS-derived catalysts. For that, a detailed scorecard was assembled according to MSM guidelines [13,83]. The scorecard shows the efficiency of identified KPIs within TAMS catalysts. In the scorecard (Fig. 38), the TAMS for the **3D-FeNC-LAG** stands out with an outstanding overall efficiency of 90% while requiring no manual operation like with manual hydraulic press for **3D-FeNC-LAC**.

FeNC-LAG

	Process name	Synthesis	Pyrolysis	Workup	Overall efficiency
	Efficiency	64%	100%	88%	84%
KPI	Time (h)	100%	100%	100%	100%
KPI	Energy (kWh)	0%	100%	100%	78%

3D-FeNC-LAG

	Process name	Synthesis	Pyrolysis	Workup	Overall efficiency
	Efficiency	83%	100%	88%	90%
KPI	Time (h)	100%	100%	75%	82%
KPI	Energy (kWh)	0%	100%	75%	71%

3D-FeNC-LAC

	Process name	Synthesis	Pyrolysis	Workup	Overall efficiency
	Efficiency	93%	100%	88%	94%
KPI	Time (h)	60%	100%	75%	79%
KPI	Energy (kWh)	100%	100%	75%	88%

Figure 36. Scorecard of TAMS for FeNC-LAG, 3D-FeNC-LAG, and 3D-FeNC-LAC.

Next, the assembled scorecards allow for assessing the VA and NVA of the TAMS protocols. VA/NVA analysis (Fig. 39a,b) evidenced that TAMS-derived **3D-FeNC-LAC** and **3D-FeNC-LAG** result in the lowest overall NVA of 1.66 and 2.33%, respectively, yielding lower total price per 1g of catalyst (~12 EUR). The workup process constitutes most of the NVA (7.09% for both), stemming from additional time and energy to wash out the template. Overall, the MSM analysis results evidence that TAMS improved the resource, energy, and cost efficiency of the process. Combined with the improved bifunctionality, the TAMS approach emerges as an excellent method for M-N-C catalyst synthesis with outstanding sustainability metrics and cost efficiency, making TAMS a

sustainability benchmark in M-N-C catalyst synthesis, setting the standard for future developments in this field.

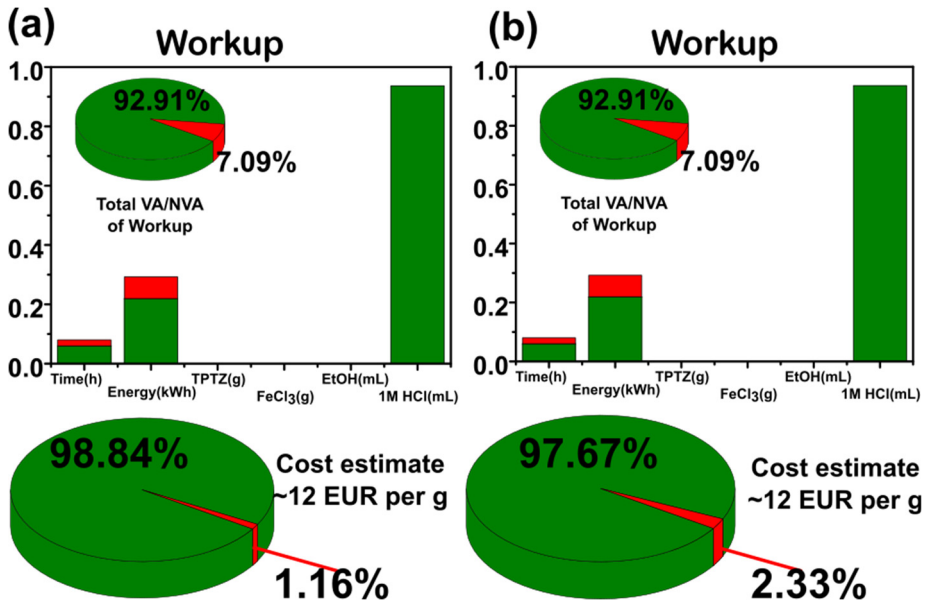

Figure 39. MSM cost assessment per Workup KPI (green – VA, red -NVA) and total cost for producing 1 g of the (a) 3D-FeNC-LAC and (b) 3D-FeNC-LAG.

8. SUMMARY

The current PhD study investigates the development of bifunctional transition metal-based catalysts using a novel synthesis method – Template-Assisted Mechanosynthesis (TAMS). The research focuses on optimising these catalysts for use in metal-air batteries (MABs), specifically zinc-air batteries (ZABs), which are promising for their high energy density and efficiency. However, ZABs face challenges such as low power density and limited stability due to the slow kinetics of the oxygen reduction reaction (ORR) and oxygen evolution reaction (OER). The core of the study is the synthesis and characterisation of cobalt (Co), iron (Fe) and nickel (Ni) based catalysts. The TAMS method was gradually enhanced with rapid pyrolysis, yielding a balance between ORR-active single-atom/nitrogen sites and OER-active nanoparticles. The upgraded TAMS protocol showed significant improvements in catalyst performance, including higher porosity and better electrochemical activity compared to traditional methods. Specifically, the 3D-FeNC-LAG catalyst demonstrated outstanding performance, with a power density of 139 mW cm^{-2} and stable long-term cycling in ZAB applications. Furthermore, the TAMS-derived catalysts exhibited improved bifunctional ORR/OER activity, which is essential for efficient ZAB operation. The IroNi-3D catalyst, in particular, showed the best ΔE of 0.70 V. Regarding morphology improvement, the catalysts produced via TAMS had superior porosity and surface area, with the TAMS-derived catalyst achieving a surface area of 450-600 $m^2\ g^{-1}$, enhancing the accessibility of active sites and overall catalytic efficiency. The electrochemical assessment of TAMS-derived catalysts confirmed their superior performance in ZABs, not only outperforming commercial PGM catalysts in terms of power density but also demonstrating exceptional stability over prolonged cycling periods. Furthermore, TAMS was found to be more sustainable and cost-effective compared to conventional liquid-phase synthesis methods, requiring significantly less energy and time, with no toxic waste generation. The 3D-FeNC-LAG synthesis, for instance, consumed five times less energy and was five times quicker than other reported methods. Overall, this study advances the field of electrochemical energy storage by providing a viable method to produce high-performance, sustainable catalysts for metal-air batteries. The findings contribute to the development of more efficient and cost-effective energy storage solutions, essential for integrating renewable energy sources into the power grid.

9. REFERENCES

1. H. Nazir, N. Muthuswamy, C. Louis, S. Jose, J. Prakash, M.E.M. Buan, C. Flox, S. Chavan, X. Shi, P. Kauranen, T. Kallio, G. Maia, K. Tammeveski, N. Lymperopoulos, E. Carcadea, E. Veziroglu, A. Iranzo, A. M. Kannan, *International Journal of Hydrogen Energy*, 45 (2020) 28217–28239.
2. I. Staffell, D. Scamman, A.V. Abad, P. Balcombe, P.E. Dodds, P. Ekins, N. Shah, K.R. Ward, *Energy Environ. Sci.*, 12 (2019) 463–491.
3. W.F. Pickard, A.Q. Shen, N.J. Hansing, *Renewable and Sustainable Energy Reviews*, 13 (2009) 1934–1945.
4. T. Li, M. Huang, X. Bai, Y.-X. Wang, *Progress in Natural Science: Materials International*, 33 (2023) 151–171.
5. M. Luo, W. Sun, B.B. Xu, H. Pan, Y. Jiang, *Advanced Energy Materials*, 11 (2021) 2002762.
6. X. Ren, Q. Lv, L. Liu, B. Liu, Y. Wang, A. Liu, G. Wu, *Sustainable Energy & Fuels*, 4 (2020) 15–30.
7. Q. Shi, C. Zhu, D. Du, Y. Lin, *Chemical Society Reviews*, 48 (2019) 3181–3192.
8. Y. Kumar, M. Mooste, K. Tammeveski, *Current Opinion in Electrochemistry*, 38 (2023) 101229.
9. H. Xu, D. Wang, P. Yang, L. Du, X. Lu, R. Li, L. Liu, J. Zhang, M. An, *Applied Catalysis B: Environmental*, 305 (2022) 121040.
10. L. Fan, H. Deng, Y. Zhang, Q. Du, D.Y.C. Leung, Y. Wang, K. Jiao, *Energy Environ. Sci.* (2023).
11. A.P. Amrute, J. De Bellis, M. Felderhoff, F. Schüth, *Chemistry – A European Journal*, 27 (2021) 6819–6847.
12. T.-P. Fellinger, A. Thomas, J. Yuan, M. Antonietti, *Adv. Mater.*, 25 (2013) 5838–5855.
13. P. Peças, B. Gonçalves, B. Rocha, D. Jorge, A. Baptista, M. Ram (Ed.), Advances in Mathematics for Industry 4.0, Academic Press, (2021), pp. 23–60.
14. M.A. Russo, D. Carvalho, N. Martins, A. Monteiro, *Sustainable Energy Technologies and Assessments*, 52 (2022) 102283.
15. R. Sharma, H. Kumar, G. Kumar, S. Sharma, R. Aneja, A.K. Sharma, R. Kumar, P. Kumar, *Chemical Engineering Journal*, 468 (2023) 143706.
16. Louis Maiche, US243454A, 1881.
17. J.-N. Liu, C.-X. Zhao, J. Wang, D. Ren, B.-Q. Li, Q. Zhang, *Energy Environ. Sci.*, 15 (2022) 4542–4553.
18. J. Pan, Y.Y. Xu, H. Yang, Z. Dong, H. Liu, B.Y. Xia, *Advanced Science*, 5 (2018) 1700691.
19. D. Linden, *Fuel and Energy Abstracts*, 4 (1995) 265.
20. L. Wei, E.H. Ang, Y. Yang, Y. Qin, Y. Zhang, M. Ye, Q. Liu, C.C. Li, *Journal of Power Sources*, 477 (2020) 228696.
21. T. Noor, L. Yaqoob, N. Iqbal, *ChemElectroChem*, 8 (2021) 447–483.
22. K.W. Leong, Y. Wang, M. Ni, W. Pan, S. Luo, D.Y.C. Leung, *Renewable and Sustainable Energy Reviews*, 154 (2022) 111771.
23. W. Shao, R. Yan, M. Zhou, L. Ma, C. Roth, T. Ma, S. Cao, C. Cheng, B. Yin, S. Li, *Electrochem. Energy Rev.*, 6 (2023) 11.
24. C. Li, E. Zhou, Z. Yu, H. Liu, M. Xiong, *Applied Catalysis B: Environmental*, 269 (2020) 118771.

25. X. Ge, A. Sumboja, D. Wuu, T. An, B. Li, F.W.T. Goh, T.S.A. Hor, Y. Zong, Z. Liu, *ACS Catal.*, 5 (2015) 4643–4667.
26. Q. Liang, G. Brocks, A. Bieberle-Hütter, *J. Phys. Energy*, 3 (2021) 026001.
27. Y. Wang, X. Zheng, D. Wang, *Nano Res.*, 15 (2022) 1730–1752.
28. K. Zeng, X. Zheng, C. Li, J. Yan, J.-H. Tian, C. Jin, P. Strasser, R. Yang, *Advanced Functional Materials*, 30 (2020) 2000503.
29. C.-X. Zhao, B.-Q. Li, J.-N. Liu, Q. Zhang, *Angewandte Chemie International Edition*, 60 (2021) 4448–4463.
30. W.-C. Chen, G. Yang, Y. Zhao, G.-Q. Yuan, J.-S. Ye, H.-Y. Liu, X.-Y. Xiao, *International Journal of Hydrogen Energy*, 46 (2021) 39882–39891.
31. J. Woo, H. Choi, Y.J. Sa, H.Y. Kim, T. Lim, J.-H. Jang, S.J. Yoo, J.Y. Kim, C.S. Kim, S.H. Joo, *J. Phys. Chem. C*, 125 (2021) 11928–11938.
32. Z. Shi, W. Yang, Y. Gu, T. Liao, Z. Sun, *Adv. Sci.*, 7 (2020) 2001069.
33. S. Kattel, P. Atanassov, B. Kiefer, *Phys. Chem. Chem. Phys.*, 15 (2012) 148–153.
34. C. Zúñiga, C. Candia-Onfray, R. Venegas, K. Muñoz, J. Urra, M. Sánchez-Arenillas, J.F. Marco, J.H. Zagal, F.J. Recio, *Electrochemistry Communications*, 102 (2019) 78–82.
35. X. Ning, Y. Li, J. Ming, Q. Wang, H. Wang, Y. Cao, F. Peng, Y. Yang, H. Yu, *Chem. Sci.*, 10 (2019) 1589–1596.
36. M. Skorupska, A. Ilnicka, J.P. Lukaszewicz, *Sci Rep*, 11 (2021) 23970.
37. M. Zerner, M. Gouterman, *Theoret. Chim. Acta*, 4 (1966) 44–63.
38. L. Osmieri, A.H.A. Monteverde Videla, P. Ocón, S. Specchia, *J. Phys. Chem. C*, 121 (2017) 17796–17817.
39. M. Zhou, Z. Zhu, Y. Ju, Y. Zhai, L. Jiao, M. Liu, W. Yang, J. Tang, *Electroanalysis*, 34 (2022) 1572–1578.
40. S. Xia, H. Yang, W. Lu, N. Cai, H. Xiao, X. Chen, Y. Chen, X. Wang, S. Wang, P. Wu, H. Chen, *Energy*, 239 (2022) 122262.
41. M. Tahir, L. Pan, F. Idrees, X. Zhang, L. Wang, J.-J. Zou, Z.L. Wang, *Nano Energy*, 37 (2017) 136–157.
42. J. Yang, J.K. Cooper, F.M. Toma, K.A. Walczak, M. Favaro, J.W. Beeman, L.H. Hess, C. Wang, C. Zhu, S. Gul, J. Yano, C. Kisielowski, A. Schwartzberg, I.D. Sharp, *Nature Mater*, 16 (2017) 335–341.
43. S. Niu, W.-J. Jiang, Z. Wei, T. Tang, J. Ma, J.-S. Hu, L.-J. Wan, *J. Am. Chem. Soc.*, 141 (2019) 7005–7013.
44. E. Cossar, F. Murphy, E.A. Baranova, *Journal of Chemical Technology & Biotechnology*, 97 (2022) 1611–1624.
45. L. Kuai, J. Geng, C. Chen, E. Kan, Y. Liu, Q. Wang, B. Geng, *Angewandte Chemie International Edition*, 53 (2014) 7547–7551.
46. D. Zhang, L. Meng, J. Shi, N. Wang, S. Liu, C. Li, *Electrochimica Acta*, 169 (2015) 402–408.
47. E. Cossar, K. Agarwal, V.B. Nguyen, R. Safari, G.A. Botton, E.A. Baranova, *Electrocatalysis*, 12 (2021) 605–618.
48. D. Chen, J. Zhu, X. Mu, R. Cheng, W. Li, S. Liu, Z. Pu, C. Lin, S. Mu, *Applied Catalysis B: Environmental*, 268 (2020) 118729.
49. K. Chen, S. Kim, R. Rajendiran, K. Prabakar, G. Li, Z. Shi, C. Jeong, J. Kang, O.L. Li, *Journal of Colloid and Interface Science*, 582 (2021) 977–990.
50. C. Du, Y. Gao, J. Wang, W. Chen, *J. Mater. Chem. A*, 8 (2020) 9981–9990.

51. M. Alam, K. Ping, M. Danilson, V. Mikli, M. Käärik, J. Leis, J. Aruväli, P. Paiste, M. Rähn, V. Sammelselg, K. Tammeveski, S. Haller, U.I. Kramm, P. Starkov, N. Kongi, *ACS Appl. Energy Mater.*, 7 (2024) 4076–4087.
52. A. Fauzi, X. Chen, H. Zhao, S. Cao, L. Kong, S. Huang, S. Zhang, X. Ma, *Next Energy*, 1 (2023) 100045.
53. S. Juvanen, A. Sarapuu, S. Vlassov, M. Kook, V. Kisand, M. Käärik, A. Treshchalov, J. Aruväli, J. Kozlova, A. Tamm, J. Leis, K. Tammeveski, *ChemElectroChem*, 8 (2021) 2288–2297.
54. K. Kisand, A. Sarapuu, J.C. Douglin, A. Kikas, A. Treshchalov, M. Käärik, H.-M. Piirsoo, P. Paiste, J. Aruväli, J. Leis, V. Kisand, A. Tamm, D.R. Dekel, K. Tammeveski, *ACS Catal.*, 12 (2022) 14050–14061.
55. J. Lilloja, M. Mooste, E. Kibena-Põldsepp, A. Sarapuu, A. Kikas, V. Kisand, M. Käärik, J. Kozlova, A. Treshchalov, P. Paiste, J. Aruväli, J. Leis, A. Tamm, S. Holdcroft, K. Tammeveski, *Electrochimica Acta*, 439 (2023) 141676.
56. J. Lilloja, E. Kibena-Põldsepp, A. Sarapuu, A. Konovalova, M. Käärik, J. Kozlova, P. Paiste, A. Kikas, A. Treshchalov, J. Aruväli, A. Zitolo, J. Leis, A. Tamm, V. Kisand, S. Holdcroft, K. Tammeveski, *ACS Appl. Energy Mater.*, 6 (2023) 5519–5529.
57. S.G. Peera, C. Liu, *Coordination Chemistry Reviews*, 463 (2022) 214554.
58. J. Fan, Z. Yang, S. Dai, *Green Chemical Engineering*, 5 (2024) 155–172.
59. F. Gomollón-Bel, *Chemistry International*, 41 (2019) 12–17.
60. A.I. Martín-Perales, A.M. Balu, I. Malpartida, R. Luque, *Current Opinion in Green and Sustainable Chemistry*, 38 (2022) 100714.
61. S.L. James, C.J. Adams, C. Bolm, D. Braga, P. Collier, T. Friščić, F. Grepioni, K.D.M. Harris, G. Hyett, W. Jones, A. Krebs, J. Mack, L. Maini, A.G. Orpen, I.P. Parkin, W.C. Shearouse, J.W. Steed, D.C. Waddell, *Chem. Soc. Rev.*, 41 (2012) 413–447.
62. T. Friščić, C. Mottillo, H.M. Titi, *Angewandte Chemie International Edition*, 59 (2020) 1018–1029.
63. X. Liu, W. Kang, X. Li, L. Zeng, Y. Li, Q. Wang, C. Zhang, *Nano Materials Science*, 5 (2023) 210–227.
64. O. Bento, F. Luttringer, T. Mohy El Dine, N. Pétry, X. Bantreil, F. Lamaty, *European Journal of Organic Chemistry*, 2022 (2022) e202101516.
65. K.J. Ardila-Fierro, J.G. Hernández, *ChemSusChem*, 14 (2021) 2145–2162.
66. D. Tan, T. Friščić, *European Journal of Organic Chemistry*, 2018 (2018) 18–33.
67. T. Friščić, L. Fábián, *CrystEngComm*, 11 (2009) 743.
68. G.-L. Wen, H.-J. Niu, A.-J. Wang, Z.-Z. Yin, Q.-L. Zhang, J.-J. Feng, *Journal of Colloid and Interface Science*, 556 (2019) 352–359.
69. Q. Sun, Z. Dai, X. Meng, F.-S. Xiao, *Chemical Society Reviews*, 44 (2015) 6018–6034.
70. X. S. Zhao, F. Su, Q. Yan, W. Guo, X. Ying Bao, L. Lv, Z. Zhou, *Journal of Materials Chemistry*, 16 (2006) 637–648.
71. L. Alison, S. Menasce, F. Bouville, E. Tervoort, I. Mattich, A. Ofner, A.R. Studart, *Sci Rep*, 9 (2019) 409.
72. R. Wang, H. Yang, N. Lu, S. Lei, D. Jia, Z. Wang, Z. Liu, X. Wu, H. Zheng, S. Ali, F. Ma, S. Peng, *Chemical Engineering Journal*, 433 (2022) 134500.
73. H. Adabi, A. Shakouri, N. Ul Hassan, J.R. Varcoe, B. Zulevi, A. Serov, J.R. Regalbuto, W.E. Mustain, *Nat Energy*, 6 (2021) 834–843.

74. J. Hu, D. Wu, C. Zhu, C. Hao, C. Xin, J. Zhang, J. Guo, N. Li, G. Zhang, Y. Shi, *Nano Energy*, 72 (2020) 104670.
75. N. Hedayat, Y. Du, H. Ilkhani, *Renewable and Sustainable Energy Reviews*, 77 (2017) 1221–1239.
76. H. Shin, J. Ko, C. Park, D.-H. Kim, J. Ahn, J.-S. Jang, Y.H. Kim, S.-H. Cho, H. Baik, I.-D. Kim, *Advanced Functional Materials*, 32 (2022) 2110485.
77. Y. Xie, D. Kocaefe, C. Chen, Y. Kocaefe, *Journal of Nanomaterials*, 2016 (2016) 2302595.
78. P. Saxena, P. Stavropoulos, J. Kechagias, K. Salonitis, *Energies*, 13 (2020) 2730.
79. S. Ahmad, K.Y. Wong, *Benchmarking: An International Journal*, 25 (2018) 3162–3179.
80. M. Schulz, M.D. Short, G.M. Peters, *Integrated Environmental Assessment and Management*, 8 (2012) 183–193.
81. J. Walzberg, G. Lonca, R.J. Hanes, A.L. Eberle, A. Carpenter, G.A. Heath, *Front. Sustain.*, 1 (2021).
82. L. Usai, C.R. Hung, F. Vásquez, M. Windsheimer, O.S. Burheim, A.H. Strømman, *Journal of Cleaner Production*, 280 (2021) 125086.
83. E.J. Lourenço, A.J. Baptista, J.P. Pereira, C. Dias-Ferreira, A.Y.C. Nee, B. Song, S.-K. Ong (Eds.), Re-Engineering Manufacturing for Sustainability, Springer, (2013) Singapore, pp. 427–433.
84. M.N. Gomes, A.J. Baptista, A.P. Guedes, I. Ribeiro, E.J. Lourenço, P. Peças, G. Campana, R.J. Howlett, R. Setchi, B. Cimatti (Eds.), Sustainable Design and Manufacturing 2017, Springer International Publishing, (2017) Cham, pp. 193–202.
85. A.J. Baptista, E.J. Lourenço, P. Peças, E.J. Silva, M.A. Estrela, M. Holgado, M. Benedetti, S. Evans, WASTES – Solutions, Treatments and Opportunities II, CRC Press, (2017).
86. S. Trasatti, O.A. Petrii, *Pure and Applied Chemistry*, 63 (1991) 711–734.
87. C.C.L. McCrory, S. Jung, J.C. Peters, T.F. Jaramillo, *J. Am. Chem. Soc.*, 135 (2013) 16977–16987.
88. A.J. Bard, L.R. Faulkner, Electrochemical Methods: Fundamentals and Applications, 2nd ed, Wiley, (2001) New York.
89. E.R. Cohen, B.N. Taylor, *Rev. Mod. Phys.*, 59 (1987) 1121–1148.
90. J. Wu, Z. Meng, R. Zhang, T. Tian, R. Wang, H. Tang, *Energy Fuels*, 36 (2022) 4006–4014.
91. C. Guo, R. Zhou, Z. Li, Y. Si, W. Liao, W. Sun, S. Xiang, X. Luo, M. Luo, Z. Luo, *Microporous and Mesoporous Materials*, 303 (2020) 110281.
92. C. Guo, Y. Li, W. Liao, Y. Liu, Z. Li, L. Sun, C. Chen, J. Zhang, Y. Si, L. Li, *J. Mater. Chem. A*, 6 (2018) 13050–13061.
93. S. Li, L. Zhang, H. Liu, M. Pan, L. Zan, J. Zhang, *Electrochimica Acta*, 55 (2010) 4403–4411.
94. S. Ortaboy, G. Atun, *Materials Chemistry and Physics*, 156 (2015) 129–140.
95. J. Yang, X. Feng, G. Lu, Y. Li, C. Mao, Z. Wen, W. Yuan, *Dalton Trans.*, 47 (2018) 5065–5071.
96. D. Weingarth, M. Zeiger, N. Jäckel, M. Aslan, G. Feng, V. Presser, *Advanced Energy Materials*, 4 (2014) 1400316.
97. R.K. Dash, G. Yushin, Y. Gogotsi, *Microporous and Mesoporous Materials*, 86 (2005) 50–57.

98. X.-Z. Fan, X. Du, Q.-Q. Pang, S. Zhang, Z.-Y. Liu, X.-Z. Yue, *ACS Appl. Mater. Interfaces*, 14 (2022) 8549–8556.
99. Y. Duan, T. Song, X. Dong, Y. Yang, *Green Chem.*, 20 (2018) 2821–2828.
100. I.S. Amiinu, X. Liu, Z. Pu, W. Li, Q. Li, J. Zhang, H. Tang, H. Zhang, S. Mu, *Adv. Funct. Mater.*, 28 (2018) 1704638.
101. F. Roncaroli, E.S. Dal Molin, F.A. Viva, M.M. Bruno, E.B. Halac, *Electrochimica Acta*, 174 (2015) 66–77.
102. L. Osmieri, A.H.A. Monteverde Videla, S. Specchia, *Journal of Power Sources*, 278 (2015) 296–307.
103. A. Kosimov, G. Yusibova, J. Aruväli, P. Paiste, M. Käärik, J. Leis, A. Kikas, V. Kisand, K. Šmits, N. Kongi, *Green Chem.*, 24 (2022) 305–314.
104. A.H. Tkaczyk, A. Bartl, A. Amato, V. Lapkovskis, M. Petranikova, *J. Phys. D: Appl. Phys.*, 51 (2018) 203001.
105. S.D. Bhoyate, J. Kim, F.M. de Souza, J. Lin, E. Lee, A. Kumar, R.K. Gupta, *Coordination Chemistry Reviews*, 474 (2023) 214854.
106. C.S.C. Kumar, L.Y. Then, T.S. Chia, S. Chandraju, Y.-F. Win, S.F. Sulaiman, N.S. Hashim, K.L. Ooi, C.K. Quah, H.-K. Fun, *Molecules*, 20 (2015) 16566–16581.
107. D. Menga, F. Ruiz-Zepeda, L. Moriau, M. Šala, F. Wagner, B. Koyutürk, M. Bele, U. Petek, N. Hodnik, M. Gaberšček, T. Fellinger, *Adv. Energy Mater.*, 9 (2019) 1902412.
108. X. Zhao, P. Pachfule, S. Li, J.R.J. Simke, J. Schmidt, A. Thomas, *Angewandte Chemie International Edition*, 57 (2018) 8921–8926.
109. D. Lyu, Y.B. Mollamahale, S. Huang, P. Zhu, X. Zhang, Y. Du, S. Wang, M. Qing, Z.Q. Tian, P.K. Shen, *Journal of Catalysis*, 368 (2018) 279–290.
110. T. Xiao, Y. Wang, J. Wan, Y. Ma, Z. Yan, S. Huang, C. Zeng, *Journal of Hazardous Materials*, 424 (2022) 127380.
111. Y. Xu, B. Chen, J. Nie, G. Ma, *Nanoscale*, 10 (2018) 17021–17029.
112. J. Zhang, J. Chen, Y. Luo, Y. Chen, Y. Luo, C. Zhang, Y. Xue, H. Liu, G. Wang, R. Wang, *J. Mater. Chem. A*, 9 (2021) 5556–5565.
113. H. Adabi, P.G. Santori, A. Shakouri, X. Peng, K. Yassin, I.G. Rasin, S. Brandon, D.R. Dekel, N.U. Hassan, M.-T. Sougrati, A. Zitolo, J.R. Varcoe, J.R. Regalbuto, F. Jaouen, W.E. Mustain, *Materials Today Advances*, 12 (2021) 100179.
114. Z. Chen, X. Gao, X. Wei, X. Wang, Y. Li, T. Wu, J. Guo, Q. Gu, W.D. Wu, X.D. Chen, Z. Wu, D. Zhao, *Carbon*, 121 (2017) 143–153.
115. K. Zhang, R. Zou, *Small*, n/a (n.d.) 2100129.
116. A. Kosimov, A. Alimbekova, J.-M. Assafrei, G. Yusibova, J. Aruväli, M. Käärik, J. Leis, P. Paiste, M. Ahmadi, K. Roohi, P. Taheri, S.M. Pinto, R. Cepitis, A.J. Baptista, P. Teppor, E. Lust, N. Kongi, *ACS Sustainable Chem. Eng.*, 11 (2023) 10825–10834.
117. C. Ouyang, L. Zheng, Q. Zhang, X. Wang, *Advanced Materials*, 34 (2022) 2205372.
118. N. Fechler, T.-P. Fellinger, M. Antonietti, *Adv. Mater.*, 25 (2013) 75–79.
119. J. Pampel, T.-P. Fellinger, *Advanced Energy Materials*, 6 (2016) 1502389.
120. A. Mehmood, J. Pampel, G. Ali, H.Y. Ha, F. Ruiz-Zepeda, T.-P. Fellinger, *Advanced Energy Materials*, 8 (2018) 1701771.
121. F. Wang, X. Li, X. Qi, C. Liu, T. Liang, *J. Electrochem. Soc.*, 167 (2020) 136512.
122. A. Kosimov, G. Yusibova, I.T. Wojsiat, J. Aruväli, M. Käärik, J. Leis, P. Paaver, S. Vlassov, A. Kikas, V. Kisand, H.-M. Piirsoo, K. Kukli, I. Heinmaa, T. Kaljuvee, N. Kongi, *J. Mater. Chem. A*, 12 (2023) 335–342.

123. Z. Meng, N. Chen, S. Cai, R. Wang, W. Guo, H. Tang, *International Journal of Energy Research*, 45 (2021) 6250–6261.
124. N. Huang, L. Yang, M. Zhang, S. Yan, Y. Ding, P. Sun, X. Sun, *ChemElectro Chem*, 6 (2019) 4522–4532.
125. S. Dilpazir, H. He, Z. Li, M. Wang, P. Lu, R. Liu, Z. Xie, D. Gao, G. Zhang, *ACS Appl. Energy Mater.*, 1 (2018) 3283–3291.
126. X. Lv, Z. Xiao, H. Wang, X. Wang, L. Shan, F. Wang, C. Wei, X. Tang, Y. Chen, *Journal of Energy Chemistry*, 54 (2021) 626–638.
127. K. Ping, M. Alam, S.R. Kahnert, R. Bhadoria, A. Mere, V. Mikli, M. Käärik, J. Aruväli, P. Paiste, A. Kikas, V. Kisand, I. Järving, J. Leis, N. Kongi, P. Starkov, *Mater. Adv.*, 2 (2021) 4009–4015.
128. X. Sun, S. Sun, S. Gu, Z. Liang, J. Zhang, Y. Yang, Z. Deng, P. Wei, J. Peng, Y. Xu, C. Fang, Q. Li, J. Han, Z. Jiang, Y. Huang, *Nano Energy*, 61 (2019) 245–250.
129. F. Afshariazar, A. Morsali, *J. Mater. Chem. A*, 10 (2022) 15332–15369.
130. T. Friščić, C. Mottillo, H.M. Titi, *Angewandte Chemie*, 132 (2020) 1030–1041.
131. M. Wu, J. Xie, A. Liu, W. Jia, Y. Cao, *Journal of Colloid and Interface Science*, 566 (2020) 194–201.
132. L. Osmieri, A.H.A. Monteverde Videla, M. Armandi, S. Specchia, *International Journal of Hydrogen Energy*, 41 (2016) 22570–22588.
133. Y. Toyama, K. Miyake, Y. Shu, K. Moroto, J. Ma, T. Zheng, S. Tanaka, N. Nishiyama, C. Fukuhara, C.Y. Kong, *Materials Today Energy*, 17 (2020) 100444.
134. A. Serov, K. Artyushkova, N.I. Andersen, S. Stariha, P. Atanassov, *Electrochimica Acta*, 179 (2015) 154–160.
135. D.P. Debecker, K. Kuok (Mimi) Hii, A. Moores, L.M. Rossi, B. Sels, D.T. Allen, B. Subramaniam, *ACS Sustainable Chem. Eng.*, 9 (2021) 4936–4940.
136. E.J. Lourenço, J.P. Pereira, R. Barbosa, A.J. Baptista, *Procedia CIRP*, 48 (2016) 128–133.

10. SUMMARY IN ESTONIAN

Malli abil mehhanokeemilise sünteesi meetod (TAMS) bifunktsionaalsete siirdemetallikatalüsaatorite tootmiseks

Doktoritöö eesmärk on arendada bifunktsionaalsete siirdemetallipõhiste katalüsaatorite väljatöötamist, kasutades uudset sünteesimeetodit – malliabiga mehhanosünteesi (TAMS). Doktoritöö keskendub bifunktsionaalsete katalüsaatorite optimeerimisele, et kasutada neid metall-õhkpatareides (MAB), eriti tsink-õhkpatareides (ZAB), mis on paljutõotavad oma suure energiatiheduse ja tõhususe poolest. Siiski seisavad ZAB-d silmitsi väljakutsetega, nagu madal võimsustihedus ja piiratud stabiilsus hapniku redutseerimisreaktsiooni (ORR) ja hapniku eraldumise reaktsiooni (OER) aeglase kineetika tõttu. Uuringu keskmes on koobalti (Co), raua (Fe) ja nikli (Ni) baasil katalüsaatorite süntees ja iseloomustamine. TAMS-meetodit täiustati järk-järgult kiire pürolüüsiga, saavutades tasakaalu ORR-aktiivsete üheaatomi/lämmastiku tsentrite ja OER-aktiivsete nanoosakeste vahel. Täiendatud TAMS-protokoll näitas katalüsaatori jõudluse märkimisväärset paranemist, sealhulgas suuremat poorsust ja paremat elektrokeemilist aktiivsust. Bifunktsionaalne 3D-FeNC-LAG katalüsaator demonstreeris silmapaistvat jõudlust, saavutades võimsustiheduse 139 mW cm^{-2} ja stabiilse pikaajalise tsükli ZAB-rakendustes. Lisaks näitasid TAMS-meetodil valmistatud katalüsaatorid paremat bifunktsionaalset ORR/OER aktiivsust, mis on ZAB tõhusaks tööks hädavajalik. Eelkõige näitas IroNi-3D katalüsaator parimat ΔE = 0,70 V väärtust. TAMS-i sünteesiprotsess parandas ka katalüsaatormaterjalide morfoloogiat. Katalüsaatori eripind oli 450-600 m^2 g^{-1}, mis parandas aktiivsete tsentrite ligipääsetavust ja üldist katalüütilist tõhusust. TAMS-ist tuletatud katalüsaatorite elektrokeemiline analüüs kinnitas nende paremat jõudlust ZAB-des, ületades mitte ainult kommertsiaalseid PGM-katalüsaatoreid võimsustiheduse osas, vaid demonstreerides ka erakordset stabiilsust pikemate tsükliperioodide jooksul. Lisaks leiti, et TAMS on tavapäraste vedelfaasi sünteesimeetoditega võrreldes säästvam ja kulutõhusam, nõudes oluliselt vähem energiat ja aega ning vältides mürgiste jäätmete teket. Näiteks 3D-FeNC-LAG süntees tarbis viis korda vähem energiat ja oli viis korda kiirem kui teised teatatud meetodid. Üldiselt edendab see uuring elektrokeemilise energia salvestamise valdkonda, pakkudes elujõulist meetodit suure jõudlusega ja jätkusuutlike katalüsaatorite tootmiseks metall-õhk akude jaoks. Tulemused aitavad kaasa tõhusamate ja kuluefektiivsemate energiasalvestuslahenduste väljatöötamisele, mis on hädavajalikud taastuvate energiaallikate elektrivõrku integreerimiseks.

11. ACKNOWLEDGEMENTS

First and foremost, I would like to express my deepest gratitude to my supervisor, Assoc. Prof. Nadežda Kongi, for her support, guidance, and encouragement throughout this journey. Your expertise and insights have been invaluable to the development of this thesis. I am also profoundly grateful to Assoc. Prof. Vladislav Ivaništšev for his constant support and constructive feedback. I am thankful to my colleagues and friends at UT, who have provided a stimulating and enjoyable environment. Special thanks to Ritums Cepitis for the friendship, support and countless discussions that enriched my research perspective. I extend my heartfelt thanks to my family for their unconditional love, patience, and support. To my mother for believing in me and encouraging me to pursue my dreams, and to my sister for always being there to lift my spirits.

Furthermore, I would like to express my sincere gratitude to my colleagues and collaborators for contributing to the development of the TAMS methodology. More specifically, I am grateful to the University of Tartu collaborators for conducting PXRD (Jaan Aruväli), MP-AES (Päärn Paiste, Peeter Paaver), electron microscopy (Sergei Vlassov), N_2 physisorption (Maike Käärik, Jaan Leis) and XPS (Arvo Kikas, Vambola Kisand) measurements. Moreover, I would like to thank external collaborators for performing XPS (Khatereh Roohi, Peyman Taheri – Delft University of Technology), electron microscopy (Krišjānis Šmits – University of Latvia, Majid Ahmadi – University of Groningen), MSM sustainability assessment (Sara M. Pinto, Antonio J. Baptista – INEGI), s-NMR (Ivo Heinmaa – KBFI), and TGA (Tiit Kaljuvee – Tallinn Technical University) measurements. Additionally, I am thankful for the help of my colleagues and students at KongiLab Gulnara Yusibova, Amina Alimbekova, Jurgen-Martin Assafrei, and Ivan Tito Wojsiat for conducting electrochemical measurements and ZAB testing of the TAMS-derived catalysts.

My research work was financially supported by the Estonian Research Council (grant PSG250).

PUBLICATIONS

CURRICULUM VITAE

Name: Akmal Kosimov
Date of birth: Sep 30, 1995
Citizenship: Uzbekistan
Address: Ravila 14a, 50411 Tartu, Estonia
E-mail: akmal.kosimov99@gmail.com

Education:

2020–…	University of Tartu, Faculty of Science and Technology, Estonia, *Ph.D. studies in Chemistry*
2018–2020	Adam Mickiewicz University in Poznan, Faculty of Chemistry, Poland, *M.Sc. in Chemistry*
2014–2018	Riga Technical University, Faculty of Chemistry, Latvia, *B.Sc. in Chemistry*

Professional experience:

2022–…	RedoxNRG OÜ, Tartu, Estonia, *Researcher*
06.2020–09.2020	Selvita SA pharma, Poznan, Poland, *Researcher*
07.2019–10. 2019	Comenius University, Natural Sciences Faculty, Slovakia, *Junior Researcher*
01.2017–07.2018	Latvian institute of organic synthesis, Latvia, *Junior Researcher*

Major scientific publications:

1. **Kosimov, A.**; Yusibova, G.; Aruväli, J.; Paiste, P.; Käärik, M.; Leis, J.; Kikas, A.; Kisand, V.; Šmits, K.; Kongi, N. Liquid-Assisted Grinding/Compression: A Facile Mechanosynthetic Route for the Production of High-Performing Co–N–C Electrocatalyst Materials. *Green Chemistry* 2022, 24 (1), 305–314. DOI: 10.1039/D1GC03433B
2. **Kosimov, A.**; Alimbekova, A.; Assafrei, J.-M.; Yusibova, G.; Aruväli, J.; Käärik, M.; Leis, J.; Paiste, P.; Ahmadi, M.; Roohi, K.; Taheri, P.; Pinto, S. M.; Cepitis, R.; Baptista, A. J.; Teppor, P.; Lust, E.; Kongi, N. Template-Assisted Mechanosynthesis Leading to Benchmark Energy Efficiency and Sustainability in the Production of Bifunctional Fe–N–C Electrocatalysts. *ACS Sustainable Chem. Eng.* 2023, 11 (29), 10825–10834. DOI: 10.1021/acssuschemeng.3c02077
3. Eaby, A. C.; Myburgh, D. C.; **Kosimov, A.**; Kwit, M.; Esterhuysen, C.; Janiak, A. M.; Barbour, L. J. Dehydration of a Crystal Hydrate at Subglacial Temperatures. *Nature* 2023, *616* (7956), 288–292. DOI: 10.1038/s41586-023-05749-7.
4. **Kosimov, A.**; Yusibova, G.; Wojsiat, I.T.; Aruväli, J.; Käärik, M.; Leis, J.; Paaver, P.; Vlassov, S.; Kikas, A.; Kisand, V.; Piirsoo, H.-M.; Kukli, K.; Heinmaa, I.; Kaljuvee, T.; Kongi, N. Mechanosynthesis of bifunctional

FeNi-NC oxygen electrocatalyst via a facile mixed-phase templating and preheating-pyrolysis. *Journal of Materials Chemistry A*, 2023, 12, 335-342. DOI: 10.1039/D3TA04580C

ELULOOKIRJELDUS

Nimi: Akmal Kosimov
Sünniaeg: September 30, 1995
Kodakondsus: Usbekistan
Address: Ravila 14a, 50411 Tartu, Estonia
E-mail: akmal.kosimov99@gmail.com

Hariduskäik:

2020–…	Tartu Ülikool, Loodus- ja täppisteaduste valdkond, Eesti, PhD
2018–2020	Adam Mickiewiczi Ülikool Poznanis, Keemiateaduskond, Poola, MSc
2014–2018	Riia Tehnikaülikool, Keemiateaduskond, Läti, BSc

Töökogemus:

2022–…	RedoxNRG OÜ, Tartu, Eesti, *Uurija*
2020–2020	Selvita SA pharma, Poznan, Poola, *Uurija*
2019–2019	Comenius University, Natural Sciences Faculty, Slovakkia, *Nooremteadur*
2017–2018	Latvian institute of organic synthesis, Läti, *Nooremteadur*

Publikatsioonide loetelu:

1. **Kosimov, A.**; Yusibova, G.; Aruväli, J.; Paiste, P.; Käärik, M.; Leis, J.; Kikas, A.; Kisand, V.; Šmits, K.; Kongi, N. Liquid-Assisted Grinding/Compression: A Facile Mechanosynthetic Route for the Production of High-Performing Co–N–C Electrocatalyst Materials. *Green Chemistry* 2022, 24 (1), 305–314. DOI: 10.1039/D1GC03433B
2. **Kosimov, A.**; Alimbekova, A.; Assafrei, J.-M.; Yusibova, G.; Aruväli, J.; Käärik, M.; Leis, J.; Paiste, P.; Ahmadi, M.; Roohi, K.; Taheri, P.; Pinto, S. M.; Cepitis, R.; Baptista, A. J.; Teppor, P.; Lust, E.; Kongi, N. Template-Assisted Mechanosynthesis Leading to Benchmark Energy Efficiency and Sustainability in the Production of Bifunctional Fe–N–C Electrocatalysts. *ACS Sustainable Chem. Eng.* 2023, 11 (29), 10825–10834. DOI: 10.1021/acssuschemeng.3c02077
3. Eaby, A. C.; Myburgh, D. C.; **Kosimov, A.**; Kwit, M.; Esterhuysen, C.; Janiak, A. M.; Barbour, L. J. Dehydration of a Crystal Hydrate at Subglacial Temperatures. *Nature* 2023, *616* (7956), 288–292. DOI: 10.1038/s41586-023-05749-7.
4. **Kosimov, A.**; Yusibova, G.; Wojsiat, I.T.; Aruväli, J.; Käärik, M.; Leis, J.; Paaver, P.; Vlassov, S.; Kikas, A.; Kisand, V.; Piirsoo, H.-M.; Kukli, K.; Heinmaa, I.; Kaljuvee, T.; Kongi, N. Mechanosynthesis of bifunctional FeNi-NC oxygen electrocatalyst via a facile mixed-phase templating and preheating-pyrolysis. *Journal of Materials Chemistry A*, 2023, 12, 335-342. DOI: 10.1039/D3TA04580C

DISSERTATIONES CHIMICAE UNIVERSITATIS TARTUENSIS

1. **Toomas Tamm.** Quantum-chemical simulation of solvent effects. Tartu, 1993, 110 p.
2. **Peeter Burk.** Theoretical study of gas-phase acid-base equilibria. Tartu, 1994, 96 p.
3. **Victor Lobanov.** Quantitative structure-property relationships in large descriptor spaces. Tartu, 1995, 135 p.
4. **Vahur Mäemets.** The ^{17}O and ^{1}H nuclear magnetic resonance study of H_2O in individual solvents and its charged clusters in aqueous solutions of electrolytes. Tartu, 1997, 140 p.
5. **Andrus Metsala.** Microcanonical rate constant in nonequilibrium distribution of vibrational energy and in restricted intramolecular vibrational energy redistribution on the basis of slater's theory of unimolecular reactions. Tartu, 1997, 150 p.
6. **Uko Maran.** Quantum-mechanical study of potential energy surfaces in different environments. Tartu, 1997, 137 p.
7. **Alar Jänes.** Adsorption of organic compounds on antimony, bismuth and cadmium electrodes. Tartu, 1998, 219 p.
8. **Kaido Tammeveski.** Oxygen electroreduction on thin platinum films and the electrochemical detection of superoxide anion. Tartu, 1998, 139 p.
9. **Ivo Leito.** Studies of Brønsted acid-base equilibria in water and non-aqueous media. Tartu, 1998, 101 p.
10. **Jaan Leis.** Conformational dynamics and equilibria in amides. Tartu, 1998, 131 p.
11. **Toonika Rinken.** The modelling of amperometric biosensors based on oxidoreductases. Tartu, 2000, 108 p.
12. **Dmitri Panov.** Partially solvated Grignard reagents. Tartu, 2000, 64 p.
13. **Kaja Orupõld.** Treatment and analysis of phenolic wastewater with microorganisms. Tartu, 2000, 123 p.
14. **Jüri Ivask.** Ion Chromatographic determination of major anions and cations in polar ice core. Tartu, 2000, 85 p.
15. **Lauri Vares.** Stereoselective Synthesis of Tetrahydrofuran and Tetrahydropyran Derivatives by Use of Asymmetric Horner-Wadsworth-Emmons and Ring Closure Reactions. Tartu, 2000, 184 p.
16. **Martin Lepiku.** Kinetic aspects of dopamine D_2 receptor interactions with specific ligands. Tartu, 2000, 81 p.
17. **Katrin Sak.** Some aspects of ligand specificity of P2Y receptors. Tartu, 2000, 106 p.
18. **Vello Pällin.** The role of solvation in the formation of iotsitch complexes. Tartu, 2001, 95 p.
19. **Katrin Kollist.** Interactions between polycyclic aromatic compounds and humic substances. Tartu, 2001, 93 p.

20. **Ivar Koppel.** Quantum chemical study of acidity of strong and superstrong Brønsted acids. Tartu, 2001, 104 p.
21. **Viljar Pihl.** The study of the substituent and solvent effects on the acidity of OH and CH acids. Tartu, 2001, 132 p.
22. **Natalia Palm.** Specification of the minimum, sufficient and significant set of descriptors for general description of solvent effects. Tartu, 2001, 134 p.
23. **Sulev Sild.** QSPR/QSAR approaches for complex molecular systems. Tartu, 2001, 134 p.
24. **Ruslan Petrukhin.** Industrial applications of the quantitative structure-property relationships. Tartu, 2001, 162 p.
25. **Boris V. Rogovoy.** Synthesis of (benzotriazolyl)carboximidamides and their application in relations with *N*- and *S*-nucleophyles. Tartu, 2002, 84 p.
26. **Koit Herodes.** Solvent effects on UV-vis absorption spectra of some solvatochromic substances in binary solvent mixtures: the preferential solvation model. Tartu, 2002, 102 p.
27. **Anti Perkson.** Synthesis and characterisation of nanostructured carbon. Tartu, 2002, 152 p.
28. **Ivari Kaljurand.** Self-consistent acidity scales of neutral and cationic Brønsted acids in acetonitrile and tetrahydrofuran. Tartu, 2003, 108 p.
29. **Karmen Lust.** Adsorption of anions on bismuth single crystal electrodes. Tartu, 2003, 128 p.
30. **Mare Piirsalu.** Substituent, temperature and solvent effects on the alkaline hydrolysis of substituted phenyl and alkyl esters of benzoic acid. Tartu, 2003, 156 p.
31. **Meeri Sassian.** Reactions of partially solvated Grignard reagents. Tartu, 2003, 78 p.
32. **Tarmo Tamm.** Quantum chemical modelling of polypyrrole. Tartu, 2003. 100 p.
33. **Erik Teinemaa.** The environmental fate of the particulate matter and organic pollutants from an oil shale power plant. Tartu, 2003. 102 p.
34. **Jaana Tammiku-Taul.** Quantum chemical study of the properties of Grignard reagents. Tartu, 2003. 120 p.
35. **Andre Lomaka.** Biomedical applications of predictive computational chemistry. Tartu, 2003. 132 p.
36. **Kostyantyn Kirichenko.** Benzotriazole – Mediated Carbon–Carbon Bond Formation. Tartu, 2003. 132 p.
37. **Gunnar Nurk.** Adsorption kinetics of some organic compounds on bismuth single crystal electrodes. Tartu, 2003, 170 p.
38. **Mati Arulepp.** Electrochemical characteristics of porous carbon materials and electrical double layer capacitors. Tartu, 2003, 196 p.
39. **Dan Cornel Fara.** QSPR modeling of complexation and distribution of organic compounds. Tartu, 2004, 126 p.
40. **Riina Mahlapuu.** Signalling of galanin and amyloid precursor protein through adenylate cyclase. Tartu, 2004, 124 p.

41. **Mihkel Kerikmäe.** Some luminescent materials for dosimetric applications and physical research. Tartu, 2004, 143 p.
42. **Jaanus Kruusma.** Determination of some important trace metal ions in human blood. Tartu, 2004, 115 p.
43. **Urmas Johanson.** Investigations of the electrochemical properties of polypyrrole modified electrodes. Tartu, 2004, 91 p.
44. **Kaido Sillar.** Computational study of the acid sites in zeolite ZSM-5. Tartu, 2004, 80 p.
45. **Aldo Oras.** Kinetic aspects of dATPαS interaction with $P2Y_1$ receptor. Tartu, 2004, 75 p.
46. **Erik Mölder.** Measurement of the oxygen mass transfer through the air-water interface. Tartu, 2005, 73 p.
47. **Thomas Thomberg.** The kinetics of electroreduction of peroxodisulfate anion on cadmium (0001) single crystal electrode. Tartu, 2005, 95 p.
48. **Olavi Loog.** Aspects of condensations of carbonyl compounds and their imine analogues. Tartu, 2005, 83 p.
49. **Siim Salmar.** Effect of ultrasound on ester hydrolysis in aqueous ethanol. Tartu, 2006, 73 p.
50. **Ain Uustare.** Modulation of signal transduction of heptahelical receptors by other receptors and G proteins. Tartu, 2006, 121 p.
51. **Sergei Yurchenko.** Determination of some carcinogenic contaminants in food. Tartu, 2006, 143 p.
52. **Kaido Tämm.** QSPR modeling of some properties of organic compounds. Tartu, 2006, 67 p.
53. **Olga Tšubrik.** New methods in the synthesis of multisubstituted hydrazines. Tartu. 2006, 183 p.
54. **Lilli Sooväli.** Spectrophotometric measurements and their uncertainty in chemical analysis and dissociation constant measurements. Tartu, 2006, 125 p.
55. **Eve Koort.** Uncertainty estimation of potentiometrically measured ph and pK_a values. Tartu, 2006, 139 p.
56. **Sergei Kopanchuk.** Regulation of ligand binding to melanocortin receptor subtypes. Tartu, 2006, 119 p.
57. **Silvar Kallip.** Surface structure of some bismuth and antimony single crystal electrodes. Tartu, 2006, 107 p.
58. **Kristjan Saal.** Surface silanization and its application in biomolecule coupling. Tartu, 2006, 77 p.
59. **Tanel Tätte.** High viscosity $Sn(OBu)_4$ oligomeric concentrates and their applications in technology. Tartu, 2006, 91 p.
60. **Dimitar Atanasov Dobchev**. Robust QSAR methods for the prediction of properties from molecular structure. Tartu, 2006, 118 p.
61. **Hannes Hagu**. Impact of ultrasound on hydrophobic interactions in solutions. Tartu, 2007, 81 p.
62. **Rutha Jäger.** Electroreduction of peroxodisulfate anion on bismuth electrodes. Tartu, 2007, 142 p.

63. **Kaido Viht.** Immobilizable bisubstrate-analogue inhibitors of basophilic protein kinases: development and application in biosensors. Tartu, 2007, 88 p.
64. **Eva-Ingrid Rõõm.** Acid-base equilibria in nonpolar media. Tartu, 2007, 156 p.
65. **Sven Tamp.** DFT study of the cesium cation containing complexes relevant to the cesium cation binding by the humic acids. Tartu, 2007, 102 p.
66. **Jaak Nerut.** Electroreduction of hexacyanoferrate(III) anion on Cadmium (0001) single crystal electrode. Tartu, 2007, 180 p.
67. **Lauri Jalukse.** Measurement uncertainty estimation in amperometric dissolved oxygen concentration measurement. Tartu, 2007, 112 p.
68. **Aime Lust.** Charge state of dopants and ordered clusters formation in CaF_2:Mn and CaF_2:Eu luminophors. Tartu, 2007, 100 p.
69. **Iiris Kahn**. Quantitative Structure-Activity Relationships of environmentally relevant properties. Tartu, 2007, 98 p.
70. **Mari Reinik.** Nitrates, nitrites, N-nitrosamines and polycyclic aromatic hydrocarbons in food: analytical methods, occurrence and dietary intake. Tartu, 2007, 172 p.
71. **Heili Kasuk.** Thermodynamic parameters and adsorption kinetics of organic compounds forming the compact adsorption layer at Bi single crystal electrodes. Tartu, 2007, 212 p.
72. **Erki Enkvist.** Synthesis of adenosine-peptide conjugates for biological applications. Tartu, 2007, 114 p.
73. **Svetoslav Hristov Slavov**. Biomedical applications of the QSAR approach. Tartu, 2007, 146 p.
74. **Eneli Härk.** Electroreduction of complex cations on electrochemically polished Bi(*hkl*) single crystal electrodes. Tartu, 2008, 158 p.
75. **Priit Möller.** Electrochemical characteristics of some cathodes for medium temperature solid oxide fuel cells, synthesized by solid state reaction technique. Tartu, 2008, 90 p.
76. **Signe Viggor.** Impact of biochemical parameters of genetically different pseudomonads at the degradation of phenolic compounds. Tartu, 2008, 122 p.
77. **Ave Sarapuu.** Electrochemical reduction of oxygen on quinone-modified carbon electrodes and on thin films of platinum and gold. Tartu, 2008, 134 p.
78. **Agnes Kütt.** Studies of acid-base equilibria in non-aqueous media. Tartu, 2008, 198 p.
79. **Rouvim Kadis.** Evaluation of measurement uncertainty in analytical chemistry: related concepts and some points of misinterpretation. Tartu, 2008, 118 p.
80. **Valter Reedo.** Elaboration of IVB group metal oxide structures and their possible applications. Tartu, 2008, 98 p.
81. **Aleksei Kuznetsov.** Allosteric effects in reactions catalyzed by the cAMP-dependent protein kinase catalytic subunit. Tartu, 2009, 133 p.

82. **Aleksei Bredihhin.** Use of mono- and polyanions in the synthesis of multisubstituted hydrazine derivatives. Tartu, 2009, 105 p.
83. **Anu Ploom.** Quantitative structure-reactivity analysis in organosilicon chemistry. Tartu, 2009, 99 p.
84. **Argo Vonk.** Determination of adenosine A_{2A}- and dopamine D_1 receptor-specific modulation of adenylate cyclase activity in rat striatum. Tartu, 2009, 129 p.
85. **Indrek Kivi.** Synthesis and electrochemical characterization of porous cathode materials for intermediate temperature solid oxide fuel cells. Tartu, 2009, 177 p.
86. **Jaanus Eskusson.** Synthesis and characterisation of diamond-like carbon thin films prepared by pulsed laser deposition method. Tartu, 2009, 117 p.
87. **Marko Lätt.** Carbide derived microporous carbon and electrical double layer capacitors. Tartu, 2009, 107 p.
88. **Vladimir Stepanov.** Slow conformational changes in dopamine transporter interaction with its ligands. Tartu, 2009, 103 p.
89. **Aleksander Trummal.** Computational Study of Structural and Solvent Effects on Acidities of Some Brønsted Acids. Tartu, 2009, 103 p.
90. **Eerold Vellemäe.** Applications of mischmetal in organic synthesis. Tartu, 2009, 93 p.
91. **Sven Parkel.** Ligand binding to 5-HT_{1A} receptors and its regulation by Mg^{2+} and Mn^{2+}. Tartu, 2010, 99 p.
92. **Signe Vahur.** Expanding the possibilities of ATR-FT-IR spectroscopy in determination of inorganic pigments. Tartu, 2010, 184 p.
93. **Tavo Romann**. Preparation and surface modification of bismuth thin film, porous, and microelectrodes. Tartu, 2010, 155 p.
94. **Nadežda Aleksejeva.** Electrocatalytic reduction of oxygen on carbon nanotube-based nanocomposite materials. Tartu, 2010, 147 p.
95. **Marko Kullapere.** Electrochemical properties of glassy carbon, nickel and gold electrodes modified with aryl groups. Tartu, 2010, 233 p.
96. **Liis Siinor.** Adsorption kinetics of ions at Bi single crystal planes from aqueous electrolyte solutions and room-temperature ionic liquids. Tartu, 2010, 101 p.
97. **Angela Vaasa.** Development of fluorescence-based kinetic and binding assays for characterization of protein kinases and their inhibitors. Tartu 2010, 101 p.
98. **Indrek Tulp.** Multivariate analysis of chemical and biological properties. Tartu 2010, 105 p.
99. **Aare Selberg.** Evaluation of environmental quality in Northern Estonia by the analysis of leachate. Tartu 2010, 117 p.
100. **Darja Lavõgina.** Development of protein kinase inhibitors based on adenosine analogue-oligoarginine conjugates. Tartu 2010, 248 p.
101. **Laura Herm.** Biochemistry of dopamine D_2 receptors and its association with motivated behaviour. Tartu 2010, 156 p.

102. **Terje Raudsepp.** Influence of dopant anions on the electrochemical properties of polypyrrole films. Tartu 2010, 112 p.
103. **Margus Marandi.** Electroformation of Polypyrrole Films: *In-situ* AFM and STM Study. Tartu 2011, 116 p.
104. **Kairi Kivirand.** Diamine oxidase-based biosensors: construction and working principles. Tartu, 2011, 140 p.
105. **Anneli Kruve.** Matrix effects in liquid-chromatography electrospray mass-spectrometry. Tartu, 2011, 156 p.
106. **Gary Urb.** Assessment of environmental impact of oil shale fly ash from PF and CFB combustion. Tartu, 2011, 108 p.
107. **Nikita Oskolkov.** A novel strategy for peptide-mediated cellular delivery and induction of endosomal escape. Tartu, 2011, 106 p.
108. **Dana Martin.** The QSPR/QSAR approach for the prediction of properties of fullerene derivatives. Tartu, 2011, 98 p.
109. **Säde Viirlaid.** Novel glutathione analogues and their antioxidant activity. Tartu, 2011, 106 p.
110. **Ülis Sõukand.** Simultaneous adsorption of Cd^{2+}, Ni^{2+}, and Pb^{2+} on peat. Tartu, 2011, 124 p.
111. **Lauri Lipping.** The acidity of strong and superstrong Brønsted acids, an outreach for the "limits of growth": a quantum chemical study. Tartu, 2011, 124 p.
112. **Heisi Kurig.** Electrical double-layer capacitors based on ionic liquids as electrolytes. Tartu, 2011, 146 p.
113. **Marje Kasari.** Bisubstrate luminescent probes, optical sensors and affinity adsorbents for measurement of active protein kinases in biological samples. Tartu, 2012, 126 p.
114. **Kalev Takkis.** Virtual screening of chemical databases for bioactive molecules. Tartu, 2012, 122 p.
115. **Ksenija Kisseljova**. Synthesis of aza-β^3-amino acid containing peptides and kinetic study of their phosphorylation by protein kinase A. Tartu, 2012, 104 p.
116. **Riin Rebane.** Advanced method development strategy for derivatization LC/ESI/MS. Tartu, 2012, 184 p.
117. **Vladislav Ivaništšev.** Double layer structure and adsorption kinetics of ions at metal electrodes in room temperature ionic liquids. Tartu, 2012, 128 p.
118. **Irja Helm.** High accuracy gravimetric Winkler method for determination of dissolved oxygen. Tartu, 2012, 139 p.
119. **Karin Kipper.** Fluoroalcohols as Components of LC-ESI-MS Eluents: Usage and Applications. Tartu, 2012, 164 p.
120. **Arno Ratas.** Energy storage and transfer in dosimetric luminescent materials. Tartu, 2012, 163 p.
121. **Reet Reinart-Okugbeni**. Assay systems for characterisation of subtype-selective binding and functional activity of ligands on dopamine receptors. Tartu, 2012, 159 p.

122. **Lauri Sikk.** Computational study of the Sonogashira cross-coupling reaction. Tartu, 2012, 81 p.
123. **Karita Raudkivi.** Neurochemical studies on inter-individual differences in affect-related behaviour of the laboratory rat. Tartu, 2012, 161 p.
124. **Indrek Saar.** Design of GalR2 subtype specific ligands: their role in depression-like behavior and feeding regulation. Tartu, 2013, 126 p.
125. **Ann Laheäär.** Electrochemical characterization of alkali metal salt based non-aqueous electrolytes for supercapacitors. Tartu, 2013, 127 p.
126. **Kerli Tõnurist.** Influence of electrospun separator materials properties on electrochemical performance of electrical double-layer capacitors. Tartu, 2013, 147 p.
127. **Kaija Põhako-Esko.** Novel organic and inorganic ionogels: preparation and characterization. Tartu, 2013, 124 p.
128. **Ivar Kruusenberg.** Electroreduction of oxygen on carbon nanomaterial-based catalysts. Tartu, 2013, 191 p.
129. **Sander Piiskop.** Kinetic effects of ultrasound in aqueous acetonitrile solutions. Tartu, 2013, 95 p.
130. **Ilona Faustova**. Regulatory role of L-type pyruvate kinase N-terminal domain. Tartu, 2013, 109 p.
131. **Kadi Tamm.** Synthesis and characterization of the micro-mesoporous anode materials and testing of the medium temperature solid oxide fuel cell single cells. Tartu, 2013, 138 p.
132. **Iva Bozhidarova Stoyanova-Slavova.** Validation of QSAR/QSPR for regulatory purposes. Tartu, 2013, 109 p.
133. **Vitali Grozovski**. Adsorption of organic molecules at single crystal electrodes studied by *in situ* STM method. Tartu, 2014, 146 p.
134. **Santa Veikšina**. Development of assay systems for characterisation of ligand binding properties to melanocortin 4 receptors. Tartu, 2014, 151 p.
135. **Jüri Liiv.** PVDF (polyvinylidene difluoride) as material for active element of twisting-ball displays. Tartu, 2014, 111 p.
136. **Kersti Vaarmets.** Electrochemical and physical characterization of pristine and activated molybdenum carbide-derived carbon electrodes for the oxygen electroreduction reaction. Tartu, 2014, 131 p.
137. **Lauri Tõntson**. Regulation of G-protein subtypes by receptors, guanine nucleotides and Mn^{2+}. Tartu, 2014, 105 p.
138. **Aiko Adamson.** Properties of amine-boranes and phosphorus analogues in the gas phase. Tartu, 2014, 78 p.
139. **Elo Kibena**. Electrochemical grafting of glassy carbon, gold, highly oriented pyrolytic graphite and chemical vapour deposition-grown graphene electrodes by diazonium reduction method. Tartu, 2014, 184 p.
140. **Teemu Näykki.** Novel Tools for Water Quality Monitoring – From Field to Laboratory. Tartu, 2014, 202 p.
141. **Karl Kaupmees.** Acidity and basicity in non-aqueous media: importance of solvent properties and purity. Tartu, 2014, 128 p.

142. **Oleg Lebedev**. Hydrazine polyanions: different strategies in the synthesis of heterocycles. Tartu, 2015, 118 p.
143. **Geven Piir.** Environmental risk assessment of chemicals using QSAR methods. Tartu, 2015, 123 p.
144. **Olga Mazina.** Development and application of the biosensor assay for measurements of cyclic adenosine monophosphate in studies of G protein-coupled receptor signalinga. Tartu, 2015, 116 p.
145. **Sandip Ashokrao Kadam.** Anion receptors: synthesis and accurate binding measurements. Tartu, 2015, 116 p.
146. **Indrek Tallo.** Synthesis and characterization of new micro-mesoporous carbide derived carbon materials for high energy and power density electrical double layer capacitors. Tartu, 2015, 148 p.
147. **Heiki Erikson.** Electrochemical reduction of oxygen on nanostructured palladium and gold catalysts. Tartu, 2015, 204 p.
148. **Erik Anderson.** *In situ* Scanning Tunnelling Microscopy studies of the interfacial structure between Bi(111) electrode and a room temperature ionic liquid. Tartu, 2015, 118 p.
149. **Girinath G. Pillai.** Computational Modelling of Diverse Chemical, Biochemical and Biomedical Properties. Tartu, 2015, 140 p.
150. **Piret Pikma.** Interfacial structure and adsorption of organic compounds at Cd(0001) and Sb(111) electrodes from ionic liquid and aqueous electrolytes: an *in situ* STM study. Tartu, 2015, 126 p.
151. **Ganesh babu Manoharan.** Combining chemical and genetic approaches for photoluminescence assays of protein kinases. Tartu, 2016, 126 p.
152. **Carolin Siimenson**. Electrochemical characterization of halide ion adsorption from liquid mixtures at Bi(111) and pyrolytic graphite electrode surface. Tartu, 2016, 110 p.
153. **Asko Laaniste.** Comparison and optimisation of novel mass spectrometry ionisation sources. Tartu, 2016, 156 p.
154. **Hanno Evard.** Estimating limit of detection for mass spectrometric analysis methods. Tartu, 2016, 224 p.
155. **Kadri Ligi.** Characterization and application of protein kinase-responsive organic probes with triplet-singlet energy transfer. Tartu, 2016, 122 p.
156. **Margarita Kagan.** Biosensing penicillins' residues in milk flows. Tartu, 2016, 130 p.
157. **Marie Kriisa.** Development of protein kinase-responsive photoluminescent probes and cellular regulators of protein phosphorylation. Tartu, 2016, 106 p.
158. **Mihkel Vestli.** Ultrasonic spray pyrolysis deposited electrolyte layers for intermediate temperature solid oxide fuel cells. Tartu, 2016, 156 p.
159. **Silver Sepp**. Influence of porosity of the carbide-derived carbon on the properties of the composite electrocatalysts and characteristics of polymer electrolyte fuel cells. Tartu, 2016, 137 p.
160. **Kristjan Haav**. Quantitative relative equilibrium constant measurements in supramolecular chemistry. Tartu, 2017, 158 p.

161. **Anu Teearu**. Development of MALDI-FT-ICR-MS methodology for the analysis of resinous materials. Tartu, 2017, 205 p.
162. **Taavi Ivan**. Bifunctional inhibitors and photoluminescent probes for studies on protein complexes. Tartu, 2017, 140 p.
163. **Maarja-Liisa Oldekop**. Characterization of amino acid derivatization reagents for LC-MS analysis. Tartu, 2017, 147 p.
164. **Kristel Jukk**. Electrochemical reduction of oxygen on platinum- and palladium-based nanocatalysts. Tartu, 2017, 250 p.
165. **Siim Kukk**. Kinetic aspects of interaction between dopamine transporter and *N*-substituted nortropane derivatives. Tartu, 2017, 107 p.
166. **Birgit Viira**. Design and modelling in early drug development in targeting HIV-1 reverse transcriptase and Malaria. Tartu, 2017, 172 p.
167. **Rait Kivi**. Allostery in cAMP dependent protein kinase catalytic subunit. Tartu, 2017, 115 p.
168. **Agnes Heering**. Experimental realization and applications of the unified acidity scale. Tartu, 2017, 123 p.
169. **Delia Juronen**. Biosensing system for the rapid multiplex detection of mastitis-causing pathogens in milk. Tartu, 2018, 85 p.
170. **Hedi Rahnel.** ARC-inhibitors: from reliable biochemical assays to regulators of physiology of cells. Tartu, 2018, 176 p.
171. **Anton Ruzanov.** Computational investigation of the electrical double layer at metal–aqueous solution and metal–ionic liquid interfaces. Tartu, 2018, 129 p.
172. **Katrin Kestav.** Crystal Structure-Guided Development of Bisubstrate-Analogue Inhibitors of Mitotic Protein Kinase Haspin. Tartu, 2018, 166 p.
173. **Mihkel Ilisson.** Synthesis of novel heterocyclic hydrazine derivatives and their conjugates. Tartu, 2018, 101 p.
174. **Anni Allikalt.** Development of assay systems for studying ligand binding to dopamine receptors. Tartu, 2018, 160 p.
175. **Ove Oll.** Electrical double layer structure and energy storage characteristics of ionic liquid based capacitors. Tartu, 2018, 187 p.
176. **Rasmus Palm.** Carbon materials for energy storage applications. Tartu, 2018, 114 p.
177. **Jörgen Metsik.** Preparation and stability of poly(3,4-ethylenedioxythiophene) thin films for transparent electrode applications. Tartu, 2018, 111 p.
178. **Sofja Tšepelevitš.** Experimental studies and modeling of solute-solvent interactions. Tartu, 2018, 109 p.
179. **Märt Lõkov.** Basicity of some nitrogen, phosphorus and carbon bases in acetonitrile. Tartu, 2018, 104 p.
180. **Anton Mastitski**. Preparation of α-aza-amino acid precursors and related compounds by novel methods of reductive one-pot alkylation and direct alkylation. Tartu, 2018, 155 p.
181. **Jürgen Vahter**. Development of bisubstrate inhibitors for protein kinase CK2. Tartu, 2019, 186 p.

182. **Piia Liigand.** Expanding and improving methodology and applications of ionization efficiency measurements. Tartu, 2019, 189 p.
183. **Sigrid Selberg.** Synthesis and properties of lipophilic phosphazene-based indicator molecules. Tartu, 2019, 74 p.
184. **Jaanus Liigand.** Standard substance free quantification for LC/ESI/MS analysis based on the predicted ionization efficiencies. Tartu, 2019, 254 p.
185. **Marek Mooste.** Surface and electrochemical characterisation of aryl film and nanocomposite material modified carbon and metal-based electrodes. Tartu, 2019, 304 p.
186. **Mare Oja.** Experimental investigation and modelling of pH profiles for effective membrane permeability of drug substances. Tartu, 2019, 306 p.
187. **Sajid Hussain.** Electrochemical reduction of oxygen on supported Pt catalysts. Tartu, 2019, 220 p.
188. **Ronald Väli.** Glucose-derived hard carbon electrode materials for sodium-ion batteries. Tartu, 2019, 180 p.
189. **Ester Tee.** Analysis and development of selective synthesis methods of hierarchical micro- and mesoporous carbons. Tartu, 2019, 210 p.
190. **Martin Maide.** Influence of the microstructure and chemical composition of the fuel electrode on the electrochemical performance of reversible solid oxide fuel cell. Tartu, 2020, 144 p.
191. **Edith Viirlaid.** Biosensing Pesticides in Water Samples. Tartu, 2020, 102 p.
192. **Maike Käärik.** Nanoporous carbon: the controlled nanostructure, and structure-property relationships. Tartu, 2020, 162 p.
193. **Artur Gornischeff.** Study of ionization efficiencies for derivatized compounds in LC/ESI/MS and their application for targeted analysis. Tartu, 2020, 124 p.
194. **Reet Link.** Ligand binding, allosteric modulation and constitutive activity of melanocortin-4 receptors. Tartu, 2020, 108 p.
195. **Pilleriin Peets.** Development of instrumental methods for the analysis of textile fibres and dyes. Tartu, 2020, 150 p.
196. **Larisa Ivanova.** Design of active compounds against neurodegenerative diseases. Tartu, 2020, 152 p.
197. **Meelis Härmas.** Impact of activated carbon microstructure and porosity on electrochemical performance of electrical double-layer capacitors. Tartu, 2020, 122 p.
198. **Ruta Hecht.** Novel Eluent Additives for LC-MS Based Bioanalytical Methods. Tartu, 2020, 202 p.
199. **Max Hecht.** Advances in the Development of a Point-of-Care Mass Spectrometer Test. Tartu, 2020, 168 p.
200. **Ida Rahu.** Bromine formation in inorganic bromide/nitrate mixtures and its application for oxidative aromatic bromination. Tartu, 2020, 116 p.
201. **Sander Ratso**. Electrocatalysis of oxygen reduction on non-precious metal catalysts. Tartu, 2020, 371 p.
202. **Astrid Darnell.** Computational design of anion receptors and evaluation of host-guest binding. Tartu, 2021, 150 p.

203. **Ove Korjus.** The development of ceramic fuel electrode for solid oxide cells. Tartu, 2021, 150 p.
204. **Merit Oss.** Ionization efficiency in electrospray ionization source and its relations to compounds' physico-chemical properties. Tartu, 2021, 124 p.
205. **Madis Lüsi**. Electroreduction of oxygen on nanostructured palladium catalysts. Tartu, 2021, 180 p.
206. **Eliise Tammekivi.** Derivatization and quantitative gas-chromatographic analysis of oils. Tartu, 2021, 122 p.
207. **Simona Selberg.** Development of Small-Molecule Regulators of Epi-transcriptomic Processes. Tartu, 2021, 122 p.
208. **Olivier Etebe Nonga.** Inhibitors and photoluminescent probes for in vitro studies on protein kinases PKA and PIM. Tartu, 2021, 189 p.
209. **Riinu Härmas.** The structure and H2 diffusion in porous carbide-derived carbon particles. Tartu, 2022, 123 p.
210. **Maarja Paalo.** Synthesis and characterization of novel carbon electrodes for high power density electrochemical capacitors. Tartu, 2022, 144 p.
211. **Jinfeng Zhao.** Electrochemical characteristics of Bi(hkl) and micro-meso-porous carbon electrodes in ionic liquid based electrolytes. Tartu, 2022, 134 p.
212. **Alar Heinsaar.** Investigation of oxygen electrode materials for high-temperature solid oxide cells in natural conditions. Tartu, 2022, 120 p.
213. **Jaana Lilloja.** Transition metal and nitrogen doped nanocarbon cathode catalysts for anion exchange membrane fuel cells. Tartu, 2022, 202 p.
214. **Maris-Johanna Tahk.** Novel fluorescence-based methods for illuminating transmembrane signal transduction by G-protein coupled receptors. Tartu, 2022, 200 p.
215. **Eerik Jõgi.** Development and Applications of E. coli Immunosensor. Tartu, 2022, 103 p.
216. **Alo Rüütel.** Design principles of synthetic molecular receptors for anion-selective electrodes. Tartu, 2022, 109 p.
217. **Tanel Sõrmus.** Development of stimuli-responsive and covalent bisubstrate inhibitors of protein kinases. Tartu, 2022, 148 p.
218. **Oleg Artemchuk.** Autotrophic nitrogen removal processes for nutrient removal from sidestream and mainstream wastewater. Tartu, 2022, 115 p.
219. **Andre Leesment.** Quantitative studies of Brønsted acidity in biphasic systems and gas-phase. Tartu, 2023, 83 p.
220. **Meeli Arujõe-Sado.** Structural effects in aza-peptide bond formation reaction. Tartu, 2023, 83 p.
221. **Jonas Mart Linge.** Electrochemical reduction of oxygen on silver-based catalysts. Tartu, 2023, 269 p.
222. **Tõnis Laasfeld.** Integrating Image Analysis and Quantitative Modeling for a Holistic View of GPCR Ligand Binding Dynamics. Tartu, 2023, 226 p.
223. **Ernesto de Jesus Zapata Flores.** Derivatization Reagents used in negative mode electrospray LC-MS. Tartu, 2023, 107 p.

224. **Patrick Teppor.** Obtaining platinum-free oxygen reduction catalysts through biomass valorization: a case study of peat. Tartu, 2023, 161 p.
225. **Peeter Valk.** Methanol Oxidation on Platinum-Rare-Earth Metal Oxide Activated Catalysts. Tartu, 2023, 162 p.
226. **Shidong Chen.** Unravelling prehistoric plant exploitation in eastern Baltic: organic residue analysis of plant-based materials by multi-method approach. Tartu, 2023, 245 p.
227. **Yogesh Kumar.** M-N_4 macrocycle-based catalysts for electrocatalysis of oxygen reduction and oxygen evolution. Tartu, 2023, 224 p.
228. **Kerli Martin.** Recognition of carboxylates by synthetic receptors – from structure-affinity studies to solid-contact anion-selective electrode prototyping. Tartu, 2024, 130 p.
229. **Huy Quí Vinh Nguyen.** Development of Carbon Supported Pt–CeO_2 Catalysts for Proton Exchange Membrane Fuel Cells. Tartu, 2024, 198 p.
230. **Heigo Ers**. Adsorption and Structuring Processes at Single Crystal Electrode – Ionic Liquid Interface – Insights from Simulations and *in situ* Studies. Tartu, 2024, 137 p.
231. **Ritums Cepitis.** Modelling Structural and Geometrical Effects in Carbon Dioxide and Oxygen Electrocatalysis. Tartu, 2024, 99 p.
232. **Kaarel Kisand.** Resorcinol-derived carbon-based catalysts for polymer electrolyte fuel cell cathodes. Tartu, 2024, 205 p.